



POLITECNICO
MILANO 1863

SCUOLA DI INGEGNERIA INDUSTRIALE
E DELL'INFORMAZIONE

Radiation Effects on Candidate Self-Healing Polymers for Space Applications

MASTER THESIS IN
MATERIALS ENGINEERING AND NANOTECHNOLOGY

Author: **Gianpaolo Bevilacqua**

Student ID: 996330
Advisor: Prof. Antonio Mattia Grande
Co-advisor: Ing. Laura Pernigoni
Academic Year: 2022-23

Abstract

In the upcoming years, space exploration will require missions of increasing duration, reaching destinations previously unthinkable for humans. The colonization of the Moon and the exploration of Mars are just two of the next challenges, the latter requiring a space travel that can last more than nine months. Limiting their durability and feasibility is the rapid deterioration of structures due to the extreme conditions of the space environment, which includes the presence of micrometeorites and orbital debris, atomic oxygen, vacuum, radiation and extreme temperature changes. Facing this, a strong interest has developed in recent decades in the application of self-healing materials. They would be able to extend the lifetime of components and to improve safety for astronauts, as well as significantly reduce the maintenance required during travel. The purpose of this thesis is to evaluate the effect of γ -radiation, present in the space environment, on the self-healing performance of two types of polymers: a supramolecular polymer, Arkema's Reverlink® HR, and four different poly(urea-urethanes). Space irradiation was simulated in the ESA-ESTEC laboratory in the Netherlands on two sets of samples, for a radiation dose of 100 and 500 krad. The irradiated samples were subsequently characterized by means of ATR-FTIR spectroscopy, DSC and TGA analysis, and the results compared with those obtained for blank samples in order to assess possible chemical-physical variations. To simulate the damage caused by micrometeorites, polymers were subjected to puncture tests and the self-healing performance was analyzed by measuring the flow rate changes following the hole created. By comparing the results obtained for irradiated and blank samples, the effect of radiation on their self-healing response was assessed. Furthermore, with the aid of a viscoelastic model based on the Zener model and on test results, an interpretation of the effects of radiation from the molecular point of view was proposed for the two types of polymers studied. Considerations concerning their suitability for space applications as inflatable and deployable structures are finally developed on the basis of the results obtained.

Key-words: self-healing polymers, inflatable structures, space radiation effects, micrometeorites and orbital debris, puncture tests.

Abstract in lingua italiana

Negli anni a venire l'esplorazione spaziale richiederà missioni sempre più durature nel tempo, raggiungendo mete in passato impensabili per l'essere umano. La colonizzazione della Luna e l'esplorazione di Marte sono solo due dei prossimi obiettivi, quest'ultimo che richiede un viaggio spaziale che può durare più di nove mesi. A limitarne la durata e la fattibilità, è il rapido deterioramento delle strutture a causa delle condizioni estreme dell'ambiente spaziale, che comprende la presenza di micrometeoriti e detriti orbitali, ossigeno atomico, vuoto, radiazioni e sbalzi termici estremi. A fronte di ciò, si è sviluppato negli ultimi decenni un forte interesse per l'applicazione di materiali autoriparanti. Essi sarebbero capaci di prolungare la vita dei componenti e migliorare la sicurezza per gli astronauti, oltre al ridurre notevolmente la manutenzione necessaria durante il viaggio. Lo scopo di questa tesi è quello di valutare l'effetto delle radiazioni γ presenti nell'ambiente spaziale sulla performance di autoriparazione per due tipi di polimeri: un polimero supramolecolare, il Reverlink® HR prodotto da Arkema, e quattro diversi poli(urea-uretani). L'irradiazione spaziale è stata simulata nel laboratorio dell'ESA-ESTEC in Olanda su due set di campioni, per una dose di radiazione pari a 100 e 500 krad. I campioni irradiati sono stati successivamente caratterizzati tramite spettroscopia ATR-FTIR, analisi DSC e TGA, e i risultati comparati con quelli ottenuti per i campioni bianchi, in modo da valutare possibili variazioni chimico-fisiche. Per simulare i danni causati da micrometeoriti i polimeri sono stati sottoposti a test di foratura e la performance di autoriparazione è stata analizzata misurando la variazione della portata a seguito del buco creato. Tramite la comparazione dei risultati ottenuti per i campioni irradiati e bianchi, è stato valutato l'effetto della radiazione sulla loro risposta autoriparativa. Inoltre, tramite l'ausilio di un modello viscoelastico basato sul modello di Zener e sui risultati dei test svolti, è stata proposta un'interpretazione degli effetti della radiazione dal punto di vista molecolare per i due tipi di polimeri studiati. Considerazioni in merito alla loro idoneità per applicazioni in campo spaziale come strutture gonfiabili e dispiegabili sono infine sviluppate a fronte dei risultati ottenuti.

Parole chiave: polimeri autoriparanti, strutture gonfiabili, effetti delle radiazioni spaziali, micrometeoriti e detriti orbitali, test di foratura.

Contents

Abstract	i
Abstract in lingua italiana	iii
Contents	v
1. Introduction	9
1.1 Introduction on the use of self-healing materials in space applications	9
1.2 The space environment.....	10
1.2.1 Radiations.....	10
1.2.2 ATOX.....	14
1.2.3 Debris	15
1.2.4 Outgassing.....	17
1.2.5 Thermal fluctuations.....	18
1.3 Self-healing mechanisms	19
1.3.1 Extrinsic mechanisms	21
1.3.2 Intrinsic mechanisms	23
1.4 Traditional elastomers adopted in space applications.....	26
1.5 Self-healing polymers for space applications	28
1.6 Inflatable and deployable space structures.....	29
1.6.1 TransHab and BEAM.....	30
1.6.2 EMU spacesuit	32
1.7 Research objectives	33
2. Materials and Methods	34
2.1 Materials tested	34
2.1.1 Poly(urea-urethane)s.....	34
2.1.2 Reverlink® HR.....	36
2.1.3 Samples manufacturing.....	37

2.2	Methods of tests	38
2.2.1	DSC Analysis	38
2.2.2	TGA Analysis	39
2.2.3	ATR-FTIR characterization	40
2.2.4	Irradiation Test	41
2.2.5	Puncture Test	42
3.	Results	48
3.1	DSC	48
3.1.1	Blanks	48
3.1.2	Comparison between blank and irradiated samples	49
3.2	TGA.....	52
3.2.1	Blanks	52
3.2.2	Comparison between blank and irradiated samples	54
3.3	ATR-FTIR.....	55
3.3.1	Blanks	55
3.3.2	Comparison between blank and irradiated samples	56
3.4	Puncture test.....	58
3.4.1	Blanks	59
3.4.2	Blanks aged	61
3.4.3	Irradiated samples.....	63
3.4.4	Comparison between blank and irradiated samples	73
4.	Modeling.....	77
4.1	Puncture test model.....	77
4.2	Viscoelastic model	82
4.3	Fitting	83
4.4	Results	89
5.	Final considerations and conclusions	94
5.1	Radiation effects on polymer's properties	95
5.2	Ageing effect on polymer's properties	98
5.3	Conclusions	100
5.4	Future developments	102

Bibliography.....	103
List of Figures.....	110
List of Tables.....	114
List of Symbols.....	116

1. Introduction

1.1 Introduction on the use of self-healing materials in space applications

The emerging challenges within space exploration are compelling scientists to take more into consideration the research and development of self-healing materials for practical applications, considering that all materials undergo degradation over time and are susceptible to wear, particularly when exposed to extreme environments and severe impacts.

The distinctive attributes of these materials have generated substantial interest. Their inherent self-healing properties offer the potential to extend the lifetime of components, reduce replacement expenses and improve safety, critical factors extremely important in space sector. Astronauts need to spend a lot of time and effort to identify the source of the damage and to find a suitable way to repair it. Any damaging event could seriously compromise its functionality and decrease its usefulness or, in the worst case, endanger the astronauts' lives. When looking at a new mission scenario in general, reliability, functionality and safety are essential and must be ensured by trying to minimize maintenance. Within this context, self-repairing materials have garnered attention thanks to their potential to enhance the dependability and safety of spacecrafts, while simultaneously lowering maintenance expenses. By integrating a self-healing mechanism into a design, the material could, following damage, partially or fully restore its primary functionality with minimal to none external intervention, thereby promptly repairing ruptures.

However, colonization and exploration missions involve the prolonged presence of astronauts and equipment in space over extended durations. This further intensifies the challenges associated with continuous exposure to space hazards and subsequent material deterioration and necessitates the imposition of more stringent demands on used technologies. Future spacecrafts must possess enduring longevity, exceptional reliability and self-sufficiency, while also being flexible enough to adapt to diverse conditions and necessitating minimal maintenance.

Exploiting such materials could enable the creation of structures and suits capable of autonomously repairing damage, therefore allowing astronauts to face longer missions, fostering greater safety, and reducing reliance on human intervention.

1.2 The space environment

One of the greatest challenges when being in space is the rapid deterioration of materials over time. In particular, in low Earth orbits (LEOs), at an altitude between 300 km and 1000 km, where the majority of space travel has taken place, numerous agents capable of causing damage and potential material failure are present. These include micrometeoroids and orbital debris (MMOD), ultraviolet radiation (UV), vacuum, absence of atmosphere, radiation exposure, extreme thermal solicitations and atomic oxygen (ATOX) effects.

1.2.1 Radiations

Radiation stands for the emission or transmission of energy through space or through a material medium, in the form of electromagnetic waves, rays and/or particles. It is categorized in ionizing or non-ionizing. Ionizing radiations include alpha, beta, x and gamma rays and photons and particles, carrying enough energy to ionize atoms and molecules, breaking chemical bonds [64].

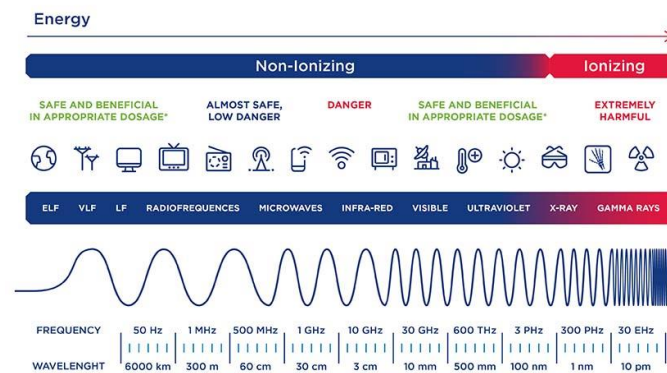


Figure 1.1: Electromagnetic spectrum damages [63].

Beyond Earth's magnetic shield, the space radiation environment presents one of the foremost challenges for prolonged human space missions. This radiation originates from star-trapping radiation belts, solar cosmic rays, and galactic cosmic rays [7]. These are composed of a variety of particles, including electrons, protons, heavy ions, photons, and more. Outside of the protection of the Earth's atmosphere and magnetic fields, fast electron-free nuclei are very common, capable of causing subsystem

degradation, such as solar cells and electronics, and, in long term missions, of inflicting irreversible damage to human health and DNA. According to this, there is the necessity to increase the residence time of astronauts and spacecrafts outside the Earth, reducing the damages associated to radiation exposure [31]. Table 1.1 shows the average radiation dose received according to the duration of the Apollo Missions [65].

Table 1.1: Residence time on the Moon during Apollo Missions [65].

Mission	Total Duration	Lunar Surface Duration	Average Radiation Dose*
Apollo 11	08 days, 03 hrs, 13 mins	21 hrs, 38 mins	0.18 rad
Apollo 12	10 days, 4 hrs, 31 mins	31 hrs, 31 mins	0.58 rad
Apollo 14	09 days, 01 min	33 hrs 31 mins	1.14 rad
Apollo 15	10 days, 01 hr, 11 mins	66 hrs, 54 mins	0.30 rad
Apollo 16	11 days, 01 hr 51 mins	71 hrs, 2 mins	0.51 rad
Apollo 17	12 days, 13 hrs, 51 mins	74 hrs, 59 mins	0.55 rad

In a space radiation environment, high-energy charged particles and photons can lead to both transient and enduring harm to spacecraft components and materials. This encompasses a range of effects such as single-particle impacts, total ionization dose effects, displacement damage, surface charge and discharge effects, internal charging, and ultraviolet radiation impacts.

Polymeric materials exhibit a wide variety of effects when exposed to radiation. The formation of new chemical bonds, which often occurs post-irradiation, generally leads to irreversible outcomes. These effects typically manifest as alterations in visual appearance, changes in chemical and physical states, and shifts in mechanical, electrical, and thermal characteristics. However, the impact of radiation varies across different properties of a polymer. The degree of a polymer's vulnerability to radiation-induced changes hinges on its chemical structure, as the excitation caused by radiation tends to localize around specific chemical bonds rather than affecting the entire molecular structure.

Irradiated polymers typically undergo two distinct reactions: cross-linking and chain scission [9]. Cross-linking leads to the formation of chemical bonds between adjacent polymer molecules, ultimately raising the polymer's molecular weight until it is encompassed in an insoluble three-dimensional network. Conversely, chain scission involves the breaking of polymer molecules, which reduces their molecular weight and increases solubility. Both reactions hold the potential to significantly modify the physical attributes of a polymer.

Space radiation consist of a combination of electromagnetic radiation and charged particles that have been accelerated to significant velocities. These charged particles are ionizing radiation and can be found in Solar Particle Events (SPE), Galactic Cosmic Rays (GCRs) and Van Allen Belts [9]. GCRs charged particles represent a continuous

hazard to individuals within spacecraft, while SPEs can pose a threat to individuals protected solely by contemporary space suits.

1.2.1.1 *Van Allen Belts*

The Van Allen belts are regions of confined charged particles within Earth's magnetic field. While absent in the expanse of deep space beyond Earth's sphere of influence, these belts do present potential hazards to individuals orbiting or departing from our planet. Extending to altitudes up to 19,000 km, they include multiple layers of charged particles within the contours of Earth's magnetic field, Figure 1.2.

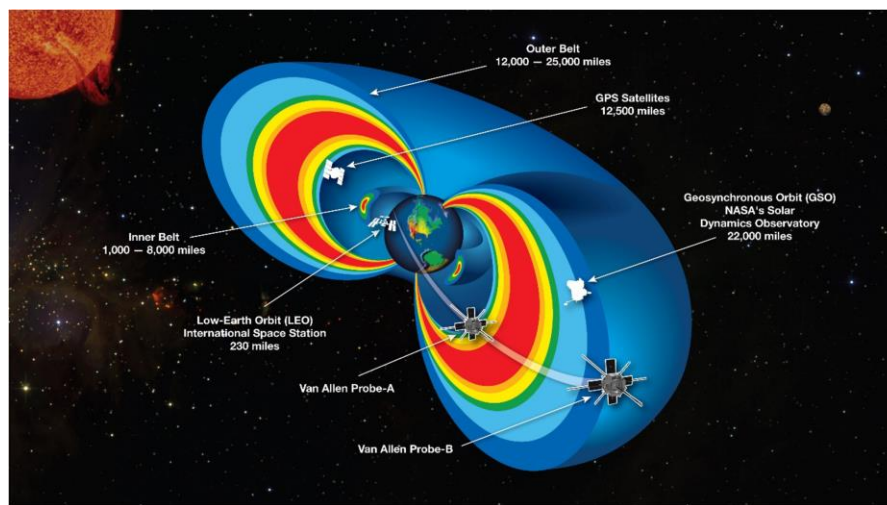


Figure 1.2: Van Allen Belts [66].

The inner Van Allen Belt, from 1000 to 10000 km, is composed by ionizing highly energetic protons generated by the collisions between GCRs and atoms from Earth's atmosphere. The outer Van Allen Belt, from 25000 to 32000 km, instead, contains low energetic particles, as ions and electrons.

1.2.1.2 *Galactic Cosmic Rays*

Galactic cosmic rays represent a highly hazardous form of radiation that necessitates effective shielding. These rays originate from outside the Solar System, predominantly within our own Milky Way Galaxy. GCRs can instigate considerable risks to crew health, notably by triggering the development of conditions such as cataracts, cancer, and degenerative diseases of various organ systems, particularly the central nervous system [21, 22]. These GCRs are characterized by their elevated energy levels and are primarily composed of three main constituents: approximately 85% hydrogen nuclei

(protons), 14% helium nuclei, and 1% high-energy and heavily charged ions known as HZE ions [24].

The nuclei referred to as HZE (High (H) Atomic Number (Z) and Energy (E)) elements possess distinctive attributes, despite their relatively low abundance. These nuclei exhibit remarkable characteristics such as high kinetic energy, significant ionizing potential, and exceptional penetrating ability. As they traverse through matter, they induce densely concentrated radiation-induced damage.

It's important to note that the content of these particles is influenced by the magnetic field of the Sun. Furthermore, their flux demonstrates an inverse correlation with solar activity throughout the 11-year solar cycle. Consequently, these particles display isotropic behavior in terms of radiation distribution. Their average intensity reaches its peak during the phase of minimum sunspots, characterized by the weakest state of the Sun's magnetic field, rendering it less capable of deflecting these particles [24].

The name derives from the fact that the bulk of GCRs seems to have a galactic origin. The directionality of these particles, upon reaching us, appears isotropic due to the galactic magnetic field, that confines particles for an average duration of around 107 years. GCRs span a wide range of energies, ranging from 10^8 to 10^{19} eV.

1.2.1.3 Solar Particle Events

Solar flares and coronal mass ejections have the ability to accelerate energetic solar particles in close proximity to the Sun, giving rise to what are known as Solar Particle Events (SPEs), Figure 1.3. During a SPE, there occurs a distinct release of ionizing particles, primarily comprising protons emitted by the Sun, alongside other nuclei including helium and HZE ions. This release of particles occurs over a limited period of time.

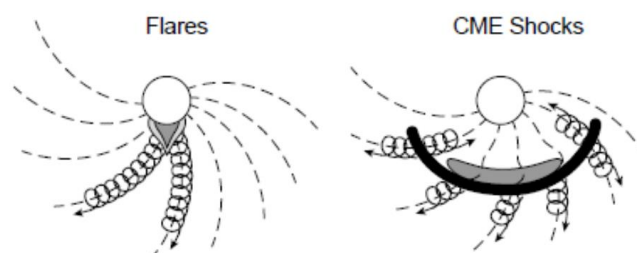


Figure 1.3: Solar Particle Events [31].

Contrary to GCRs, SPEs originate internally our Solar System itself. Moreover, they are characterized by higher particle fluxes but lower incident energies. Over extended periods of exposure, these ionizing particles possess the potential, if left unshielded,

to adversely impact astronaut health, potentially inducing severe acute effects [21, 22, 23].

1.2.2 ATOX

Atomic oxygen (ATOX) stands as the most prevalent gas species within the residual atmosphere, occupying the altitude range of 170 km to 700 km. The presence of atomic oxygen arises from the process of diatomic oxygen's photodissociation in presence of UV solar radiation (100 to 200 nm wavelengths), which is blocked by the atmosphere at lower altitudes (Figure 1.4) [10, 20]. In order to have the reaction, and so the scission of molecular interactions, the energy of the impact has to be higher or equal to the energy of the molecular bonds.

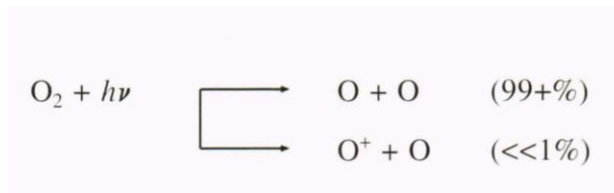


Figure 1.4: ATOX chemical reaction [20].

Ram-facing satellite surfaces, as they travel oriented through the medium, experience a constant bombardment of oxygen atoms, with a density ranging from $8 \cdot 10^{16}$ atoms $cm^{-2}s^{-1}$ at 100 km altitude to $8 \cdot 10^{11}$ atoms $cm^{-2}s^{-1}$ at 450 km altitude, the limit of very low Earth orbit (VLEO) space [10]. At the characteristic velocities of ram impacts (reaching speeds of 17,000 *mph*), the average energy associated with each impact measures at 4.5 electronVolts (*eV*).

ATOX can react both chemically and kinetically with the surface material. Over extended durations of exposure, these interactions can lead to notable deterioration of satellite surfaces. This phenomenon is commonly observed in the context of prolonged missions conducted within the confines of very low Earth orbit.

In early Space Shuttle flight experiments it was observed that hydrocarbon polymers subjected to the LEO environment would undergo gradual erosion due to their exposure to ATOX.

The interaction between ATOX and these polymers causes the surface to convert to volatile oxidation products, consequently contributing to the erosion of material over time, which rate vary among different types of polymers. The effects of atomic oxygen can extend beyond mere erosion; they can encompass severe structural, thermal, or optical deterioration of spacecraft components.

Given the noteworthy impact that this exposure can exert on a mission, there exist evident advantages in actively monitoring the flux of ATOX throughout the course of a flight. By quantifying the flux, a deeper comprehension of erosion rates and resultant effects can be achieved. The susceptibility to erosion is quantified through a parameter known as atomic oxygen erosion yield, which is the volume lost per incident atomic oxygen atom, given in $cm^3/atom$. Over time, numerous experiments conducted in the LEO environment have been instrumental in generating a dataset that encompasses atomic oxygen erosion yields for a wide range of materials [11].

In order to enhance our comprehension of phenomena like atomic oxygen erosion and the development of brittleness in spacecraft materials due to radiation, NASA Glenn has formulated a series of experiments. These experiments have been conducted as part of the Materials International Space Station Experiment (MISSE) missions, which involve placing test materials on the external surfaces of the International Space Station (ISS) [12].

Undercutting erosion due to ATOX can be a serious threat to spacecraft component survivability, as shown in Figure 1.5, where it has severely degraded the P6 Truss port solar array wing two-surface aluminized-Kapton® blanket box cover on the ISS.

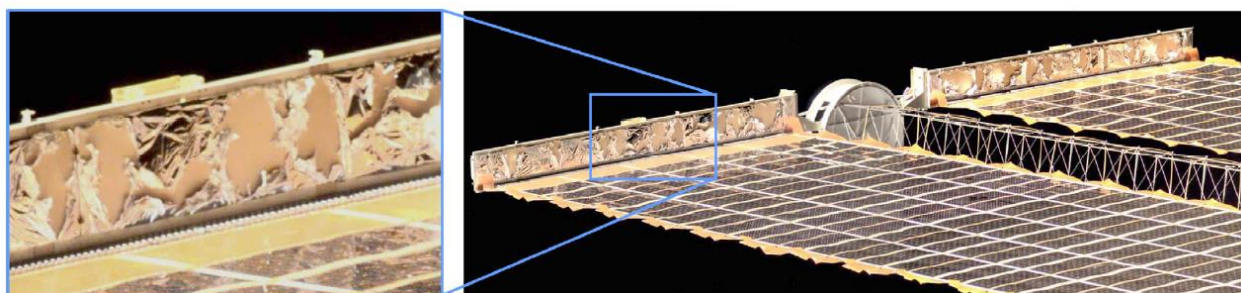


Figure 1.5: Atomic oxygen undercutting degradation of the solar array wing blanket box cover on ISS [12].

1.2.3 Debris

Micrometeoroids and orbital debris (MMOD) are related to shear, wear and perforation risks for spacecrafts and astronauts. Orbital debris include defunct human-made objects in space like nonfunctional spacecraft and abandoned launch vehicles, mission-related debris, fragmentation debris from the breakup of derelict rocket bodies and spacecraft [2].

These items travel, collide and explode creating additional debris with dimensions ranging from centimeters to meters. Considering a 1 centimeter in diameter debris with an average velocity of 10 km/s , it is capable of inflicting the same damage as a 550-pound object travelling 60 miles per hour on the earth [1]. These pieces of debris

may seem innocuous but at hypervelocity can become real killers. Several spacecrafts, both crewed and uncrewed, have been damaged or destroyed by them.

The continuous increase in the amount of debris over the years consequently enhances the risk of collisions. In Figure 1.6 is shown the variation of the amount of MMOD around the earth (on the left) and in LEO (on the right) [3]. These objects are tracked, together with most of their trajectories, by the U.S. Joint Space Operations Center (JSpOC).

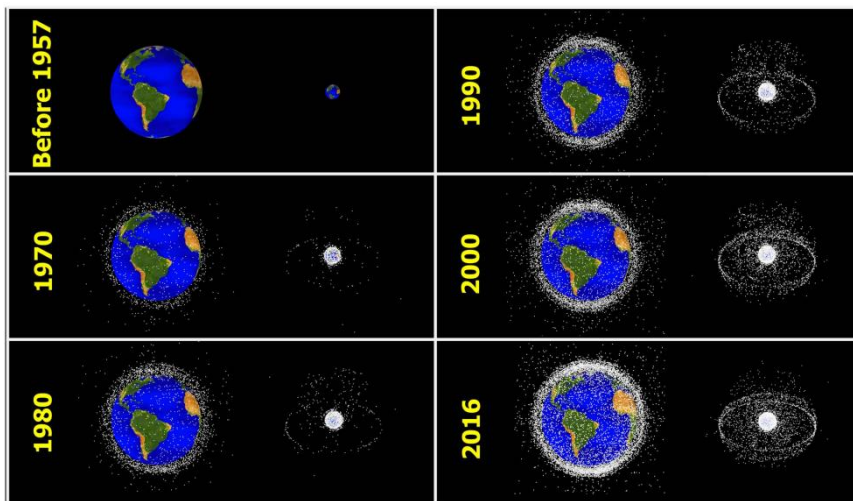


Figure 1.6: NASA simulation of MMOD near the earth and in LEO over the years [3].

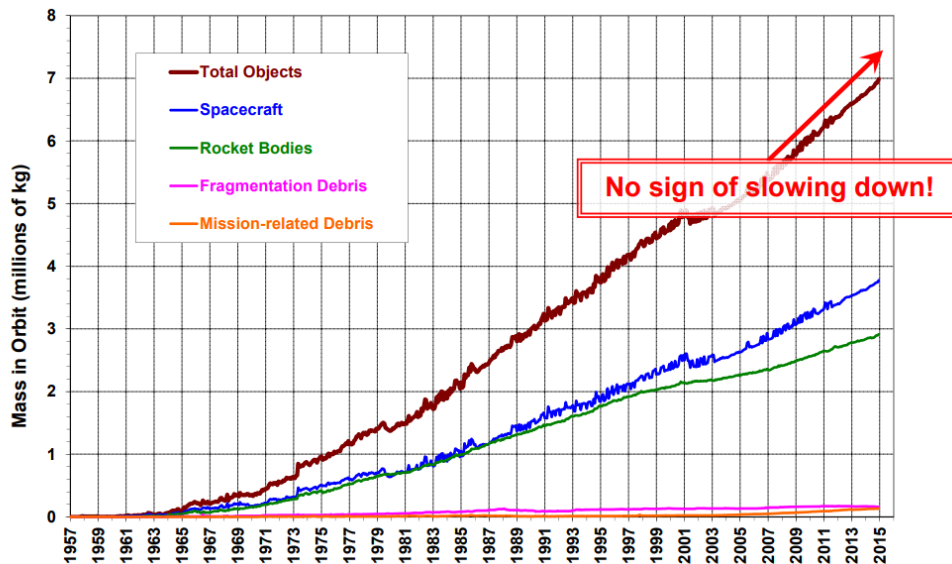


Figure 1.7: Material mass in Earth Orbit during the years [3].

All these elements have the potential to inflict irreparable damages to the spacesuit, triggering a potentially fatal depressurization scenario for the astronaut. Such a situation could result in the rapid boiling of bodily fluids or the swift depletion of

breathable air within a matter of seconds. Suit breaches can not only disrupt operations due to the loss of materials, but also lengthen the time needed to identify and repair the damage. In the case of substantial damage, even a puncture can lead to mission failure or the tragic loss of the astronaut's life.

1.2.4 Outgassing

Another common issue that requires attention involves the occurrence of outgassing phenomena within polymeric materials when exposed to ultra-high vacuum conditions and elevated temperatures. In such challenging environment, the material's surface experiences a release of gaseous substances, leading to a reduction in structural integrity and potential contamination of adjacent components. The presence of outgassing from polymeric materials in space settings can lead to a loss of mass, which not only impacts the material's effectiveness, but also introduces harmful effects on both the spacecraft and its surrounding atmosphere, formed by the outgassed products [4].

The outgassing phenomena arises due to the significant reduction in pressure and temperature fluctuations encountered in space environment compared to standard temperature and pressure conditions. Vacuum-induced outgassing is defined as the emission of gaseous elements from a surface exposed to conditions of deep vacuum [5].

In typical operational settings within space environments, the ultra-high vacuum levels (ranging from 10^{-7} to 10^{-9} Pa in Low Earth Orbit regions and below 10^{-4} Pa inside satellites) possess the capability to cause the sublimation of exposed surface atoms. This, in turn, results in adverse effects such as compromised structural integrity and contamination.

Furthermore, during the production of organic polymers, the polymerization process incorporates a large number of low molecular weight additives. These compounds within the material gradually migrate towards the material's surface and subsequently desorb from it. The process of material evaporation is linked to its saturated vapor pressure. Polymers used on spacecraft exhibit extremely low vapor pressure, consequently, under typical operating temperatures, the loss of mass due to evaporation remains minimal. Hence, the primary concern revolves around the mass loss attributed to outgassing [4, 5].

The implications of outgassing can be particularly significant for various space applications, including optical systems, HV devices, scientific exploration tasks etc. Noteworthy examples include instances where outgassing has detrimentally affected the functionality of critical components. For instance, the charge-coupled device

(CCD) detector located within the navigation sensor of NASA's Stardust probe encountered a degradation in image quality as a result of outgassing effects. Similarly, on the Cassini spacecraft, a narrow viewing angle camera experienced pronounced image flares due to outgassing, as illustrated in Figure 1.8. To mitigate this contamination, an extended heating degassing process was employed.

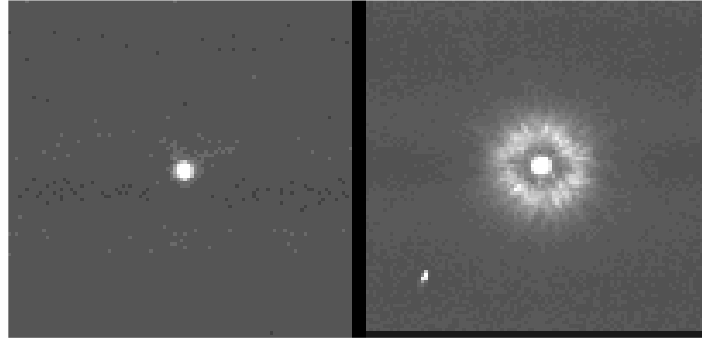


Figure 1.8: Glow in image of planet due to contamination of spacecraft Cassini. Left: no contamination. Right: contamination [6].

Hence, it becomes mandatory to assess the polymer outgassing in high thermal-vacuum conditions to guarantee the dependability of these materials in aerospace applications. Beyond the evident loss in mechanical properties witnessed as a consequence of outgassing, there exist a multitude of potential risks that necessitate careful consideration. These risks include scenarios such as the impairment of optical components and solar cells due to obscuration, the emergence of localized clouds impacting the accuracy of sensitive instruments, as well as the potential for pollution and corrosion affecting thermal control surfaces and passive radiative cooling systems. Consequently, a comprehensive approach to minimize these risks is of utmost importance.

1.2.5 Thermal fluctuations

Another fundamental issue is represented by thermal fluctuations. When considering the external structure of the spacecraft, it may receive radiant thermal energy from mainly three environmental sources: incoming solar radiation, reflected solar radiation (albedo) and outgoing longwave radiation (OLR) emitted by the Earth and atmosphere, Figure 1.9 [54, 56]. With the respect to the spacecraft, the space can be represented as the absolute black body acting as a sink, and the temperature field of the spacecraft is related to circulating and waste heat created by itself.

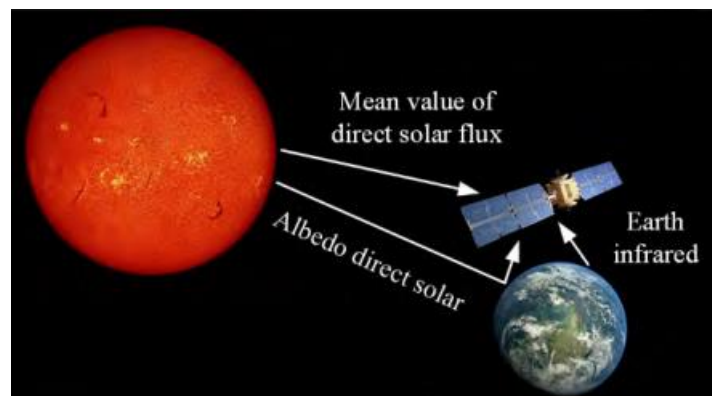


Figure 1.9: Radiant thermal energy sources of heat of the spacecraft [56].

Averaging over long time periods, the incoming solar energy and the outgoing radiant energy are in balance, leading to a radiative equilibrium between Earth, atmosphere and Sun. However, this balance is not present everywhere on the globe according to time, geography, and atmospheric conditions [54]. When orbiting and during interplanetary transfers, a spacecraft is subjected to temperature fluctuations and changes, due to external heat variations that are typically cyclic. Consequently, a spacecraft surface temperature can typically go from -100°C to 100°C and even from -150°C to 150°C in extreme situations like in geostationary orbit [55]. These temperature fluctuations can influence the material's internal and bonding strength, causing possible cracks, deformations, ageing and detachment from the spacecraft, as well as fatigue for wires and solder joints, promoting system failures [53, 54].

Solutions to this problem span from active systems, like fluid loops, to passive ones, as coatings and Multi-Layer Insulation (MLI), but the latter present some limitations like ATOX degradation in LEO missions [53].

1.3 Self-healing mechanisms

Self-healing materials are a class of smart materials able to locate and heal damages, like biological systems they can regenerate their functionalities, recovering, partially or totally, the mechanical and physical properties of the virgin component. This ability is known as the concept of "damage prevention" or "damage management" [30, 31]. For this reason, self-healing materials are characterized by longer service lifetimes (Figure 1.10) and higher reliability, fundamental property in space applications. According to this, the research aims to develop healing materials capable of self-repair in the lowest possible amount of time.

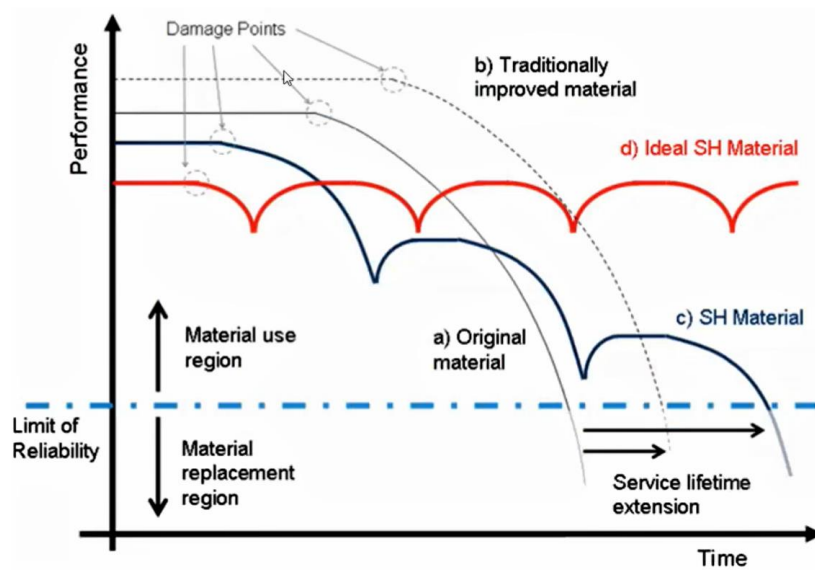


Figure 1.10: Damage management: traditional materials (grey) and self-healing materials (red and blue) [30].

This class of materials are not able to heal catastrophic damages, but only smaller fractures and deteriorations, like delamination, scratches and debris impacts, in order to prevent bigger ones arising from them. To achieve optimal healing, different strategies may be required for different damages, Figure 1.11 [30].

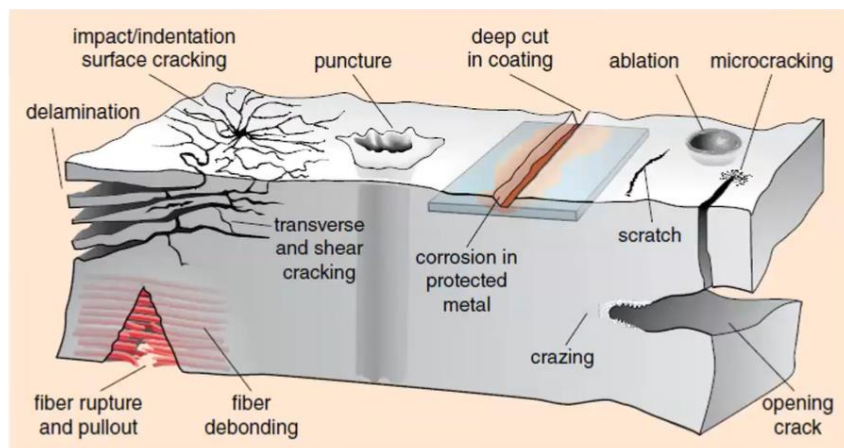


Figure 1.11: Damages that could be repaired by Self-healing materials [30].

The classification of self-healing polymers can be based on working chemistry, distinguishing them in autonomous and non-autonomous, or on mechanism, in intrinsic and extrinsic, Figure 1.12 [57].

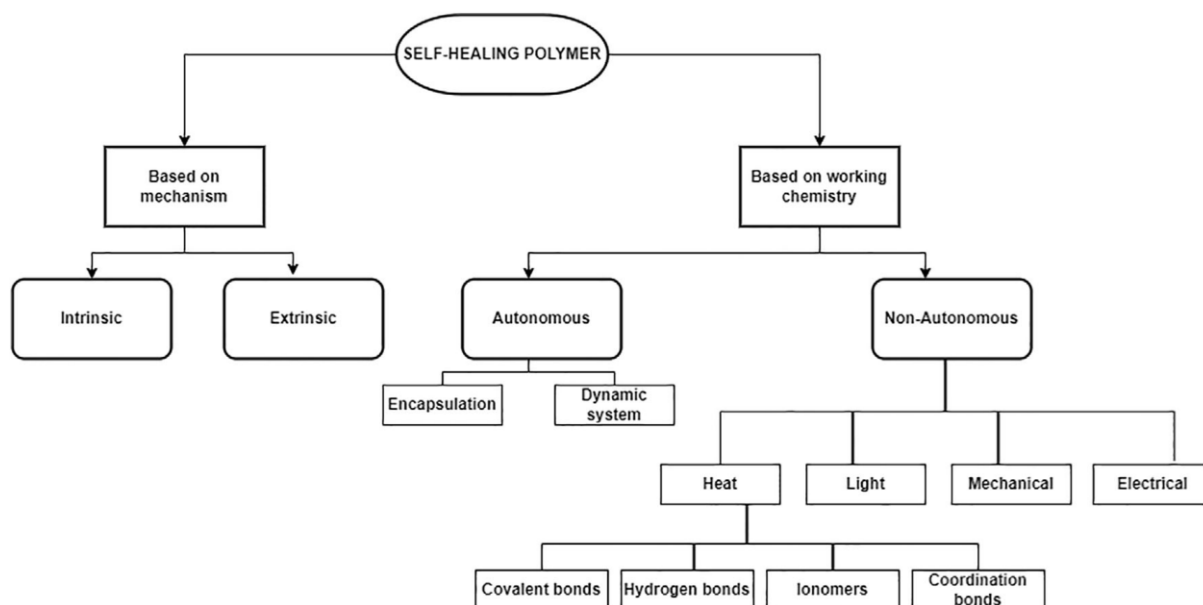


Figure 1.12: Classification of self-healing polymers [57].

In the first case, autonomic self-healing materials don't need external actions as the damage itself is the stimulus for the healing process, while non-autonomic ones, on the contrary, are activated by external phenomena capable of changing the state of the matter, such as heat or light exposure [19, 36]. The most fundamental distinction is instead represented by extrinsic and intrinsic self-healing materials. In extrinsic materials the matrix and the healing agent are two different entities, instead intrinsic materials are characterized by a matrix with reversible chemical and physical bonds, that represent the repairing capability [47, 48, 49].

1.3.1 Extrinsic mechanisms

The activation of the reactive substances of extrinsic self-healing materials can be due to environmental or chemical exothermic reactions, between a healing resin and a catalyst, both methods can be in the form of microcapsules or hollow fibers [37]. For the ones activated by environmental reaction only the healing resin is encapsulated in thin flexible films, while for the ones activated by chemical reactions both the resin and the catalyst are encapsulated. In the thin flexible film, there can be miscibility problems if not enough capsules are broken during the crack propagation [30].

1.3.1.1 Microcapsules

Microcapsules are polymeric inert spherical or irregular shells of different sizes, from nano to micro-scale, filled with cross-linkable liquid oligomer. The capsules are

inserted into a low viscosity epoxy matrix with dispersed catalyst and the shell is usually made of poly-urethane or a thermoplastic material, which must be more brittle than its content to break during crack propagation, letting the resin out (Figure 1.13) [30, 31].

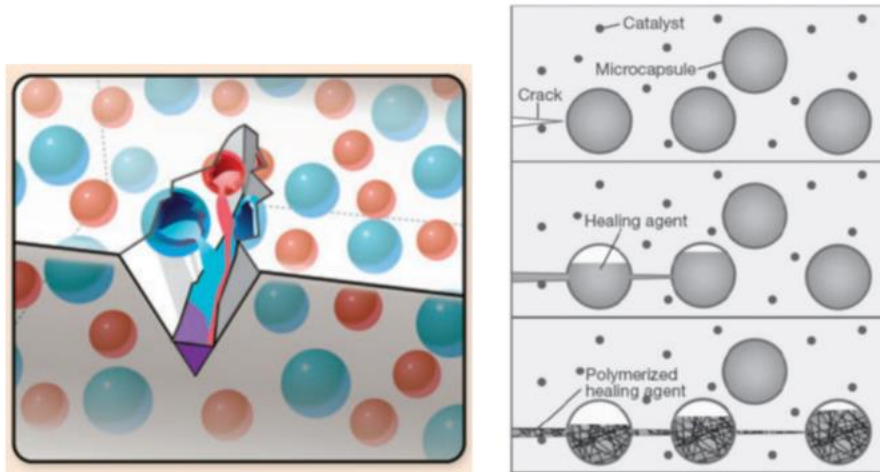


Figure 1.13: Microcapsules (left) [43] and healing process (right) [47].

The healing process occurs when the healing agent reaches the crack, leading to the cross-linking reaction promoted by the catalyst [47, 49]. In order to have a very efficient process, cracks should be attracted by the healing particles. To decrease the capsules strength, flaws can be added inside them, but not on their shell as the crack would propagate at the interface instead breaking it. Usually, smaller particles attract cracks regardless the Young's modulus [30]. The volume of the contained healing agent is limited, for this reason it is not possible to heal extended damages and, when capsules are already broken, it is not possible to repeat healing process as the liquid has already leaked out [19].

1.3.1.2 Hollow fibers

Hollow fibers are usually made of glass or carbon and placed in critical points. They are used as a biomimetic extrinsic healing methodology characterized by non-reversible chemical bonds, providing high strength on the axial direction and self-healing action [47]. The working principle is the same as for capsules, with a resin able to polymerize and fill the crack, starting the healing process when the resin and the catalyst get in contact [39]. The system can also be designed in order to transport two different types of healing agents, but the exothermal reaction, leading to unknown outgassing effects, is potentially dangerous for the lifetime of the component [19]. Also

in this case, the healing process can be done only once and is not able to heal large damages.

The main disadvantage of both hollow fibers and microcapsules is related to the fact that we are adding a brittle phase to the material. The mechanical properties can be compromised and, in particular, a crack in the interface between fibers and matrix can cause a catastrophic failure of the whole material [49].

1.3.1.3 *Micro-vascular network*

Another possible extrinsic self-healing system, apart from microcapsules and hollow fibers, is the micro-vascular network (Figure 1.14). Here, the healing agent is an inorganic ink transported to the crack through a 3D vascular hollow vessel network inside the matrix. The dimension of the channels must be big enough to let the flow of the ink, but not too much in order to not affect the mechanical properties of the matrix itself [43]. The advantages of this approach are that the rate of the healing process can be increased pressurizing the micro-vascular networks and the possibility of having multiple healing events during the lifetime through a continuous refill of the healing agent [36]. However, the manufacturing process is very expensive and complex.

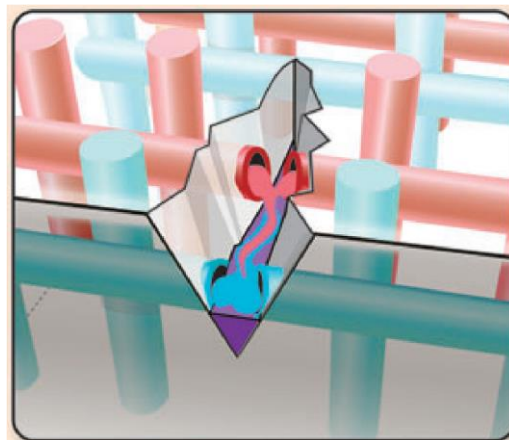


Figure 1.14: Microvascular network [43].

1.3.2 *Intrinsic mechanisms*

Intrinsic self-healing materials are characterized by a repairing mechanism based on the acquired mobility of the polymer chains of the matrix when subjected to an external stimulus, without the necessity of external elements like fibers and capsules, Figure 1.15 [43, 49]. The external input can be an electrical, electromagnetic, magnetic, photo or ballistic stimulus as well as heat or a mechanical input. The density of reversible chemical bonds and the level of chain mobility influence the repairing

process [31]. A great advantage with the respect to the extrinsic mechanism is that, since the healing process is due to the reversibility of intrinsic interactions and not due to the use of an healing agent, the same region of the polymer can be repaired multiple times and not just once [45, 46].

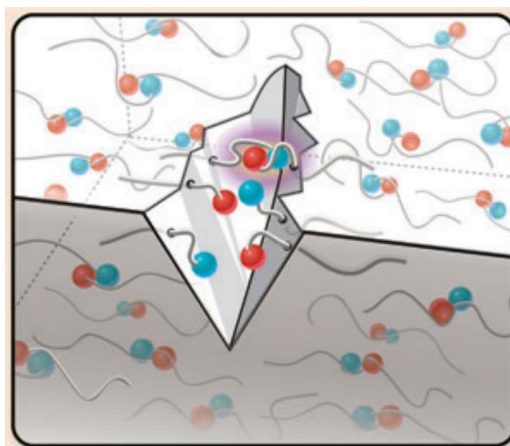


Figure 1.15: Intrinsic self-healing mechanism [43].

1.3.2.1 *Healing through covalent polymer chains*

An example of intrinsic self-repairing mechanisms that exploit reversible covalent bonds is the one exploiting the Diels–Alder/retro-Diels–Alder interactions (DA/rDA). This process is based on the synthesis of furan-maleimide polymers (DA reactions) that forms a cyclic or bicyclic compound that can be inverted through a heating process (rDA interactions), acquiring enough mobility to perform the healing process [31, 48].

1.3.2.2 *Supramolecular polymers*

Supramolecular polymers are assemblies of monomer units arranged in a polymer-like manner. These units are held together by reversible and specifically oriented secondary interactions. The non-covalent bonds, which confer self-healing functionality, include van der Waals forces, hydrogen bonding, pi-pi stacking, metal coordination, halogen bonding, chalcogen bonding, and host-guest interactions.

The chain lengths relate directly to the strength of the non-covalent bonds, the monomer concentration and the temperature [28]. When subjected to mechanical stress there is the formation of two interfaces due to the yielding of the weakest links in the chain. To re-establish the bond, it is essential to bring these interfaces closer to each other again [25]. Successful revival of supramolecular interactions in these systems necessitates adequate molecular mobility at viable temperatures, enabling the

re-engagement of these interactions. This process effectively bridges the impaired region, promoting the occurrence of healing [26].

Typically, repair takes place even at ambient room temperature when the functional groups are brought into effective contact. Increasing the healing temperature increases molecular dynamics, consequently accelerating the healing mechanism and reducing the required time. Another parameter that influences the evaluation of process efficiency is the interval between the occurrence of damage and the actual mending [30]. For instance, in healing systems based on hydrogen bonding, the efficiency decreases as time increases. This is due to the tendency of free hydrogen bonds to reorganize and link with adjacent bonds on the same fractured surface, rather than those located on the opposing side of the crack [27].

1.3.2.3 Ionomers

Ionomers are polymers that show an improvement in mechanical properties such as traction, impact, tear, and abrasion, due to the presence of ions (20% in composition). The self-healing nature is given by ionic reversible interactions in form of clusters, activated by external stimuli as UV radiation and temperature [45]. Moreover, this self-healing process is limited to the condition of an impact with high energy with the object, that passes through the material itself in a short time (ballistic impact of a projectile). In this way the kinetic energy of the object is transferred to the material in the form of heat and elastic energy, enabling the mobility of the ions in the polymeric chain and the closure of the crack [44, 49, 19].

One disadvantage is that ionomers are not suitable for low temperatures, since consequently the material assumes brittle response to impacts, nor for high temperatures, because it acquires a viscous behavior and does not have enough elastic recovery [30]. In the first case the healing process efficiency is almost zero, while in the second case the material is still able to heal in a single damage site repeatedly [25]. Surlyn® and Nucrel® are examples of commercial self-healing ionomers [36].

1.3.2.4 Viscoelastic materials

Viscoelastic materials, as can be seen from the name, are substances that show both the viscous and elastic behavior, being in this way able to both dissipate and store energy during the service. An example are elastomers, polymers that below the glass transition temperature are glassy and rigid, while above it, in unstressed state, are amorphous with a low Young modulus related to the twisted and coiled state of the molecular chains. The healing behavior is shown in the second case, since once we

apply a tensile load, the chains are partially straightened allowing for an high elongation, returning back to the initial shape when the stress is released [38, 41, 30].

1.3.2.5 *Reversible polymers*

The self-healing mechanism for reversible polymers depends on the presence of covalent or non-covalent bonds. In the first case covalent bonds can be reverted exploiting the mobility of the material at crack faces to entangle polymers chains, while in the second case the healing mechanism is based on intermolecular interactions, as ionic clustering and hydrogen bonding [36]. Isocyanate polymers (Polyurethanes) are an example of reversible polymers, characterized by organic monomers joined by urethane linkages and obtained from the reaction of a diisocyanate, containing two or more isocyanate groups $N = C = O$, with a polyol, having two or more hydroxylic groups OH, which can be the cause of a low glass transition temperature [40]. Radiation energy is the form of energy needed to be provided for the healing process, that activates when the reversible polymer is heated above its glass transition temperature, expanding itself and filling the crack. The process is long and requires external input, but it is repeatable, simple and preserve the original mechanical properties [42].

1.4 Traditional elastomers adopted in space applications

From the beginning of the space era, polymeric materials have been extensively used as construction materials due to their beneficial combination of mechanical, thermal, electrical, and thermo-optical properties, as well as their high strength-to-weight ratio. Typical used polymers are polysiloxanes (silicones), epoxies, polyurethanes, polyesters, acetals, acrylics, polyamides, fluorocarbons, polyimides, etc. [85].

The reason for this high employment is the ability of polymers to be easily modified by the addition of other materials as fillers, providing limitless different properties and possibilities. They, however, must meet the requirements to cope with the space environment, as well as safety, applied to both the instrument and the personnel. Polymeric materials that might contaminate optics, provide electrical shorts or corrode metal surfaces for example, cannot be used since they will worsen the overall performance of the equipment [83].

Some spacecraft applications where polymers are widely involved include adhesives, lubricants, temperature regulating blankets, thermal control paints, circuit boards, coatings and high stiffness composites [83].

- *Thermal blankets* are essential for regulating the spacecraft temperature. They are constituted by a multi-layer insulation of polymeric films that can be filled with carbon black pigment, in order to absorb light, or coated with a layer of vapor deposited aluminum to reflect sunlight. Polyimide, Fluorinated Ethylene Propylene (FEP) and glass fiber Beta cloth® are commonly employed materials for the first film, important to determine the equilibrium temperature of the surface. Beta cloth® consists of glass fabrics impregnated with Teflon. Films commercially available are made of Mylar® (polyethylene terephthalate) or Kapton® (polyimide), separated by fine scrim cloths made from Nylon® polymers [83].

- *Thermal control paints* have the same purpose as thermal blankets. They consist of pigments dispersed in an inorganic or organic binder, giving to the paints a black or white color. White paints are characterized by higher emissivity, rejecting the heat in excess back to space, and the most widely used binder is silicone. Black paints are, instead, filled with carbon black, providing solar absorbance (85%) and protection from UV light.

- *Adhesives* are very common in most spacecraft components, a very widely used class is the two-part epoxies, possibly modified by the addition of fillers. In this class of adhesive two liquid components are mixed and cured to a hard adherent solid.

- *Electronic components* experience the application of many polymers in different areas. Circuit board materials can be based on an epoxy impregnated glass or quartz cloth, with poly(cyanate) resins giving low dielectric constants, permitting higher frequencies to be achieved than conventional epoxy boards. Powdered silver fillers are used for conductive adhesives, where confined spaces or soldering temperatures are restrictive. Teflon is widely used for wire insulation exploiting its chemical inertness but has a low radiation stability. Insulations based on cross-linked polymers of vinylidene fluoride (PVDF) have been studied recently for insulation in high radiation environments [83].

- *Composites for structural applications* offer high strength to weight and stiffness to weight ratios, reducing spacecraft mass while improving mechanical performance. Polymers in this sense are able to replace aluminum, titanium and steel in spacecraft. A standard construction material for spacecrafts is based on high modulus graphite fibers dispersed in polymer matrix resins, mostly fabricated as laminates alternating in directions.

- *Lubricants* involves certain all polymer-based classes (poly-alpha olefins, poly-aryl ethers), offering high lubricity, high radiation resistance and low vapor pressure.

Moreover, there exist many other widely used specific polymers in space applications. Polyetherimide (PEI)/polycarbonate (PC) are used in making satellites and external

hardware, being high heat, solvent, and flame resistant with high dielectric strength, thermal conductivity and tensile strength. A great advantage is that those polymers can be 3D printed on board, allowing for tools, spares, repairs and structures to be created on site [86].

Developed in 1999 by Triton Systems, TOR (Triton Atomic Oxygen Resistant) polymers protect against erosion due to ATOX and radiation, giving 10 times longer survival periods with the respect to other polymers, allowing for cost savings from replacements and repairs. This resistance is provided by phosphorous, that reacts with oxygen producing a protective phosphate layer [87]. Sodium polyacrylate is a super absorbent polymer, it is capable of locking in 400 times its weight in water. It is used in NASA's Maximum Absorbency Garment (MAG) to absorb the astronauts' biological waste during extra-vehicular activities [86, 84].

1.5 Self-healing polymers for space applications

Spacecraft materials are subjected to harsh space environmental variables (1.2), in particular outside the LEO. A small collision, for example, with tiny MMOD can produce punctures or damages leading to gas leakage and depressurization, with possible harmful consequences for the spacecraft and the astronauts inside. Considering long-term missions, there is the necessity of materials able to sustain these circumstances. Mechanical properties related to the self-healing efficiency includes fracture toughness, impact strength and fatigue property [57].

Fracture toughness: in self-healing materials, the recovery rate of fracture toughness can go from 30% to 100%, and should be around 75% of the fracture load when using microcapsules containing epoxy resin, but the amount of healing agent and catalyst used has an important effect on it [58].

Fatigue property: Fatigue is the decrease of strength or failure due to cyclic stress, that can be above or below the yield strength. Composite structural materials and metallic materials are much more susceptible to fatigue with the respect to polymers. In general, self-healing materials have not only the ability to heal cracks, but also the ability to increase the fatigue life of the components, in particular using vascular epoxy composites [59].

Impact property: it is related to the ability of the material to absorb energy during plastic deformation. Under low velocity impacts, E-glass epoxy composites show good healing behavior [60], while under high-velocity impacts ionomeric polymer, as replacement to aluminum panels, is a good alternative [61].

Xiang and group [62] used the co-electrospinning method to create a hybrid carbon/fiber epoxy composite with a self-healing core shell nanofibers at interfaces, in particular dicyclopentadiene/polyacrylonitrile (DCPD/PAN) by using dicyclopentadiene (DCPD) as a healing agent, encapsulated into polyacrylonitrile (PAN). The polymer matrix composite is low cost, easy to manufacture and lightweight, offering to aerospace applications high-strength and high-toughness.

An intrinsic self-healing supramolecular polymer applicable for space applications is Reverlink® HR, produced by Arkema. The characterization of such polymer has been introduced by my advisor Prof. Antonio Grande and Laura Pernigoni [36, 50], and will continue in this thesis work.

Carbon fiber reinforced plastic is a self-healing polymer with the purpose of preventing delamination fracture, used in aeronautics. Microcapsules are applied and the healing agent is Cyclopenta-1,3-diene mixed up with polyepoxides by 20 wt.% [57]. Research was also done on autonomic self-healing, where either carbon fiber reinforced polymer (CFRP) and glass fiber reinforced polymer (GFRP) were implanted and infused with uncured resin. When damaged, some fibers packaged with resin break away, releasing the stored healing agent toward the damaged site recovering it [57].

Those are only some examples of polymeric materials that show promising self-healing properties for space applications, but none of them has been already qualified for space. One of the big uncertainties is related to how long they are able to keep the self-healing ability, and how this ability is affected by the exposition to the complex and combined action of the hazardous space environment [53].

1.6 Inflatable and deployable space structures

Inflatable and deployable space structures are adaptive systems that use pressurized air or gas to expand from its packaged to its operational configuration. The pressurized air or gas has also the aim of maintaining the shape and a robustness comparable to rigid metallic counterparts. They include space suits, habitats, ballutes and airlocks and will gain more and more importance in future space explorations for their increased potential, since they offer significant benefits over conventional structures. Inflatable structures are flexible and characterized by high volume-to-mass ratio and high packaging efficiency, that results in the possibility to be packaged in smaller volumes with the respect to their deployed one, selecting in this way smaller launch vehicles which greatly reduces the costs (Figure 1.16).

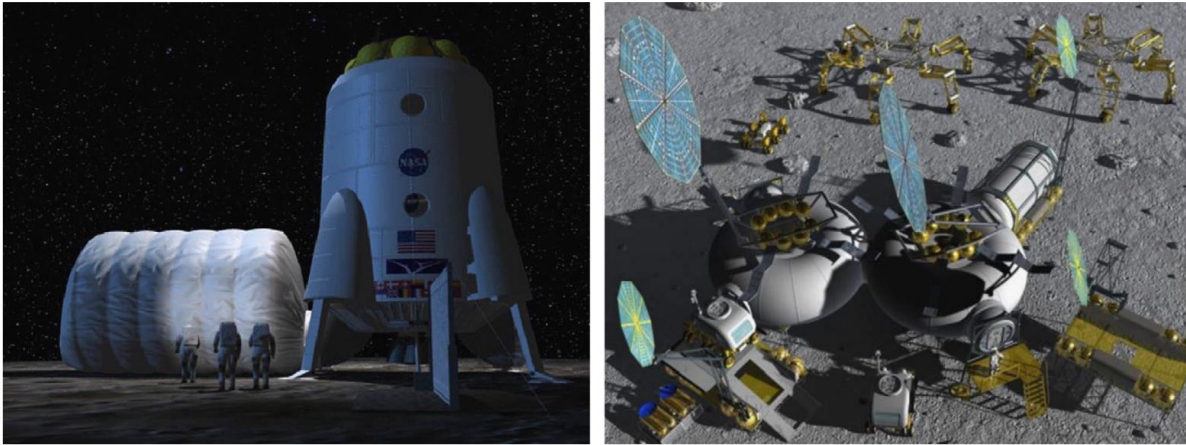


Figure 1.16: Cylindrical and toroidal inflatable habitats on the lunar surface [69].

Additionally, with these structures there is a minimal need for on-site construction materials, since all the assembly mechanism is inherent to the structure, and fewer secondary radiation effects, due to the use of soft goods with the respect to metallic structural materials [69].

Nevertheless, the structure must protect the crew from the harsh space environment and so must maintain its integrity against radiation, MMOD, ATOX, extreme thermal solicitations, absence of atmosphere and vacuum. Leakage and depressurization can be caused by MMOD impacts and contacts with sharp objects, leading to punctures and cuts [36]. These events can have catastrophic consequences and can cause the failure of the space mission. Self-healing materials would increase safety and reliability, with a reduction of maintenance costs and longer operational life.

1.6.1 TransHab and BEAM

One of the first projects for the development of inflatable space structures was the TransHab, conducted in the 1990s by NASA. Originally, the TransHab was designed to support a crew of six astronauts as a transit habitat to and from Mars, but then it was proposed as a habitation module of the ISS [70]. It combines a hard central core with an inflatable shell.

The ISS TransHab is divided into four functional levels. The first three levels are dedicated to living space and the fourth one is the connecting tunnel (Figure 1.17).

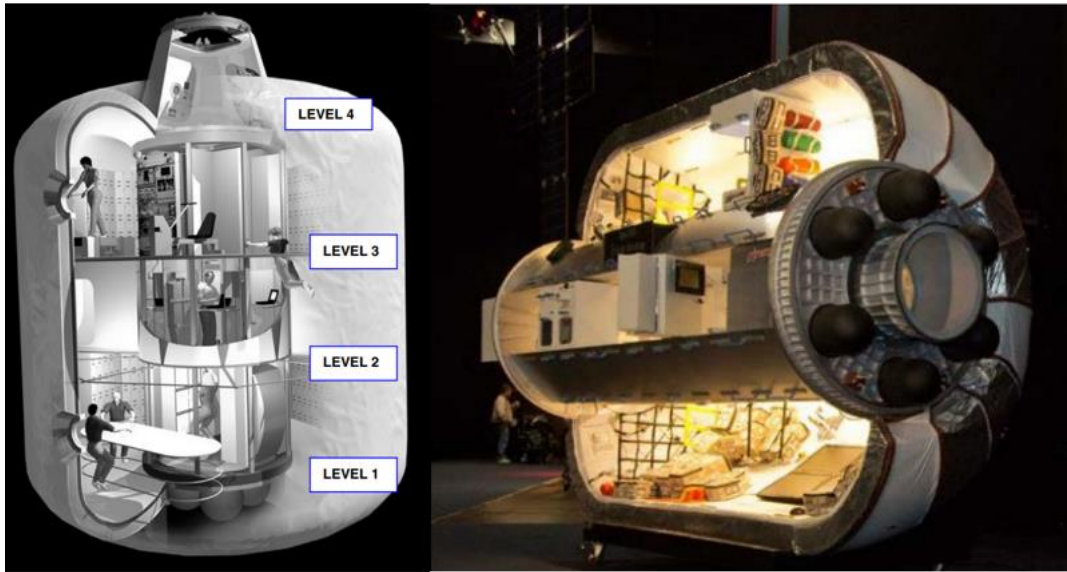


Figure 1.17: TransHab internal view and cutaway model [70].

Although the TransHab project never actually launched, it started the work that led to the Bigelow Expandable Activities Module (BEAM) demonstration on the ISS, the first ever human occupied inflatable module. The module was docked to the aft port of the ISS Tranquility node in April 2016, and it is still in operation. The inflation process progression can be seen in Figure 1.18.

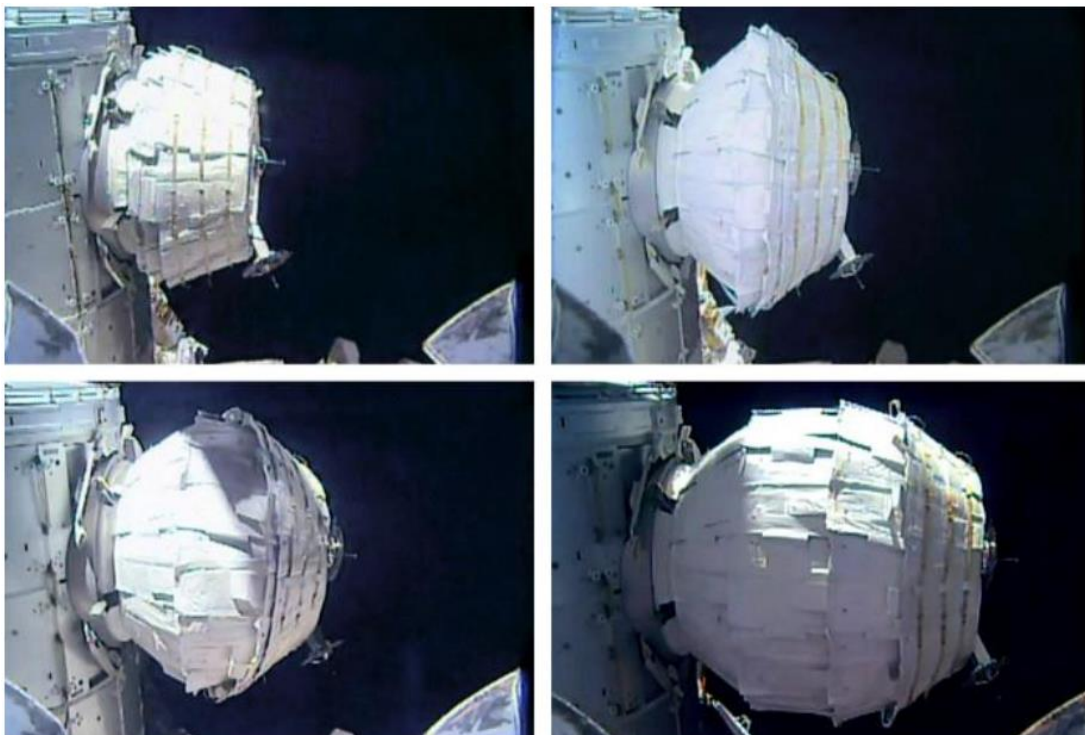


Figure 1.18: BEAM module inflation progression, from top left to bottom right [71].

1.6.2 EMU spacesuit

A spacesuit is a garment necessary for extravehicular activity (EVA), worn by humans to face the harsh environment of outer space, vacuum, and temperature extremes. Space suits are usually worn as a safety precaution inside spacecrafts in case of loss of cabin pressure. In order to allow safe and comfortable working, the primary requirements that a space suit must provide are a stable internal pressure, good mobility, the supply of breathable oxygen and elimination of carbon dioxide, temperature regulation, a communication system and a place to collect solid and liquid bodily waste. Secondary requirements include the shielding against UV and particle radiation and the protection against small micrometeoroids [72].

The Extravehicular Mobility Unit (EMU) is an independent spacesuit that provides mobility, environmental protection, life support and communications for astronauts during EVA in Earth orbit. It is currently one of the two types of EVA spacesuits used by crew members on the ISS and was introduced in 1981 [73]. It allows the redesign and substitution of each component without the modification of the whole suit, following the modular philosophy [50]. Figure 1.19 shows the fabric material layup used for the arms and legs of the EMU in order to protect the astronaut from the space environment.

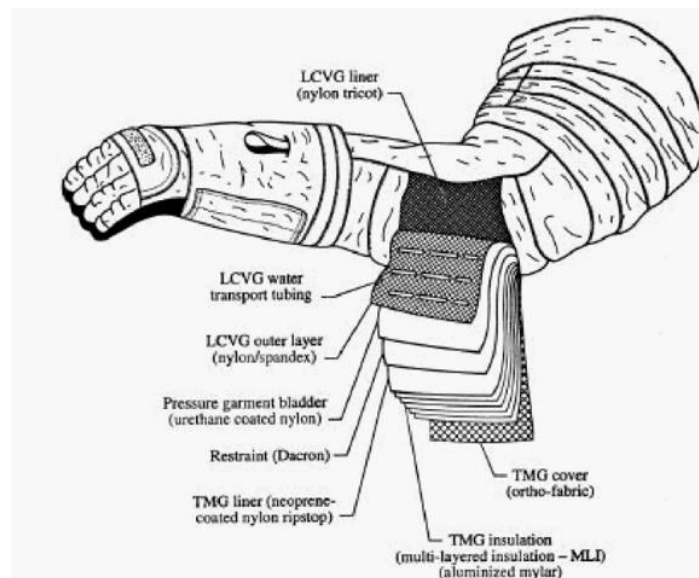


Figure 1.19: Fabric material layup used for the arms and the legs of the EMU [74].

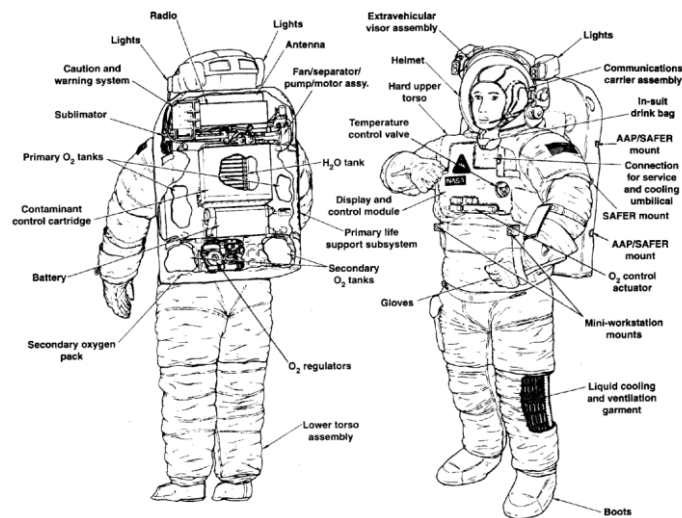


Figure 1.20: Major components of the EMU space suit assembly and support system [74].

1.7 Research objectives

The main purpose of this master's thesis is to assess the change in the healing performance of candidate self-healing polymers for space applications, presented in section 2.1, due to exposure to a simulated space environment.

The samples were provided by the European Space Agency (ESA) and subjected to radiation tests performed with the Co60 facility at ESA ESTEC in the Netherlands. The aim of these tests was to reproduce the effect of prolonged exposure to cosmic particles encountered in orbit and during space travel. Two sets of the considered self-healing polymers were therefore subjected to γ -ray exposure for 100 and 500 krad absorbed dose respectively.

The assessment of the self-healing response was done by measuring the flow rate during puncture tests, performed using the appropriate facility in the laboratory of the department of aerospace science and technology of Polytechnic of Milan. Once the flow rate data of the tests for the irradiated samples had been collected, they were compared with those relative to the puncture tests performed on a set of the same non-irradiated polymers, under the same test conditions, thus assessing the effect of exposure to spatial radiation on the healing performance.

Thermal and spectroscopic characterizations were carried out for the sample sets, before and after exposure, to assess possible changes in the mechanical, physical, and self-healing properties as a consequence of irradiation.

2. Materials and Methods

This Chapter is divided in two sections. The first section deals with the introduction of the self-healing polymers considered in this study, together with the preparation of the samples. Those, due to their properties, are candidate self-healing polymers for space applications. The second section describes the baseline characterization performed on them, which includes ATR-FTIR, DSC and TGA analysis, together with radiation tests and puncture tests.

2.1 Materials tested

The materials tested, characterized, and reported in this thesis study are poly(urea-urethane)s (PUUs) and Reverlink® HR. Those materials were supplied by European Space Agency (ESA).

2.1.1 Poly(urea-urethane)s

Poly(urea-urethane) is a type of polyurethane (PU) block copolymer with different physical properties and better healing performances due to the use of diamines as chain extenders and crosslinking agents [14, 18]. The presence of two different types of N-H bonds in the urethane and urea linkages makes the structure of this group of polymers more complex, with increasing bonding properties compared to other PUs [14].

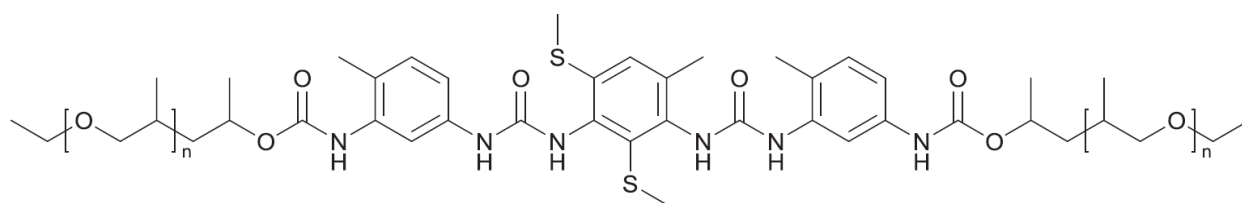


Figure 2.1: Typical chemical formula of a PUU molecule.

Cross-linked aromatic disulfide-based PUUs offer a fascinating solution due to their unique ability to repair damage at room temperature, without requiring catalysts. Additionally, these materials exhibit mechanical properties similar to those of traditional polymers.

The healing mechanism involves the formation of two distinct chemical bonds: a reversible supramolecular noncovalent interaction, performed by hydrogen bonding, and a reversible covalent bond of disulfide bridge. These disulfide connections serve

as linkers between aromatic groups and play a role in enhancing the material's elastic response [31]. The presence of hydrogen bonds has significant importance in the healing process of these PUUs. These bonds facilitate molecular interactions along the scratched interface, even before interdiffusion processes begin. This characteristic is fundamental for the healing process of these materials.

Since PUUs are thermoset polymers, melting will never take place, and this is very helpful in forming specific shapes after heating. However, degradation could take place in solid phase due to overheating.

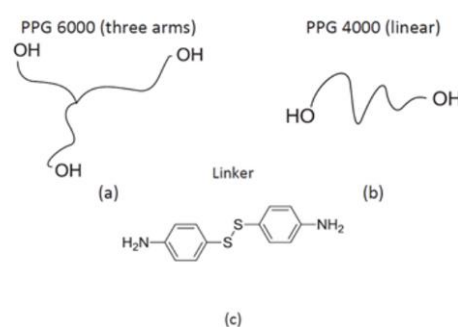


Figure 2.2: (a) trifunctional PPG, (b) bifunctional PPG, (c) disulphide linker [14].

PUUs samples with fixed disulphide content but different crosslinking densities were analyzed. The synthesis was performed using different combinations of trifunctional and difunctional polyurethane pre-polymers (PU 6000 and PU 4000), organized in networks. Those networks contain urea related H-bonds and are connected by aromatic disulphides linkages, Figure 2.3. Figure 2.2 shows chemical sketches of the two pre-polymers and the linker. The choice of the pre-polymers made possible to maintain the crosslinker quantity constant since the equivalent weight of a chain between an isocyanate moiety and a crosslinking point is always 2000 g mol^{-1} [14].

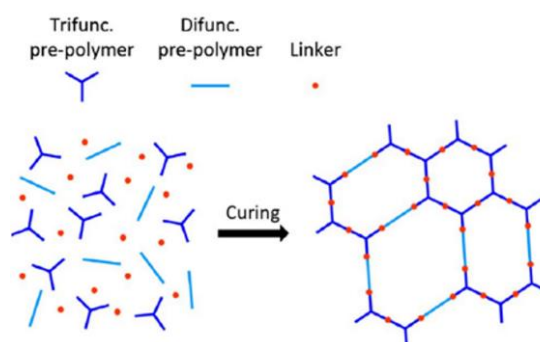


Figure 2.3: Curing process [14].

The synthesis steps of the two pre-polymers were carried out in accordance with the procedure described by Rekondo et al. [13]. Chemical compounds involved for PUUs synthesis are listed in Table 2.1.

Table 2.1: Chemical compounds involved in PUUs synthesis.

Name	Nomenclature	Mn	Percentage
Trifunctional Poly(propylene glycol)	PPG 6000	6000 g/mol	
Linear difunctional Poly(propylene glycol)	PPG 4000	4000 g/mol	
Isophorone diisocyanate	IPDI		98%
Isophorone diisocyanate	IPDI		98%
Tetrahydrofurane	THF		

Four different polymers were created by varying the trifunctional:difunctional pre-polymer ratio from 100:0 to 70:30 [14]. They contain the same density of disulfide and hydrogen bonds but differ in the degree of cross-linking (while maintaining a similar glass transition temperature (T_g)). The density of the obtained PUUs samples is about 1 g/cm³.

Table 2.2: Formulation and basic properties of the PUUs considered [14].

Sample	Composition* [wt%]		v [10^{-4} mol/cm ³]	T_g [°C]
PUU	PU-6000	PU-4000		
100	93.8	0	2.35	-58.8
90	84.4	9.4	2.05	-59
80	75.1	18.7	1.77	-59.4
70	65.7	28.1	1.50	-60.1
*Linker wt%: 6.2				

2.1.2 Reverlink® HR

An example of a commercially available supramolecular polymer is Arkema's Reverlink® HR (Figure 2.4). It contains both weak reversible supramolecular hydrogen bonds and strong irreversible covalent bonds (50:50 mol%). This polymer exhibits a rapid intrinsic self-healing mechanism at room temperature, attributed to the reversible hydrogen bonds within its structure. It is composed of 70% vegetal carbon and its characteristics stem from the combination between supramolecular assembly and chemical curing, enhancing its overall cohesion. Reverlink® HR

necessitates processing via mold casting as it can be poured as a liquid paste at approximately 90°C. The curing process demands several hours at temperatures ranging from 120 to 150°C [29].



Figure 2.4: Arkema's Reverlink® HR.

This polymer can be obtained combining supramolecular pre-polymer SP-50, diglycidyl ether of bisphenol A (DGEBA) resin and 2-Methyl Imidazole (2-MI) catalyst, with the proportions listed in table [51, 52]. It has a density of 1.09 g/cm³ and a glass transition temperature between 5 °C and 15 °C.

Table 2.3: Reverlink® HR components' mass [51].

Component	SP-50	DGEBA	2-MI
Mass (g)	23.9	6.02	0.004

2.1.3 Samples manufacturing

The samples used for the baseline characterization were obtained from initial slabs or disks of material. In the case of PUUs, 2 mm-thick slabs were already available and there was no need to obtain them.

In order to obtain Reverlink® HR, first precursors were mixed at 90 °C (Figure 2.5a) following the proportions indicated in Table 2.3, obtaining the non-cured material, that was subsequently poured into a circular Teflon® mold (Figure 2.5b) and cured for 24 hours at temperatures in the range of 120-150 °C [50]. The final obtained circular disk presents a thickness that varies between 1.7 and 2.1 mm (target thickness was 1.8 mm) due to some inhomogeneity (Figure 2.5c).



(a) Precursor mixing.



(b) Material poured in the mold



(c) Final disk.

Figure 2.5: Preparation of the Reverlink® HR disk [50].

All the samples were degassed for at least 15 hours in vacuum at room temperature in order to minimize as much as possible the effect of humidity on their properties, and then kept in a desiccator with silica gel before undergoing each test.

For the ATR-FTIR circular samples with a diameter of 25 mm, obtained from each slab or disk, were used, while smaller samples with weights in the order of milligrams for the DSC and TGA analysis.

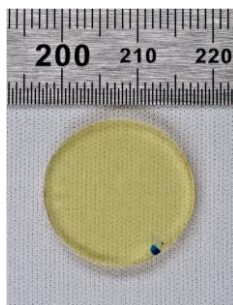


Figure 2.6: PUU80 circular sample [50].

2.2 Methods of tests

Methods, parameters and conditions under which the tests were performed on the PUUs and Reverlink® are presented in this section.

The described baseline characterization was performed mostly in the TEC-Q laboratory at the ESTEC branch of the European Space Agency (ESA) in the Netherlands [50].

2.2.1 DSC Analysis

Mettler Toledo DSC 822e module (Figure 2.7 (a)) in nitrogen with 50 ml/min flow rate, using 40 μ l aluminum crucibles, was used to perform the DSC analysis on the self-healing polymer samples immediately after they were manufactured.

Initially, a decreasing temperature ramp was performed at 20 $^{\circ}$ C/min from 25 $^{\circ}$ C to -110 $^{\circ}$ C and then, after an isothermal step, the temperature is increased up to 150 $^{\circ}$ C keeping the previous 20 $^{\circ}$ C/min ramp. The cycle is repeated after reaching again the temperature of -110 $^{\circ}$ C. The performed DSC analysis followed the typical procedure, in which the repetition of the thermal cycle is present, and the starting temperature is usually set at least 50 $^{\circ}$ C below the expected glass transition temperature of the analyzed materials [50].

Another DSC analysis was performed on blank and irradiated Reverlink® HR samples after 1 year of manufacturing, in order to assess possible changes in the T_g due to aging.

Those analyses were done using a TA Instruments® DSC 2010 (Figure 2.7 (b)) and Universal Analysis software in the DAER (Dipartimento scienze e tecnologie Aerospaziali) Laboratory of Politecnico di Milano.

In this case the thermal steps performed were the same as the other ones, with the only difference that the minimum temperature was -50 °C and not -110 °C since the instrument was not able to go below -50 °C due to the absence of liquid nitrogen.

The main aim of the analysis was to measure how the glass transition temperature of the considered samples changes along with the temperature.



(a) Mettler Toledo DSC 822e rheometer [50].



(b) TA Instruments® DSC 2010.

Figure 2.7: DSC instruments.

2.2.2 TGA Analysis

Mettler Toledo TGA/DSC 3+ device in nitrogen (Figure 2.8), at 70 ml/min from 25 °C/min with a 20 °C/min ramp, using $70\text{ }\mu\text{l}$ alumina crucibles, was used to perform the TGA analysis on the self-healing polymer samples. For each material two different samples were tested in order to prove the homogeneity of properties within the sample batches [50].

The main aim of this analysis is to evaluate the temperature range within which the considered polymers remain stable.



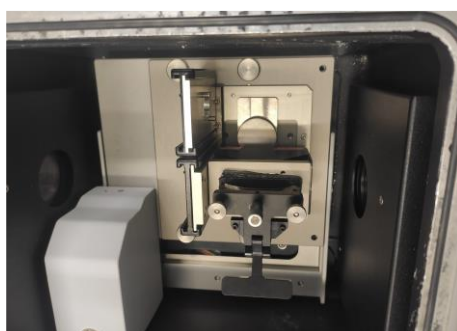
Figure 2.8: Mettler Toledo TGA/DSC 3+ device.

2.2.3 ATR-FTIR characterization

The aim of the ATR-FTIR characterization was to identify the chemical substances and functional groups of the analyzed samples by determining and looking at their spectra.

Bruker VERTEX 70v FTIR spectrometer with germanium (Ge) crystal setup (Figure 2.9) was used to acquire the needed information to build the ATR spectra of the tested materials, precisely in the wavenumber range from 650 to 4000 cm^{-1} . In order to prevent the contamination of the just characterized sample, that could compromise in this way the results of the test, the Ge crystal was cleaned right after each measurement [50].

The signal gain, scanner velocity and background scans number were set to 8, 5 kHz and 64 respectively.



(a) Experimental setup, top view.



(a) Germanium crystal.

Figure 2.9: VERTEX 70v spectrometer configuration [50].

2.2.4 Irradiation Test

To assess the effects of radiation dose in space environment on self-healing properties of PUUs and Reverlink®, the samples were subjected to irradiation tests. The set of irradiation tests was performed in air with the Co60 facility at ESA-ESTEC (Figure 2.10).

Cobalt-60 is a radioactive isotope of cobalt, produced artificially since it is not present in nature due to its short half-life time of 5.27 years [67]. It is capable of emitting high doses of extremely penetrating γ -rays and for this reason it is used to simulate an approximated radiation environment, reproducing the effect of the exposure to cosmic particles encountered in orbit [68].



Figure 2.10: Co60 irradiation facility at ESA ESTEC [68].

The facility used to simulate the space radiation environment using the Co60 replicates the lifetime effects of cumulative radiation doses, simulating years of exposure within just few days [68].

The material's samples presented in this thesis were divided in two batches and irradiated with a total ionizing dose in silicon of 100 and 500 krad (corresponding to 1000 and 5000 Gy respectively). Preceding the irradiation, the batches were contained into a sealable bag in which air was replaced with nitrogen, obtaining in this way a dry atmosphere and ideally removing the effect of humidity on materials. Table 2.4 shows the environmental conditions during the irradiation test.

Table 2.4: Environmental conditions during the test [50].

	Temperature [°C]	Pressure [mbar]	Rel. humidity [%]
Min	23	1003.1	43.9
Max	23.2	1029.5	51.6

The irradiated Reverlink® and PUUs samples were subsequently subjected to DSC, TGA, ATR-FTIR characterization and puncture tests, in order to assess the effects of γ -radiation dose on their self-healing properties.

2.2.5 Puncture Test

The aim of the puncture test is to assess the self-healing performances of the investigated polymer, following the puncturing of a hole through it. A dedicated test device is designed and assembled for the purpose.

The device's main apparatus is the cylindrical pressure vessel (Figure 2.12 (b)). It is made all of aluminum and consists of a central body, a bottom cap and an upper sealing ring, held together by screws so as to prevent air leakage when the pressurization system is active. The bottom cap remains closed, while the upper sealing ring is disassembled and reassembled in order to change and hold the samples during the puncturing tests (Figure 2.11). The upper sealing ring has three 6.4 mm diameter holes, located at a distance of 20 mm from the plate center, under which the samples to be punctured are positioned.



(a) Open cylindrical vessel



(b) Upper sealing ring with specimen



(c) Closed cylindrical vessel

Figure 2.11: Cylindrical pressure vessel

Puncturing is done using a puncturing tool, which consists of a puncturing needle and a perforated cylindrical part (Figure 2.12 (a)). The latter can be fixed by grips to tensile testing machines or other devices able to move the needle in a controlled manner to puncture the sample. The puncturing needle used has a diameter of 2 mm, which will be the diameter of the hole created in the sample.

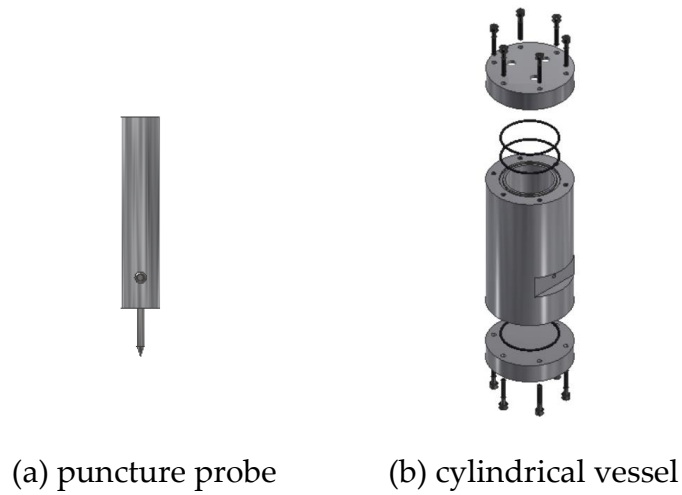


Figure 2.12: Schematic representation.

The cylindrical pressure vessel has two threaded holes to connect it with a pressure transducer and a small pipe of 6 mm external diameter through which air is supplied. Before reaching the cylindrical vessel, air must pass through a pressure regulator, a finger valve and a flow meter. The illustration of the complete setup is shown in figure.

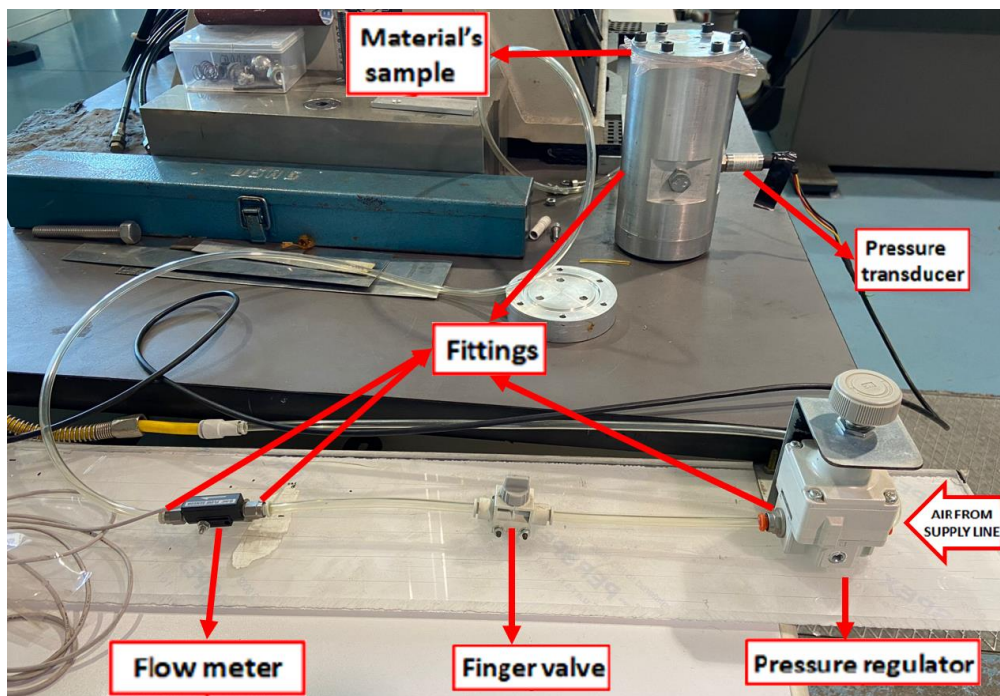


Figure 2.13: Test setup.

The two most important devices in the setup are the Pressure Sensor Limited® PSC217-B-4-5-A pressure transducer and the SMC® PFMV530-1 flow meter. The pressure transducer measures the difference between the ambient pressure and the cylinder's inner pressure, while the flow meter monitors the volumetric flow rate exiting from the cylinder (from the hole generated by the puncture probe or from other leakage sites). The flow meter considered for the tests has a maximum measurable flow rate of 3 *l/min*, lower compared to other commercially available sensors, but has a higher accuracy, which allows the correct acquisition of very small flow rates values expected in the final part of the puncture tests.

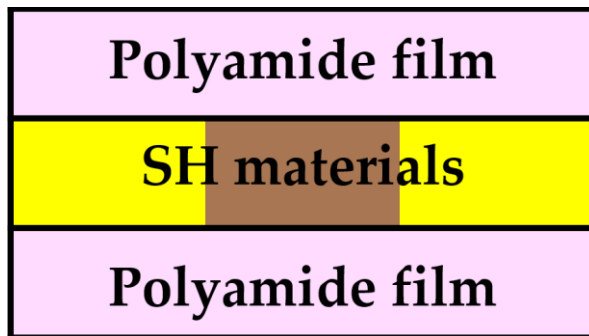
Both the flow rate and the differential pressure sensors are powered by an electrical DC power supply and produce analogue output signals (in Volts). For data acquisition they are connected to a terminal box linked to a computer. A dedicated software LabVIEW® converts the incoming voltages, output of the sensors, to the desired physical quantities (*l/min* for the flow rate and *bar* for the pressure) and plots their variation in time. There is a linear relationship between the electrical potential value of the pressure sensor and the pressure value, while a non-linear relationship between the electrical potential value of the flow rate sensor and the flow rate value. The sensor's main parameters are reported in Table 2.5.

Table 2.5: Instruments main properties.

Property	Pressure transducer	Flow meter
Supply voltage [VDC]	4.75-5.25	12-24
Measurement range	10 <i>bar</i>	0-3 <i>l/min</i>
Output voltage [V]	0.5-4.5	1-5
Accuracy/repeatability	±1% FS	≤ ±2% FS

The flow meter, the SMC® VHK2-06F-06F finger valve and the SMC® IR2000-F02 pressure regulator, are fixed on a plexiglass support.

Concerning the testing procedures, all the samples were packed between two 50 μm thick polyamide films before being fixed on the cylindrical pressure vessel via screws (Figure 2.14). Subsequently, the system is pressurized to a relative pressure of 0.3 *bar* and continuously supplied with air, in order to reproduce the internal environment of the EMU spacesuit. After checking that no air leakages are present in the system, the pressurization step is completed, and the puncture test can start.



(a) Layup illustration.

(b) Samples between polyamide layers.

Figure 2.14: Example of samples between polyamide films.

The puncture probe is fixed via grips in the MTS 858 Mini Bionix® II machine (Figure 2.15 (a)), exploited to impose a vertical sinusoidal motion to the puncheon. An amplitude of 9.62 mm and a frequency of 0.14 Hz were set to obtain a velocity of 8.467 mm/s when the puncturing tool penetrates the specimen through the holes in the aluminum disk on top. The testing procedure was performed according to the ASTM F1342/F1342M-05 standard (test method A) [76].



(a) MTS 858 Mini Bionix® II machine.



(b) Puncture event.

Figure 2.15: Puncture test machine and puncture event.

The finger valve is left open to provide a continuous supply of air to the system. As soon as the puncture has occurred, a peak of the flow rate can be seen on the acquisition software. It is caused by an outflow of air due to the pressure difference between the atmospheric pressure and the cylinder's inner one. The value of the flow rate tends to decrease at a rate depending on the healing performance of the material. The hole is considered closed, and therefore a self-repair occurred, when the flow rate value is zero, or at least less than 0.001 l/min.

Three tests were performed for each irradiated sample to allow a sufficient reliability of the obtained results. The average values, standard deviation of maximum flow rate, minimum flow rate, time between maximum and minimum flow rates and total leaked volume are computed for each specimen, according to NASA test campaign described. Those parameters are collected as self-healing performance indicators, following procedures from past literature [75].

After each successful puncture test, a leakage test was performed on the same sample. This consisted of three steps, in which the pressure was increased from 0.3 to 0.5 *bar*, from 0.5 to 0.6 *bar* and finally from 0.6 to 0.8 *bar*. The leakage test was considered passed if, after each step, the flow rate dropped to 0 *l/min* (after about 15-20 s). The point of this test was to assess whether the flow rate going to a null value after the puncture test was due to a simple elastic recovery of the sample or due to an actual repair. In the case of a simple elastic recovery, the pressure exerted during leakage testing would have been enough to keep the unrepaired hole open, thus exhibiting a flow rate greater than 0.001 *l/min*.

2.2.5.1 Preliminary outgassing

All tested samples were preliminarily degassed by placing them in a vacuum oven for at least 24 hours at room temperature in order to remove the moisture absorbed between manufacturing and testing (Figure 2.16 (a)).

Degassing the samples is extremely important as self-healing performance is highly dependent on absorbed moisture. In polyurethane (PU) based materials water occupies hydrogen bonding sites between interchain N-H and C=O, acting as a plasticizer, thus decreasing the T_g and the elastic modulus [77]. The masses are measured pre and post outgassing procedure and, together with the computed humidity concentration (HC), are reported in Table 2.6.

Table 2.6: Masses pre and post outgassing and humidity concentration in samples.

Blank	Mass pre (g)	Mass post (g)	HC %	100 krad	Mass pre (g)	Mass post (g)	HC %	500 krad	Mass pre (g)	Mass post (g)	HC %
PUU 70	1.115	1.107	0.723	PUU 70	1.086	1.079	0.649	PUU 70	1.017	1.011	0.593
PUU 80	1.109	1.101	0.727	PUU 80	1.153	1.146	0.611	PUU 80	1.11	1.102	0.726
PUU 90	1.215	1.205	0.830	PUU 90	1.063	1.055	0.758	PUU 90	1.163	1.156	0.606
PUU 100	1.189	1.180	0.763	PUU 100	1.21	1.201	0.749	PUU 100	1.14	1.133	0.618
Reverlink®	0.916	0.914	0.219	Reverlink®	0.909	0.905	0.442	Reverlink®	0.807	0.804	0.373

Once outgassing procedure is completed, each sample is stored inside a glass dryer (Figure 2.16 (b)).



(a) Outgassing oven



(b) Glass dryer

Figure 2.16: Oven and dryer apparatus in DAER laboratory.

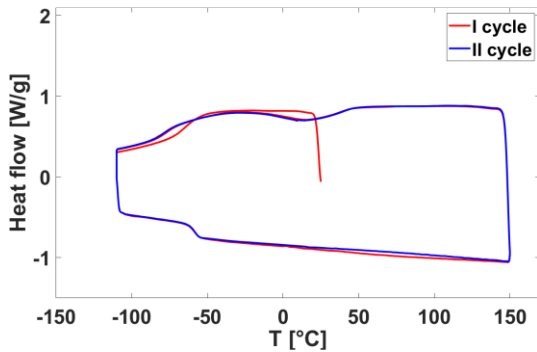
3. Results

3.1 DSC

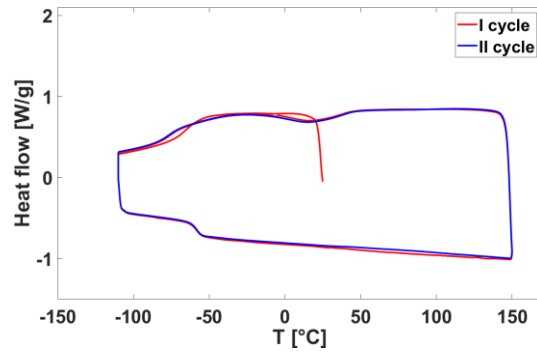
TRIOS software from TA® instruments was used to postprocess and compare DSC data obtained from tests.

3.1.1 Blanks

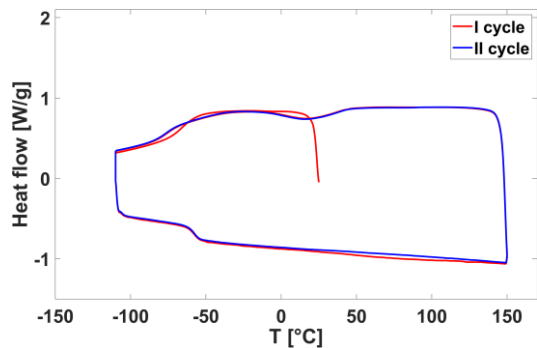
Figure 3.1 and Figure 3.2 show the DSC results for the different PUUs polymers and for Reverlink® respectively [50]. As we can see, the DSC curves for the four PUUs are very similar to each other, with only very small differences. No relevant distinctions are observed between the two cycles for the polymers tested, except from the initial cooling phase from 25 °C to -110 °C in the first cycle and a small right shift in the second cycle for Reverlink®.



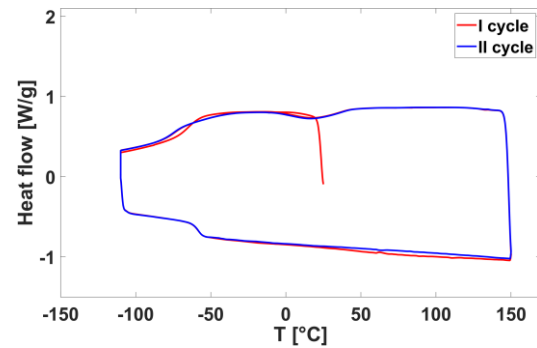
(a) PUU 70



(b) PUU 80



(c) PUU 90



(d) PUU 100

Figure 3.1: DSC results for the different PUUs [50].

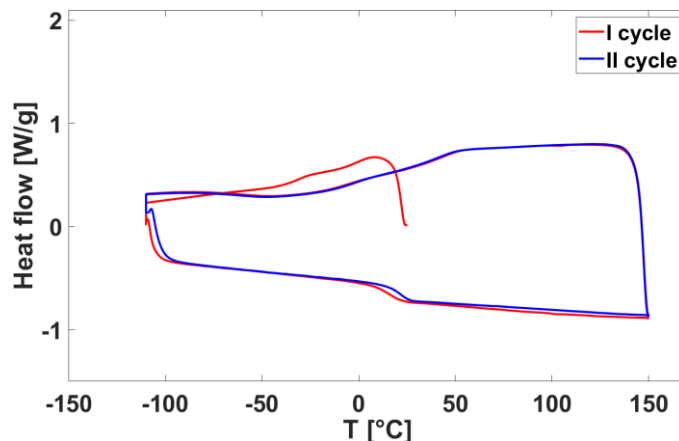


Figure 3.2: DSC result for Reverlink® [50].

The results in terms of glass transition temperature from the DSC analysis are schematized in Table 3.1. Considering the T_g values obtained for PUUs, they are consistent with the ones expected and listed in Table 2.2. However, as for Reverlink®, the T_g value found in the first cycle is consistent with the one expected, which ranges between 5 and 15 °C, while the T_g found in the second cycle is slightly higher, almost reaching a value of 21 °C. The reason for this may be related to inaccuracies in the mixing of precursors, such as maintaining the required proportions, during sample production.

Table 3.1: Glass transition temperatures T_g from DSC tests [50].

Sample	T_g [°C]	
	Cycle I	Cycle II
PUU 70	-59.05	-58.99
PUU 80	-58.28	-58.74
PUU 90	-58.12	-57.88
PUU 100	-58.59	-58.63
Reverlink®	13.93	20.97

3.1.2 Comparison between blank and irradiated samples

DSC curves for all the samples irradiated by 100 and 500 krad dose are determined and compared with the ones for blank samples. Those curves are shown in Figure 3.3 for PUUs and in Figure 3.4 for Reverlink® [50].

The 100 and 500 krad DSC curves for the different PUUs are essentially identical, except for PUU 70 where small variations in glass transition temperature and heat flow compared to blank curves are present. Due to a possible instrument or measurement

issue, the T_g point doesn't appear clearly in the first cycle of the 100 krad curve for PUU 70 (Figure 3.3 (a)). The experienced issue could be that the sample was not kept for long enough time at a low temperature, thus not equilibrating the system before proceeding to the heating ramp. This phenomenon, represented by the appearance and the progressive right shifting of something like an upside down "L", is also shown in the 500 krad Reverlink® curve.

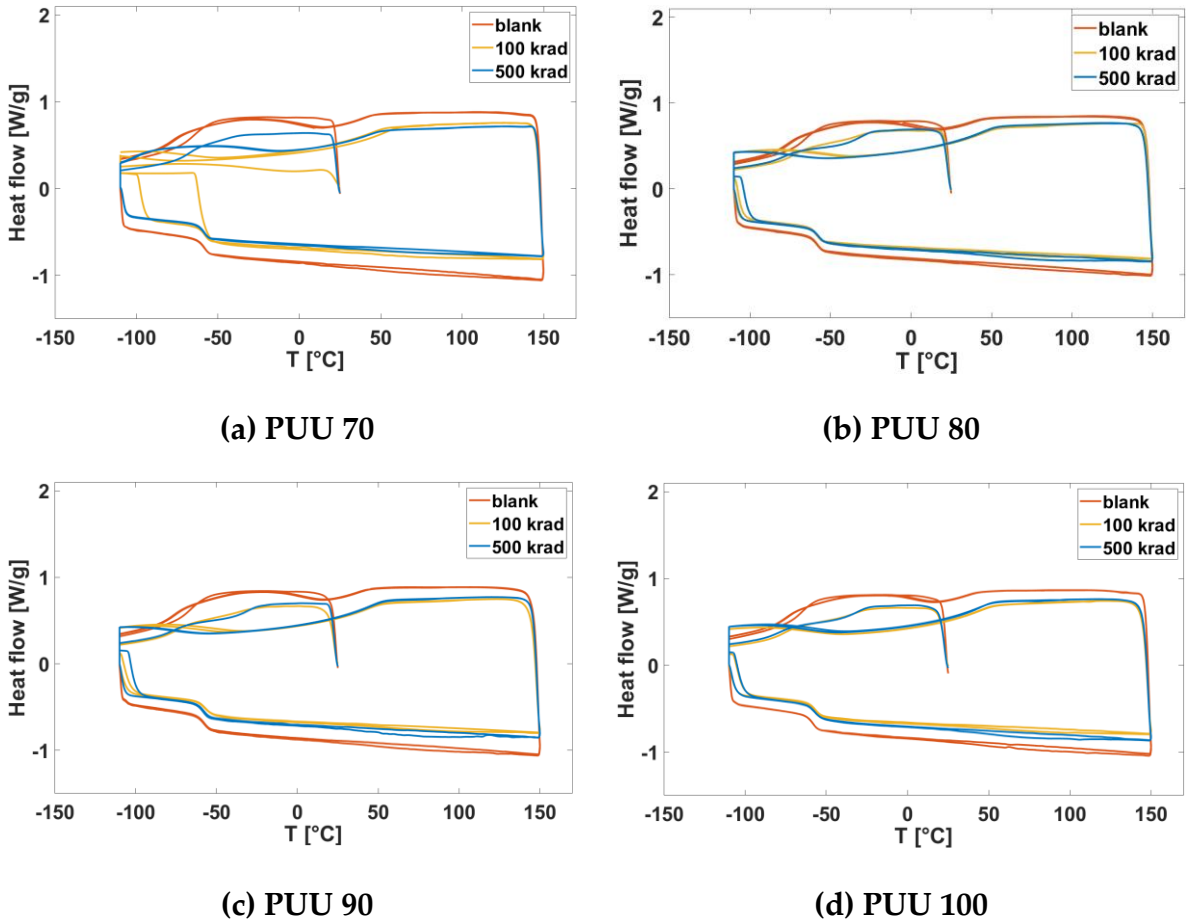


Figure 3.3: DSC results comparison of blank and irradiated PUUs [50].

Concerning instead the DSC comparison for Reverlink® results, the 100 krad and blank curves are very similar to each other, while the 500 krad curve present the right shifting previously introduced and a mild left shift of the T_g compared to the other curves.

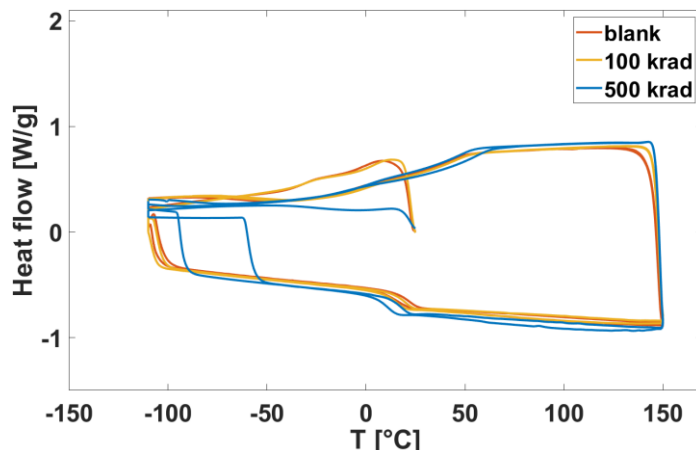


Figure 3.4: DSC results comparison of blank and irradiated Reverlink®.

Table 3.2 illustrates a comparison of the glass transition temperature values between blank and irradiated samples for the two cycles [50].

Table 3.2: T_g comparison between blank and irradiated samples.

Sample	T_g [°C]					
	Cycle I			Cycle II		
	Blank	100 krad	500 krad	Blank	100 krad	500 krad
PUU 70	-59.05	-	-58.64	-58.99	-59.10	-58.63
PUU 80	-58.28	-58.73	-57.92	-58.74	-58.76	-57.94
PUU 90	-58.12	-56.87	-58.45	-57.88	-57.09	-58.07
PUU 100	-58.59	-57.44	-56.99	-58.63	-57.30	-57.12
Reverlink®	13.93	14.85	9.78	20.97	19.43	17.19

No relevant changes can be seen from Table 3.2 due to irradiation, in particular for the PUUs, for which the T_g basically doesn't change. For Reverlink®, a slight decrease of about 4 °C in the T_g is shown passing from blank to irradiation dose of 500 krad.

3.1.2.1 Comparison between blank and aged Reverlink®

As introduced in 2.2.1, a DSC analysis was performed on blank and irradiated aged Reverlink®. The analysis was not performed on aged PUUs since the results would not show the T_g as the minimum reachable temperature by the instrument was -50 °C.

Figure 3.5 presents a comparison of the curves for the second cycle only, as for the first one several abnormal fluctuations were present due to possible instrument and measurement problems. Looking at the curves, there is a heat flow increase during heating and cooling passing from blank, 100 krad to 500 krad curves.

The right shift in the curve for 500 krad non-aged Reverlink® (Figure 3.4) is no more present here. The reason for this can hide in the different procedure and instrument involved in the analysis.

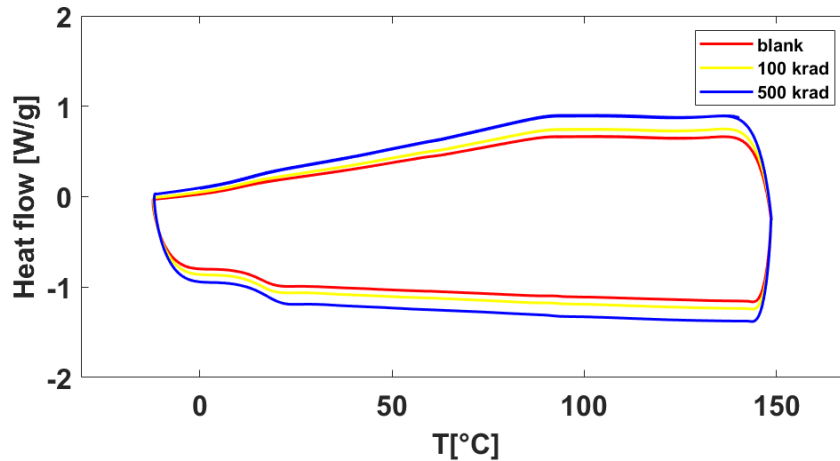


Figure 3.5: DSC results between blank and irradiated aged Reverlink®.

Table 3.3 illustrates a comparison for only the second cycle of the T_g results for Reverlink® aged and non-aged sample. A relevant difference can't be seen comparing the results, only a slight decrease of the T_g value for the blank sample and a slight increase for the 500 krad sample. The T_g value of the sample irradiated by 100 krad radiation dose remains basically the same after one year from manufacturing. In general, for aged Reverlink® the T_g is basically the same after irradiation.

Table 3.3: Aged and non-aged Reverlink® T_g comparison.

Sample	Cycle II T_g [°C]		
	Blank	100 krad	500 krad
Reverlink®	20.97	19.43	17.19
Reverlink® aged	19.05	19.47	19.45

3.2 TGA

3.2.1 Blanks

Table 3.4 illustrates degradation onset temperature $T_{5\%}$ and endset temperature $T_{95\%}$, determined at 5% and 95% of mass loss respectively, and maximum degradation temperature T_{max} determined at the peak of the first derivative of the TGA curve (DTG curve) for the two samples analyzed for each material. The values resulting from characterizing the two samples are very similar, meaning a good homogeneity within

the samples batches. For Reverlink®, no endset and maximum temperature are indicated since those values are not contained in the used 0-400 °C TGA temperature range, denoting a higher thermal stability than PUUs. The absence of T_{max} within this range is clear from the DTG curve in Figure 3.7, where no peaks are present.

Table 3.4: Thermal degradation temperatures from TGA analysis [50].

Sample	$T_{5\%}$ [°C]		$T_{95\%}$ [°C]		T_{max} [°C]	
	1	2	1	2	1	2
PUU 70	300.5	300.5	379.9	379.3	366.3	362.3
PUU 80	305.0	305.2	383.0	382.2	364.0	364.7
PUU 90	302.4	304.7	381.9	381.1	363.7	357.0
PUU 100	303.8	304.4	381.9	380.9	363.7	365.7
Reverlink®	377.6	371.5	-	-	-	-

The higher thermal stability of Reverlink® in that temperature range with the respect to PUUs is more evident by looking at TGA curves in Figure 3.6 and Figure 3.7. The plots show the weight percentage and the DTG curves only for the first sample, this because the curves related to the same material are basically the same.

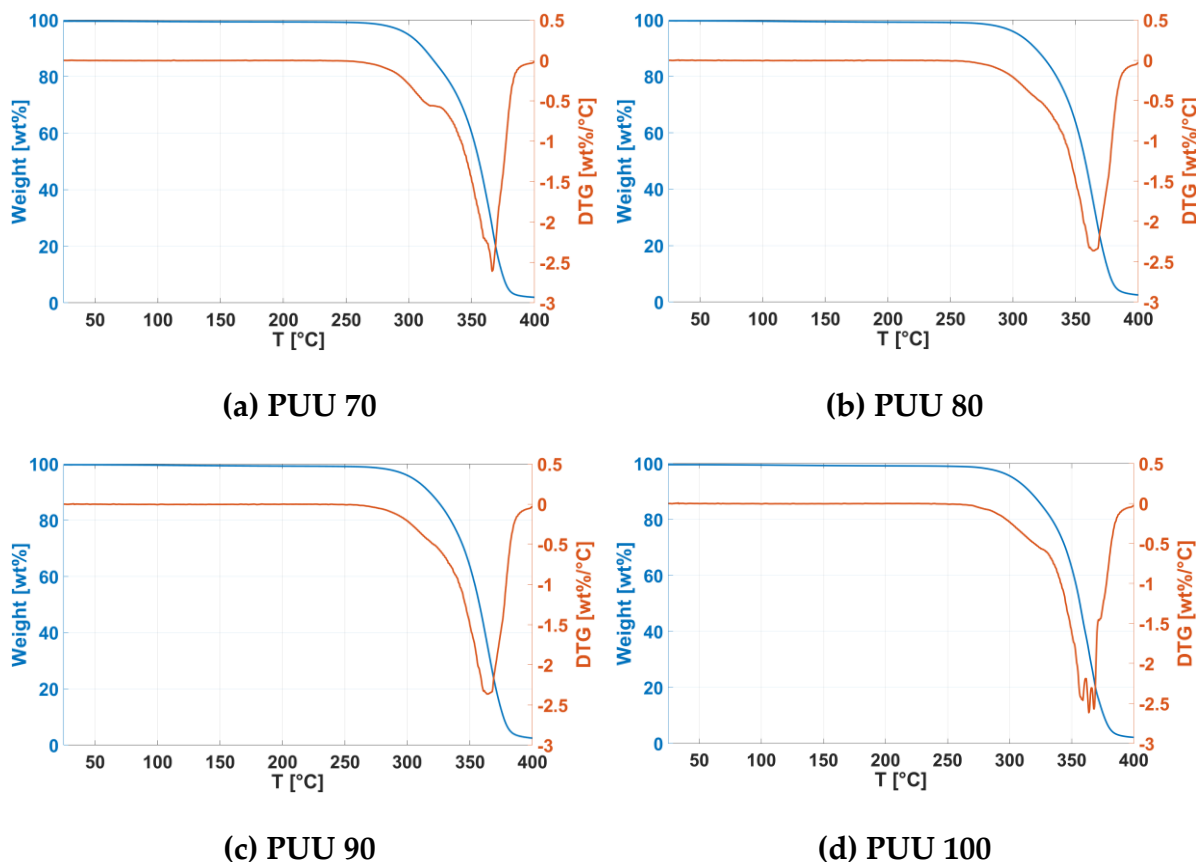


Figure 3.6: TGA curves results for PUUs [50].

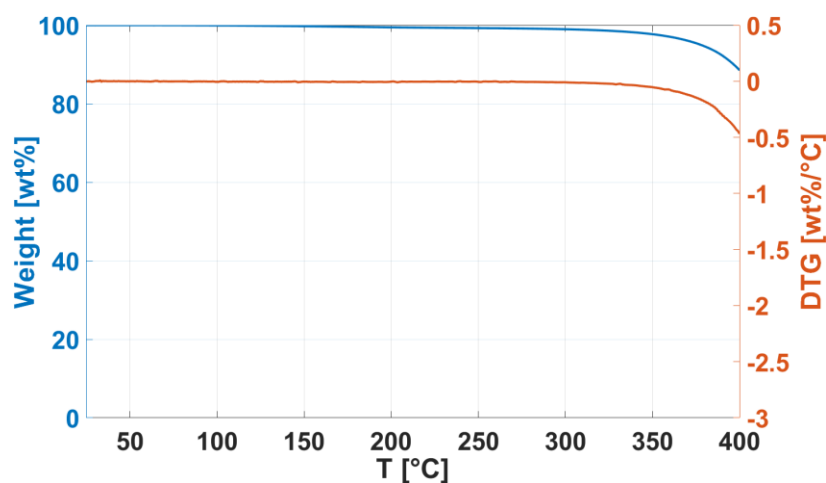


Figure 3.7: TGA curves results for Reverlink® [50].

3.2.2 Comparison between blank and irradiated samples

In Table 3.5 thermal degradation temperatures for blank and irradiated samples by 500 krad radiation dose are listed. The comparison was made only with the values of the first sample in Table 3.4 as the results of the two blanks are very similar.

After analyzing the TGA results for samples irradiated by 500 krad dose and noticing the absence of relevant changes compared to the results obtained for blank samples, it is decided to not characterize the remaining samples irradiated at lower dose (100 krad). It was assumed pointless, since even smaller variations would be observed for weaker irradiated samples compared to blanks [50].

Table 3.5: Blank and irradiated samples thermal degradation temperature [50].

Material	Conditioning	$T_{5\%}$ [°C]	$T_{95\%}$ [°C]	T_{max} [°C]
PUU 70	Blank	300.5	379.9	366.3
	500 krad	303.5	382.9	362.0
PUU 80	Blank	305.0	383.0	364.0
	500 krad	302.9	381.6	366.0
PUU 90	Blank	302.4	381.9	363.7
	500 krad	303.3	380.5	358.3
PUU 100	Blank	303.8	381.9	363.7
	500 krad	304.3	381.9	366.3
Reverlink®	Blank	377.6	-	-
	500 krad	374.1	-	-

3.3 ATR-FTIR

OMNIC software and the open source Spectragryph software were used to postprocess and compare the ATR-FTIR spectra resulting from tests.

3.3.1 Blanks

Infrared Spectra of blank polymers are determined and shown in Figure 3.8 and Figure 3.9 [50]. Figure 3.8 shows a comparison between the IR spectra of the PUUs with different crosslinking density.

All PUUs spectra are characterized by several peaks in the region between 3000 and 2850 cm^{-1} , typical of the C-H stretching related to aliphatic hydrocarbons, and a peak at around 3360 cm^{-1} , related to the stretching of the O-H group. The highest peak is in the fingerprint region at about 1105 cm^{-1} and is related to C=O stretching, while the shoulder at 1660 cm^{-1} is attributed to urea. The spectra are essentially the same for all the different PUUs, with the only difference in the wavenumber region from 2950 and 2800 cm^{-1} . Here it can be seen that a peak at about 2916 cm^{-1} is shown only by PUU 90 and PUU 100, and PUU 90 is characterized also by an additional peak at around 2850 cm^{-1} . Those different peaks are anyway related to the functional group of aliphatic hydrocarbons [50].

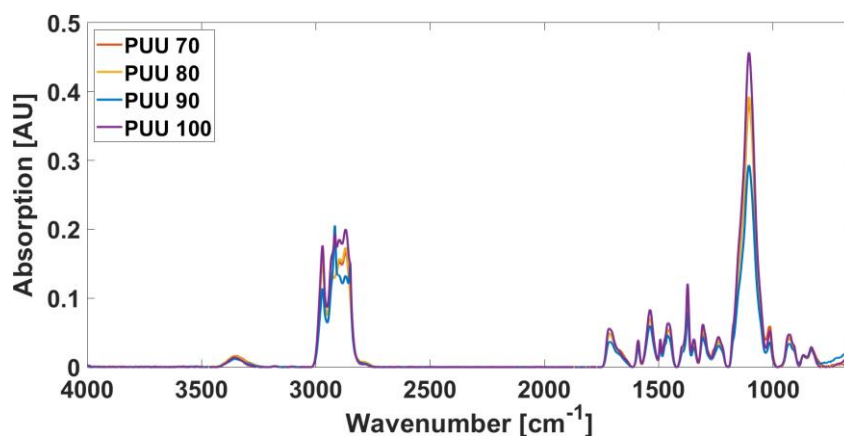


Figure 3.8: ATR-FTIR spectra comparison for PUUs [50].

Concerning Reverlink®, the peaks in the wavenumber range from 3000 to 2800 cm^{-1} are related to aliphatic hydrocarbons functional groups, while the ones between 1500 and 1400 cm^{-1} to aromatic hydrocarbons. The two highest peaks at 2917 and 2850 cm^{-1} might be due to either N-H or C-H stretching modes, while the peak at 2956 cm^{-1} is probably related to C-H stretching. The broad band in the 1736-1650 cm^{-1} range might be related to C=N or C=O stretching, while the peak at 1552 cm^{-1} to N-O stretching.

Finally, the peaks at 1470 and 1460 cm^{-1} could be attributed to the C-H bending mode of methylene group [50].

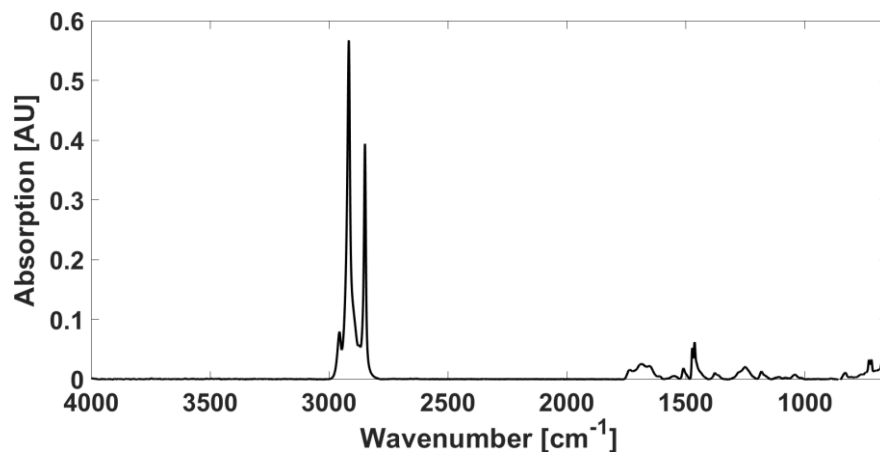


Figure 3.9: ATR-FTIR spectrum for Reverlink® [50].

3.3.2 Comparison between blank and irradiated samples

Infrared spectra of all samples irradiated by 100 krad and 500 krad radiation dose are determined and subsequently compared to the ones for the blank materials. Figure 3.10 to Figure 3.13 show the comparison for PUUs polymers, while Figure 3.14 for Reverlink®.

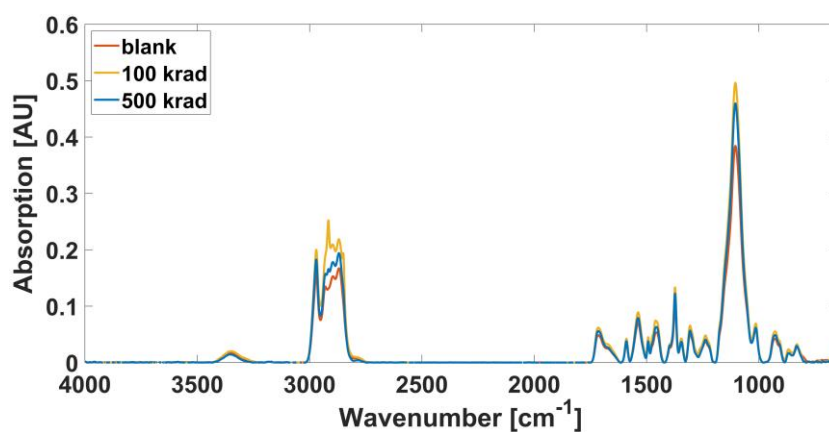


Figure 3.10: ATR-FTIR spectra comparison of blank and irradiated PUU 70.

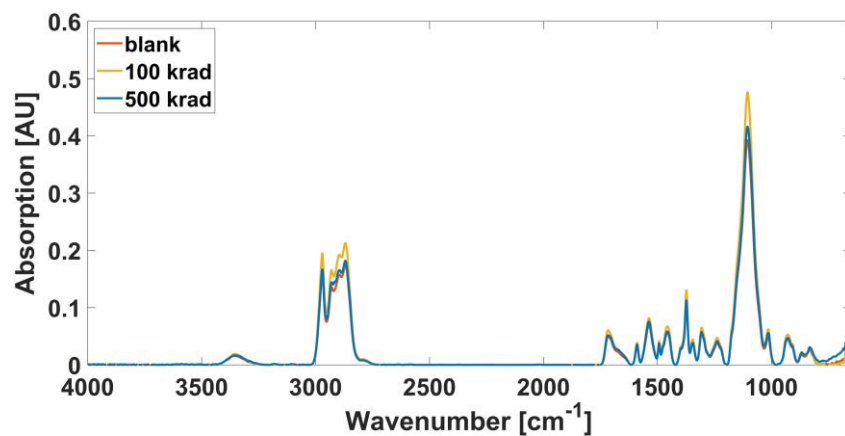


Figure 3.11: ATR-FTIR spectra comparison of blank and irradiated PUU 80.

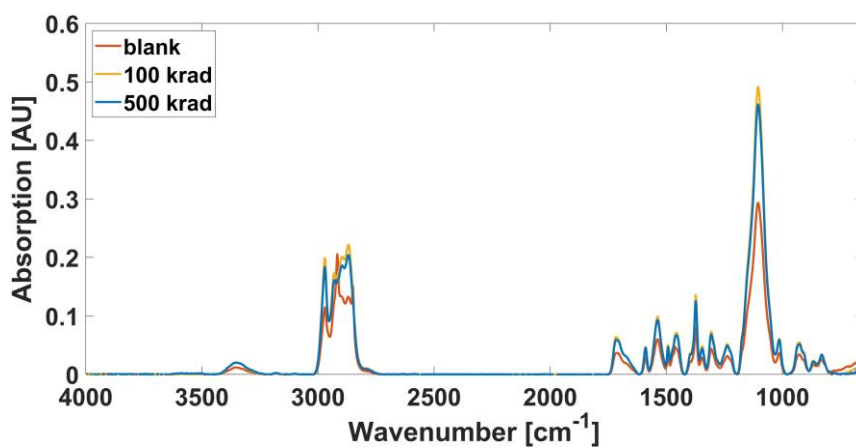


Figure 3.12: ATR-FTIR spectra comparison of blank and irradiated PUU 90.

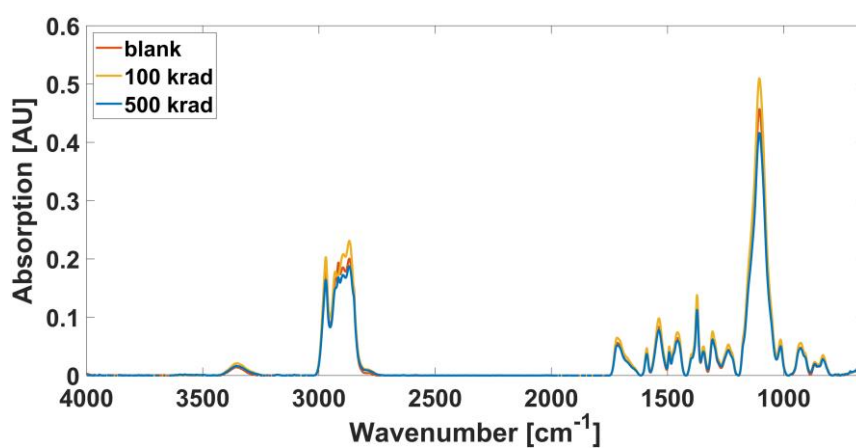


Figure 3.13: ATR-FTIR spectra comparison of blank and irradiated PUU 100.

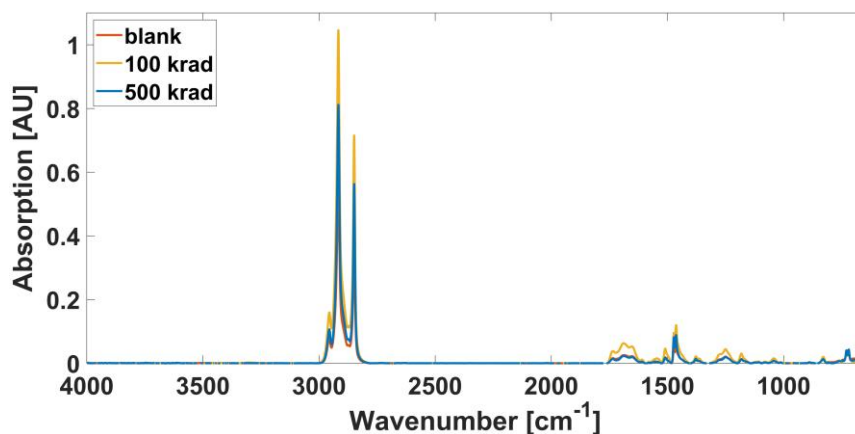


Figure 3.14: ATR-FTIR spectra comparison of blank and irradiated Reverlink®.

No relevant differences emerge from comparisons with irradiated samples. This means that the irradiation did not lead to any significant changes to the functional groups and in general to the chemical structure of the polymeric materials tested.

3.4 Puncture test

Matlab® was used to postprocess the obtained puncture tests data. The maximum and the minimum flow rate, Q_{max} and Q_{min} , the time in between the two Δt (healing time) and the total volume lost V_{leak} were considered as healing performance indicators. The mean value and the standard deviation σ were also computed and collected in the relative tables for each set of tests.

For the determination of V_{leak} the trapezoidal rule was applied for each curve to numerically integrate the flow rate over time. The air volume lost during the healing process is a fundamental parameter, as it has to be as low as possible to ensure the highest possible safety for crew members. Associated with it, the polymer clearly needs to reach the minimum flow rate in the shortest possible time. Healing is effective only if it is achieved within few minutes after the puncture event and is related to a contained leakage.

Furthermore, the thickness of the punctured sample's region is reported, since a relationship between the thickness and the healing performance is expected.

The test time considered for PUUs was 250 s, while for Reverlink® 500 s. This difference was due to the different healing efficiency of the two types of polymers, with PUUs that show a lower Δt , so a faster healing, with the respect to Reverlink®.

As anticipated in section 2.2.5, the measurable limit of the flow meter is 3 *l/min*; this leads to saturation in Reverlink® tests. In these cases, the flow rate peak is estimated through extrapolation after fitting the flow rate curve to an exponential model:

$$Q(t) = A \cdot e^{b \cdot t} + C \cdot e^{d \cdot t} + q \quad (3.1)$$

The fitting was performed exploiting the Matlab® Curve Fitting Tool. $Q(t)$ is the volumetric flow rate as a function of time t and q is a positive term allowing for possible non-zero minimum flow rates. A and C are set as positive parameters in the tool options, while b and d as negative ones, in order to have the sum of two decaying exponential functions.

Previously to the fitting, the decreasing part of the flow rate curves as output of the puncture tests was isolated in a specific vector, then uploaded into the fitting tool.

3.4.1 Blanks

Table 3.6 to Table 3.10 illustrate the results of the puncture tests performed on blank PUUs and Reverlink® samples respectively, immediately after the manufacturing [50].

PUU samples successfully pass all the tests, fully repairing themselves within tens of seconds with a very contained air volume loss for the purposes. The nominal thickness of tested PUU samples was of 1 mm, meaning that this polymer is suitable for space applications like space suits. Leakage tests confirm the damage recovery for all the tests.

Table 3.6: Puncture test results for PUU 70 blank [50].

Test	Q_{max} [l/min]	Q_{min} [l/min]	Δt [s]	V_{leak} [L]
1	1.8301	0	8.06	0.0092
2	1.7026	0	8.80	0.0080
3	1.9495	0	17.02	0.0213
Mean	1.8274	0	11.29	0.0128
σ	0.1235	0	4.97	0.0073

Table 3.7: Puncture test results for PUU 80 blank [50].

Test	Q_{max} [l/min]	Q_{min} [l/min]	Δt [s]	V_{leak} [L]
1	2.0438	0	29.37	0.0252
2	1.9652	0	8.25	0.0082
3	2.1047	0	6.78	0.0090
Mean	2.0379	0	14.80	0.0141
σ	0.0699	0	12.64	0.0096

Table 3.8: Puncture test results for PUU 90 blank [50].

Test	Q_{max} [l/min]	Q_{min} [l/min]	Δt [s]	V_{leak} [L]
1	1.3586	0	27.02	0.0035
2	1.6011	0	6.59	0.0027
3	1.8059	0	16.75	0.0079
Mean	1.5885	0	16.79	0.0047
σ	0.2239	0	10.22	0.0028

Table 3.9: Puncture test results for PUU 100 blank [50].

Test	Q_{max} [l/min]	Q_{min} [l/min]	Δt [s]	V_{leak} [L]
1	1.5894	0	6.32	0.0032
2	1.5076	0	7.15	0.0020
3	1.6909	0	9.06	0.0037
Mean	1.5960	0	7.51	0.0030
σ	0.0918	0	1.41	0.0008

Reverlink® is the worst performing material, it cannot fully repair itself in a reasonable time and consequently loses too much air volume (Table 3.10). According to these test results, it is not suitable for space applications such as space suits or habitats, which require fast damage recovery and contained leakage for safety reasons.

Table 3.10: Puncture test results for Reverlink® [50].

Test	th_p [mm]*	Q_{max} [l/min]	Q_{min} [l/min]	Δt [s]	V_{leak} [L]
1	1.41	6.5409	0.2305	488.99	6.4452
2	1.39	10.6022	0.0671	488.98	4.2598
3	1.53	13.1883	0.1642	488.40	6.3681
Mean	1.44	10.1105	0.1539	488.79	5.6910
σ	0.08	3.3508	0.0822	0.34	1.2401

* th_p = thickness of the punctured region

For this polymer, the thickness of the punctured region of the three tests is reported. Despite the much higher thickness with the respect to PUUs, it has far worst self-healing performance parameter results, especially looking at the total volume lost V_{leak} .

It is experimentally observed that the self-healing performance of a material improves by increasing its thickness [50]. Hence, in order to look for better and possibly satisfying results, the material thickness should be increased, with the risk, however, of having values that are too high for space applications, which require very thin layers (to have the lightest possible structures). The material could be considered for applications with less stringent requirements.

3.4.2 Blanks aged

Puncture tests were performed again on blank samples one year after the manufacturing. The reason for this was to check whether the results were congruent with those performed a year earlier. For this cause, only two tests were carried out on the blank aged samples. The thicknesses of the samples are illustrated in Table 3.11.

Table 3.11: Thicknesses of blank aged samples.

	PUU 70	PUU 80	PUU 90	PUU 100	Reverlink®
Thickness [mm]	2.06	2.05	2.23	2.14	1.91

Looking at Table 3.12, where self-healing performance parameters resulting from the performed tests are collected, it can be seen that all the samples successfully passed the test, except for PUU 90 in test 2.

Table 3.12: PUUs blank aged puncture test results.

Test	Q_{max} [l/min]	Q_{min} [l/min]	Δt [s]	V_{leak} [l]
PUU 70				
1	2.0887	0	116.83	0.07150
2	2.0254	0	91.82	0.03292
Mean	2.0571	0	104.33	0.05221
PUU 80				
1	1.9219	0	9.17	0.00408
2	2.5863	0	12.73	0.02460
Mean	2.2541	0	10.95	0.01434
PUU 90				
1	2.2098	0	75.16	0.03391
2	2.2208	0.006	249.79	0.07453
Mean	2.2153	0.003	162.48	0.05422
PUU 100				
1	1.8670	0	8.59	0.00937
2	2.1382	0	110.11	0.02990
Mean	2.0026	0	59.35	0.01964

Figure 3.15 shows the flow rate curves for all the four PUUs blank aged tested.

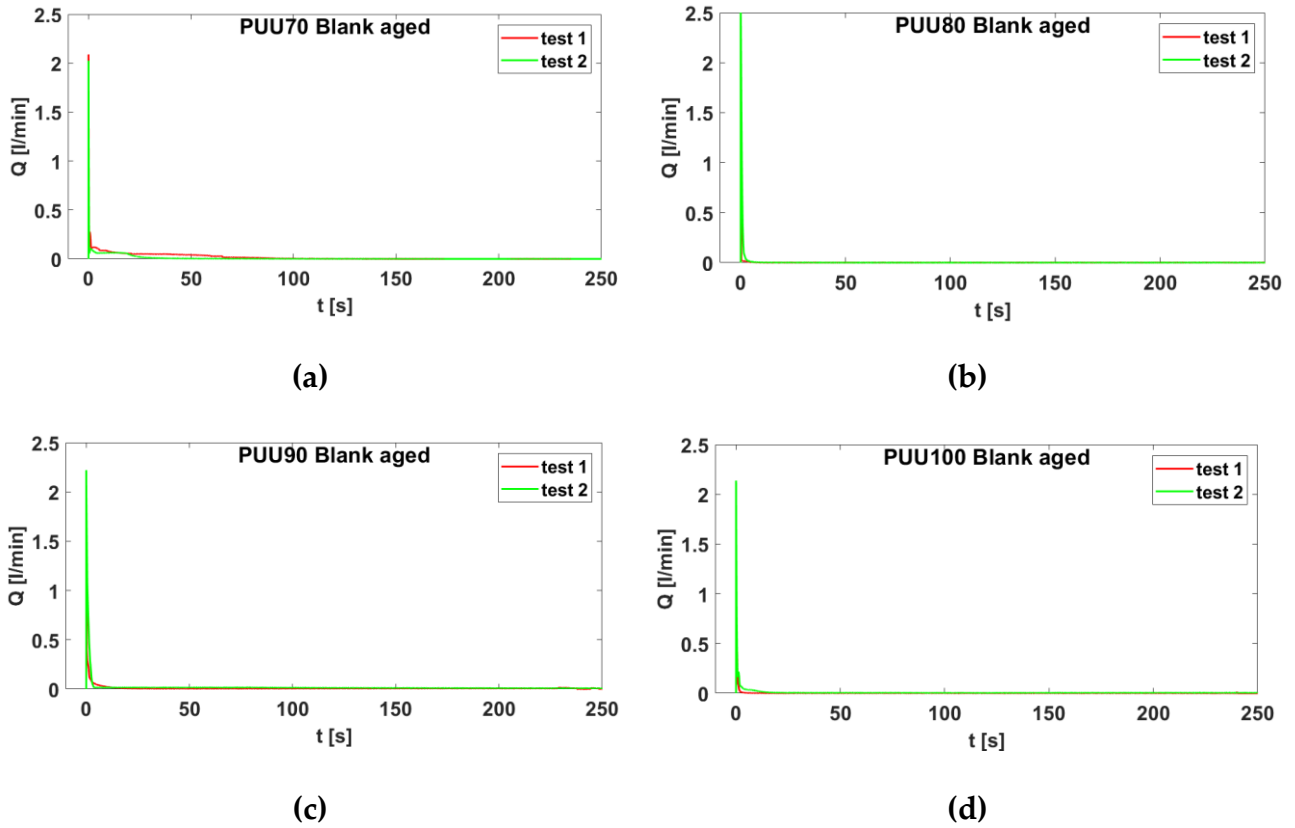


Figure 3.15: Flow rate curves for blank aged PUUs.

Considering Reverlink® tests, they were performed in 250 s since a full recovery was exhibited, there wasn't the necessity to wait for more time as for the other Reverlink® cases. As in the previous case, it performs worse with the respect to PUUs, but there is an improvement comparing with the results obtained immediately after manufacturing. Table 3.13 illustrates the puncture test results, while Figure 3.16 shows the flow rate curve for Reverlink® blank aged.

Table 3.13: Reverlink® blank aged test results.

Test	Q_{max} [l/min]	Q_{min} [l/min]	Δt [s]	V_{leak} [l]
1	3.3458	0.0028	250	0.32660
2	3.5755	0	219.92	0.31611
Mean	3.4607	0.0014	234.96	0.32136

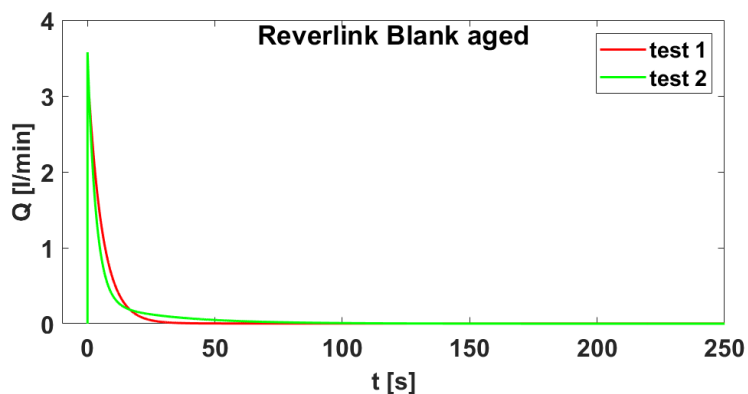


Figure 3.16: Flow rate curve for Reverlink® blank aged.

A comparison between the flow rate curves obtained from the puncture tests performed on blank aged samples is represented in Figure 3.17.

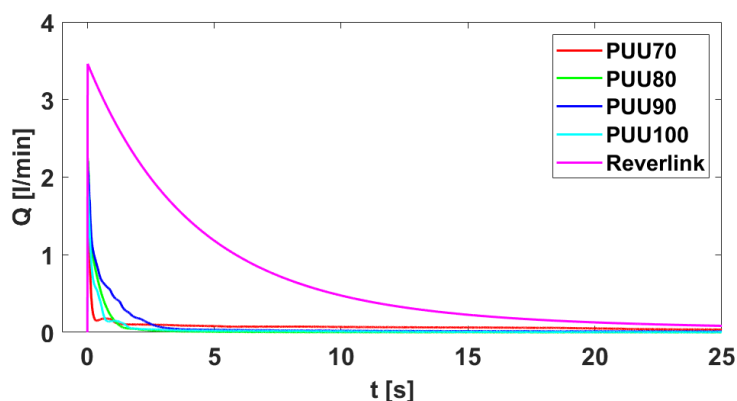


Figure 3.17: Flow rate curves for blank aged comparison.

It can be clearly seen the huge difference between Reverlink® and PUUs, both in terms of maximum flow rate, repair rate and volume lost. Among PUUs, the worst performing one is PUU 90, while the others have a similar behavior.

3.4.3 Irradiated samples

Puncture tests were performed on two sets of irradiated samples. The first set was irradiated by a radiation dose of 100 krad, while the second set by a radiation dose of 500 krad (corresponding to 1000 and 5000 Gy respectively). The thicknesses of the tested samples are reported in Table 3.14.

Table 3.14: Thicknesses of tested irradiated samples.

	PUU 70	PUU 80	PUU 90	PUU 100	Reverlink®
100 krad - Thickness [mm]	2.06	2.21	2.05	2.23	2.67
500 krad - Thickness [mm]	2.02	2.19	2.3	2.15	1.9

3.4.3.1 100 krad irradiation

The puncture tests results for the samples irradiated by a radiation dose of 100 krad are very promising, as all the samples repair the hole created.

Considering PUUs, they repair in an average time lower than 10 seconds with a very small air volume leakage (less than 0.015 l). The maximum value of flow rate exhibited is about 2.26 l/min, by PUU 90, that is still a contained value for the crew safety. In general, all the samples passed the test successfully. From Figure 3.18 to Figure 3.21 the results of the tests are plotted, while Table 3.15 to Table 3.18 collects the self-healing performance parameters for each test, together with the mean value and the standard deviation. All the samples were subjected to a leakage test after repair, which successfully passed as well.

Table 3.15: PUU 70 irradiated by 100 krad dose puncture test results.

Test	Q_{max} [l/min]	Q_{min} [l/min]	Δt [s]	V_{leak} [l]
1	1.9260	0	3.88	0.00290
2	1.7802	0	4.33	0.00288
3	2.2533	0	10.22	0.01017
Mean	1.9865	0	6.14	0.00531
σ	0.2422	0	3.54	0.00420

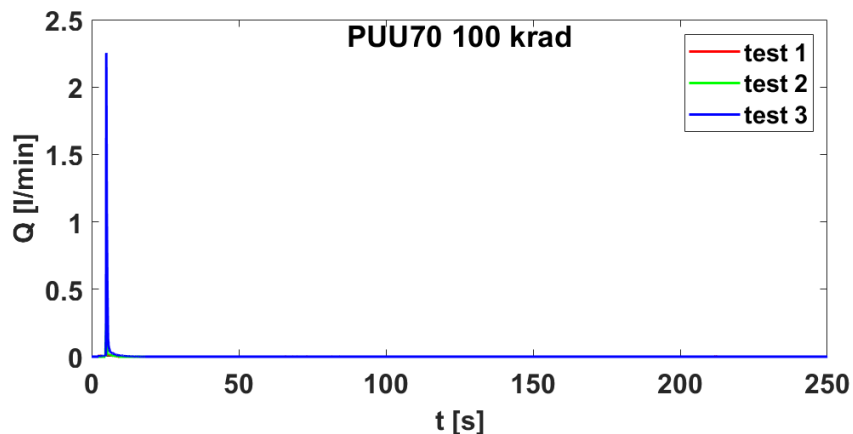


Figure 3.18: Flow rate curves for PUU 70 irradiated by 100 krad dose.

Table 3.16: PUU 80 irradiated by 100 krad dose puncture test results.

Test	Q_{max} [l/min]	Q_{min} [l/min]	Δt [s]	V_{leak} [l]
1	1.5982	0	4.71	0.00244
2	2.2335	0	8.05	0.01041
3	1.7768	0	3.28	0.00393
Mean	1.8762	0	5.34	0.00560
σ	0.3276	0	2.45	0.00424

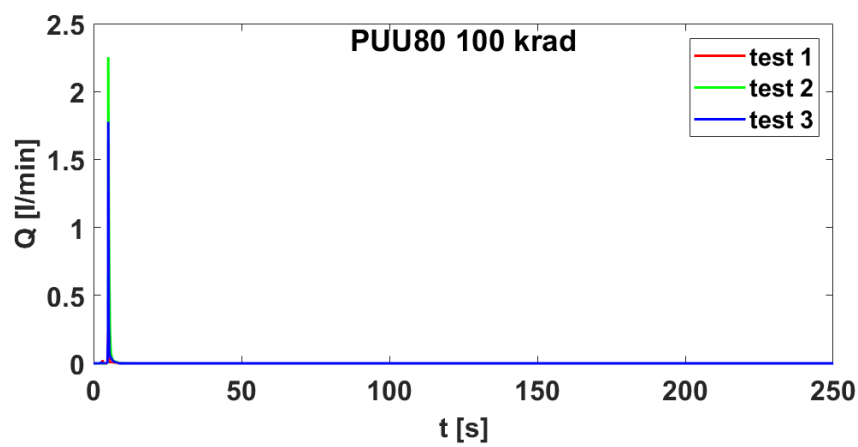


Figure 3.19: Flow rate curves for PUU 80 irradiated by 100 krad dose.

Table 3.17: PUU 90 irradiated by 100 krad dose puncture test results.

Test	Q_{max} [l/min]	Q_{min} [l/min]	Δt [s]	V_{leak} [l]
1	2.1615	0	5.43	0.00809
2	2.2608	0	3.97	0.01296
3	2.2059	0	5.04	0.01450
Mean	2.2094	0	4.81	0.01185
σ	0.0497	0	0.76	0.00334

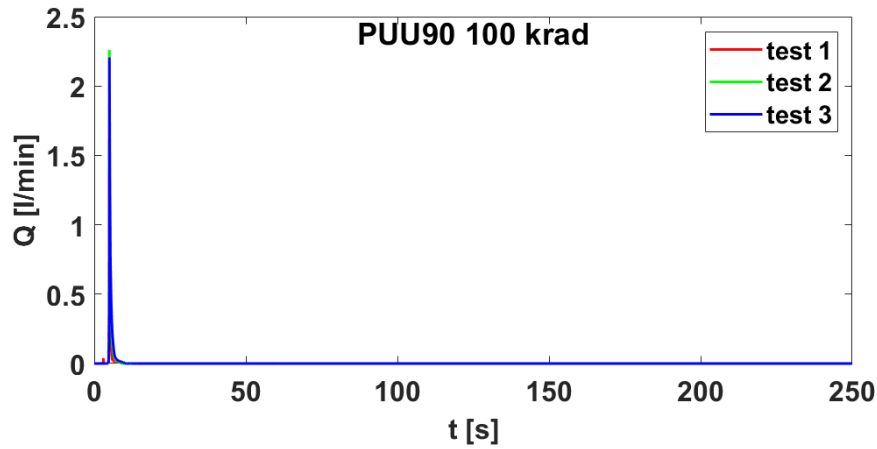


Figure 3.20: Flow rate curves for PUU 90 irradiated by 100 krad dose.

Table 3.18: PUU 100 irradiated by 100 krad dose puncture test results.

Test	Q_{max} [l/min]	Q_{min} [l/min]	Δt [s]	V_{leak} [l]
1	2.1114	0	5.13	0.00676
2	1.8331	0	11.27	0.00882
3	1.7438	0	4.81	0.00234
Mean	1.8961	0	7.07	0.00597
σ	0.1917	0	3.64	0.00331

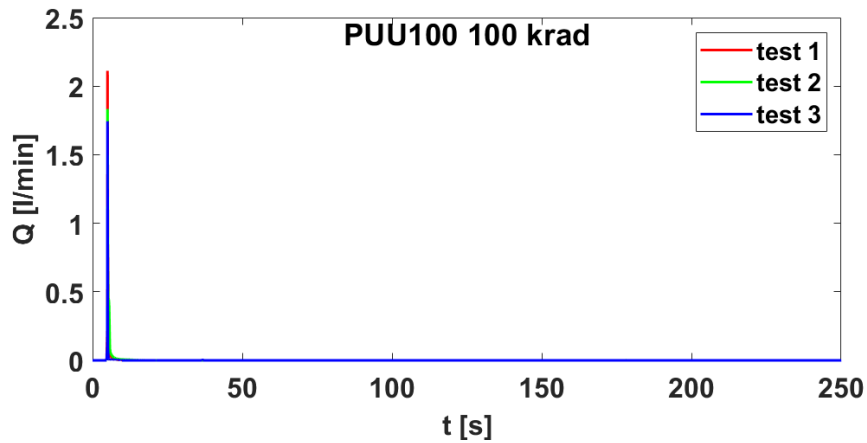


Figure 3.21: Flow rate curves for PUU 100 irradiated by 100 krad dose.

Concerning Reverlink®, Table 3.19 illustrates an average maximum flow rate value Q_{max} of 5.99 l/min, an average time to reach the minimum flow rate value Δt of 101.88 s and an average volume leakage of 0.35 l. Those values are much higher than the ones for PUUs, resulting in a worse self-healing efficiency. Despite this, the polymer completely repairs itself and still has a good self-healing performance for space applications.

As general example, a leakage test performed on Reverlink® sample is shown in Figure 3.23.

Table 3.19: Reverlink® irradiated by 100 krad dose puncture test results.

Test	Q_{max} [l/min]	Q_{min} [l/min]	Δt [s]	V_{leak} [L]
1	3.7210	0	116.72	0.16006
2	10	0	28.73	0.64645
3	4.2496	0	160.19	0.23168
Mean	5.9902	0	101.88	0.34607
σ	3.4826	0	66.9746	0.2626

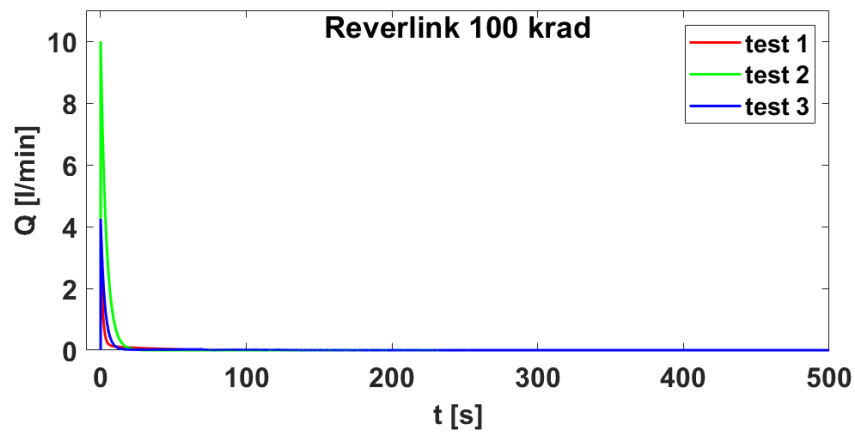


Figure 3.22: Flow rate curves for Reverlink® irradiated by 100 krad dose.

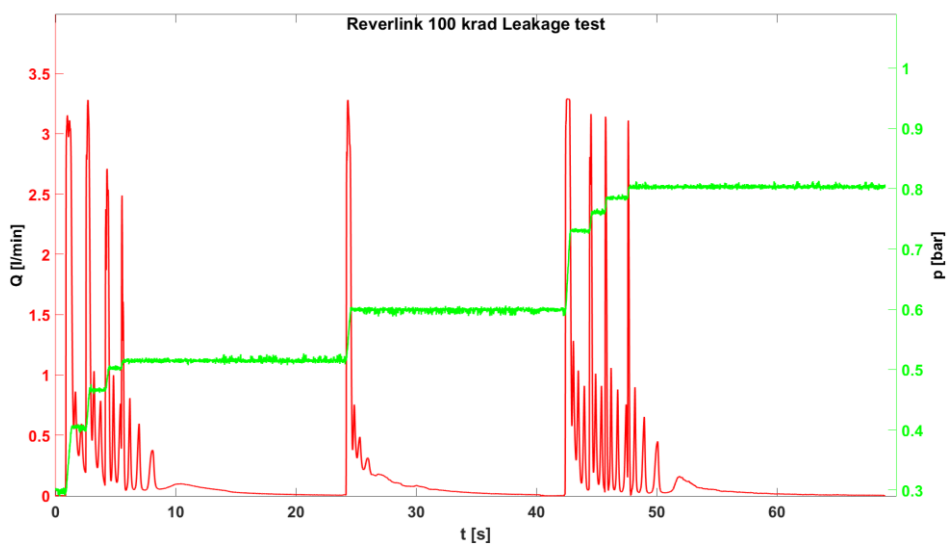


Figure 3.23: Reverlink® irradiated by 100 krad dose leakage test.

In Figure 3.24 (a) and (b) examples of how the samples appear immediately after the test are shown. The test mark on the sample, which may suggest that repair did not actually take place, vanishes after several minutes as the viscoelastic deformation recovers.

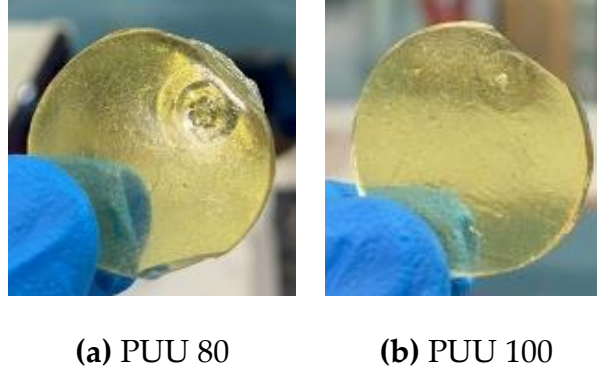


Figure 3.24: PUU 80 and PUU 100 samples immediately after puncture test.

A more schematic comparison between the mean results obtained is illustrated in Table 3.20. As already stressed, perfect healing is reached for all the samples. A big difference between PUUs and Reverlink® can be noticed by looking at the other parameters like the maximum flow rate Q_{max} , that is in the range of 1.87 and 2.2 l/min for PUUs and 5.99 l/min for Reverlink®. This big difference is reflected also considering Δt and V_{leak} . PUU 90 is the poly(urea-urethane) that shows the worst results in terms of maximum flow rate and volume leak.

Table 3.20: Comparison of the mean results obtained for 100 krad irradiation.

Sample	Q_{max} [l/min]	Q_{min} [l/min]	Δt [s]	V_{leak} [L]
PUU 70	1.9865	0	6.14	0.00531
PUU 80	1.8762	0	5.34	0.00560
PUU 90	2.2094	0	4.81	0.01185
PUU 100	1.8961	0	7.07	0.00597
Reverlink®	5.9902	0	101.88	0.34607

Figure 3.25 shows the flow rate curves comparison between the samples. This graphic comparison was done considering only the first 25 s of the tests, in order to better see the previously mentioned differences between Reverlink® and PUUs.

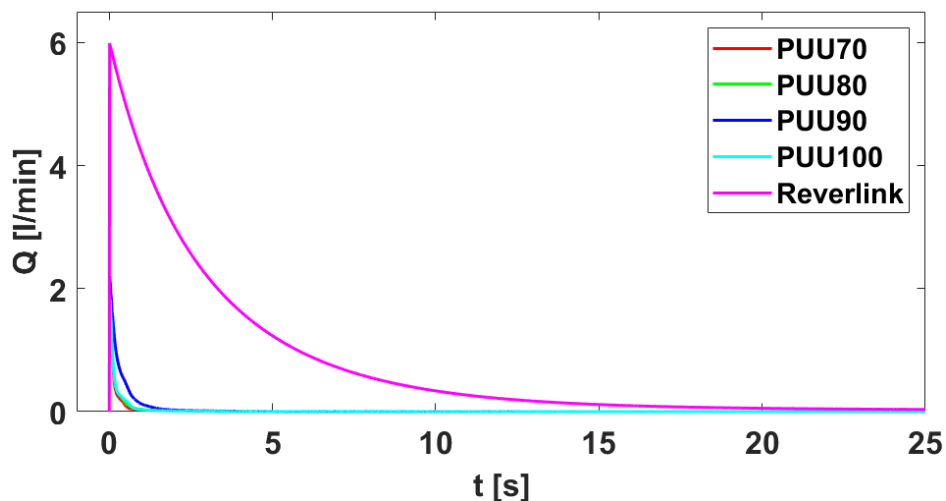


Figure 3.25: Flow rate curves comparison for 100 krad irradiation.

3.4.3.2 500 krad irradiation

Puncture tests performed on samples irradiated by 500 krad dose show slightly worse results compared to those irradiated by 100 krad, in terms of higher mean time Δt to reach the minimum flow rate and higher mean volume leak. PUU 70, PUU 80 and PUU 90 repair the damage inflicted during the test, while PUU 100 and Reverlink® do not repair respectively once and twice during the three tests. Leakage tests were performed only on successful ones.

From Table 3.21 to Table 3.24 the self-healing performance parameters for the PUUs tested are illustrated. Flow rate curves are shown from Figure 3.26 to Figure 3.29.

Table 3.21: PUU 70 irradiated by 500 krad dose puncture test results.

Test	Q_{max} [l/min]	Q_{min} [l/min]	Δt [s]	V_{leak} [L]
1	1.9937	0	6.94	0.00688
2	2.2755	0	15.19	0.01868
3	2.2952	0	81.76	0.01522
Mean	2.1881	0	34.63	0.01359
σ	0.1687	0	41.0237	0.0061

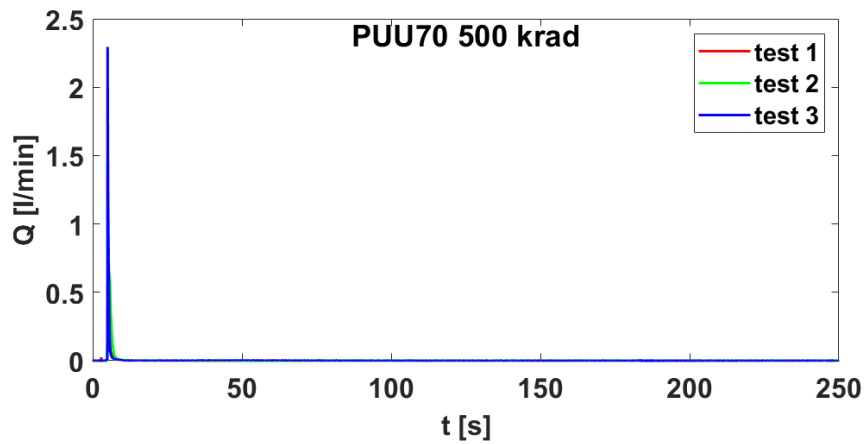


Figure 3.26: Flow rate curves for PUU 70 irradiated by 500 krad dose.

Table 3.22: PUU 80 irradiated by 500 krad dose puncture test results.

Test	Q_{max} [l/min]	Q_{min} [l/min]	Δt [s]	V_{leak} [L]
1	1.6156	0	9.43	0.00428
2	2.1157	0	9.98	0.01002
3	2.1008	0	9.86	0.01361
Mean	1.9441	0	9.76	0.00930
σ	0.2845	0	0.2892	0.0047

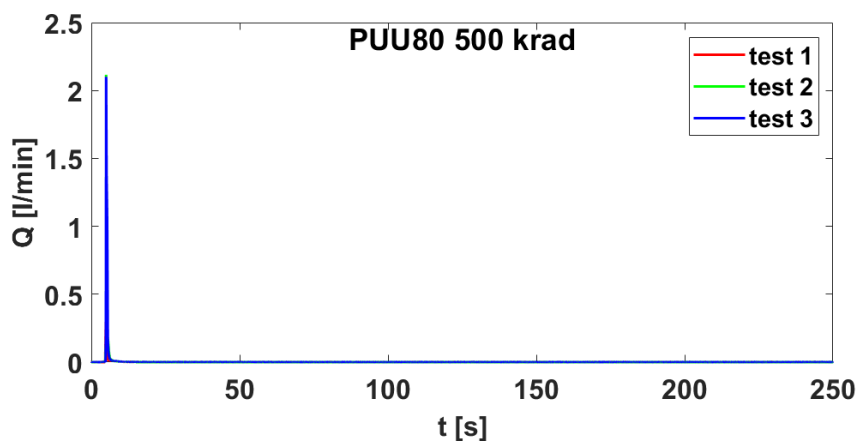


Figure 3.27: Flow rate curves for PUU 80 irradiated by 500 krad dose.

Table 3.23: PUU 90 irradiated by 500 krad dose puncture test results.

Test	Q_{max} [l/min]	Q_{min} [l/min]	Δt [s]	V_{leak} [L]
1	1.8287	0	9.47	0.01143
2	2.2833	0	21.71	0.01694
3	2.3014	0	113.93	0.03517
Mean	2.1378	0	48.37	0.02118
σ	0.2678	0	57.1055	0.0124

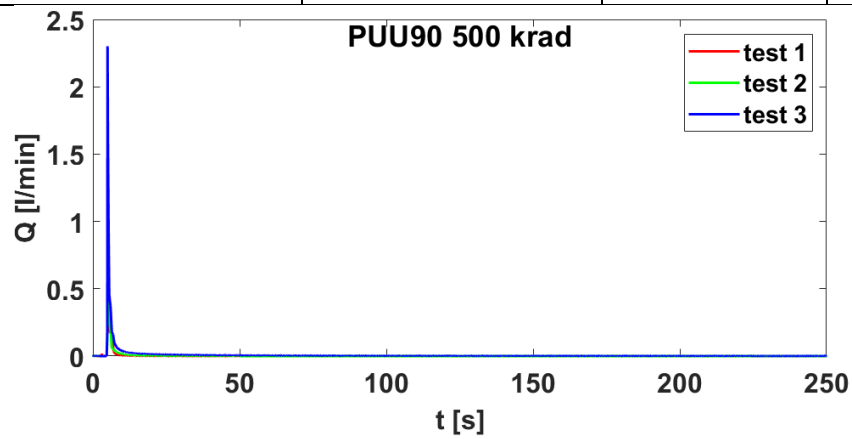


Figure 3.28: Flow rate curves for PUU 90 irradiated by 500 krad dose.

Table 3.24: PUU 100 irradiated by 500 krad dose puncture test results.

Test	Q_{max} [l/min]	Q_{min} [l/min]	Δt [s]	V_{leak} [L]
1	2.0048	0	24.90	0.00698
2	1.8734	0.0174	44.69	0.08184
3	2.0379	0	17.01	0.01514
Mean	1.9720	0.0058	28.87	0.03465
σ	0.0870	0.0100	14.2600	0.0411

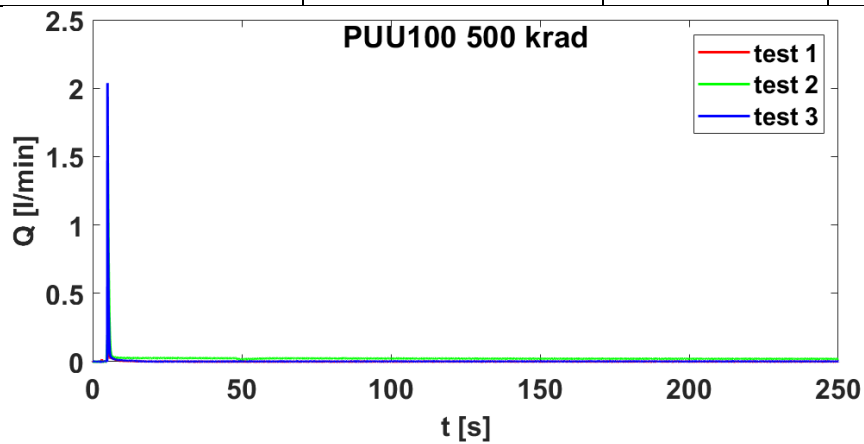


Figure 3.29: Flow rate curves for PUU 100 irradiated by 500 krad dose.

In the case of 500 krad dose as well, Reverlink® is the worst performing polymer among the ones tested, with nearly half a liter of air volume lost in average during the test, together with two failed tests. Table 3.25 illustrates the values of the puncture tests performance parameters for Reverlink®, while the flow rate curve is shown in Figure 3.30.

Table 3.25: Reverlink® irradiated by 500 krad dose puncture test results.

Test	Q_{max} [l/min]	Q_{min} [l/min]	Δt [s]	V_{leak} [l]
1	3.4810	0.0490	648.17	1.0254
2	3.1685	0.1755	649.18	0.9677
3	3.7828	0	59.78	0.2510
Mean	3.4774	0.0748	452.38	0.7480
σ	0.3072	0.0906	334.00	0.4314

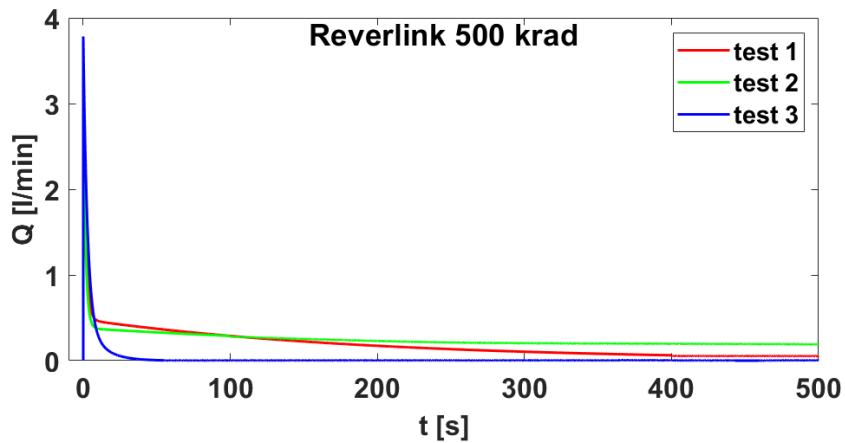


Figure 3.30: Flow rate curves for Reverlink® irradiated by 500 krad dose.

Table 3.26 shows a comparison between the mean results of the puncture tests performed on the samples.

Table 3.26: Comparison of the mean results obtained for 500 krad irradiation.

Sample	Q_{max} [l/min]	Q_{min} [l/min]	Δt [s]	V_{leak} [l]
PUU 70	2.1881	0	34.63	0.01359
PUU 80	1.9441	0	9.76	0.00930
PUU 90	2.1378	0	48.37	0.02118
PUU 100	1.9720	0.0058	28.87	0.03465
Reverlink®	3.4774	0.0748	452.38	0.7480

Figure 3.31 shows a comparison between the flow rate curves of the tested polymers. As in the case of 100 krad, only the first 25 s were considered for the comparison.

Considering PUUs, PUU 80 is the best performing one, with the fastest recovery, lowest maximum flow rate and smallest volume lost. The worst performing one is PUU 100, since it doesn't heal at 100% and for this reason has the biggest amount of volume lost. However, looking at Figure 3.31, again PUU 90 is the slowest one in terms of recovery rate compared to the other PUUs. Again, Reverlink® is visibly the worst performing material among them.

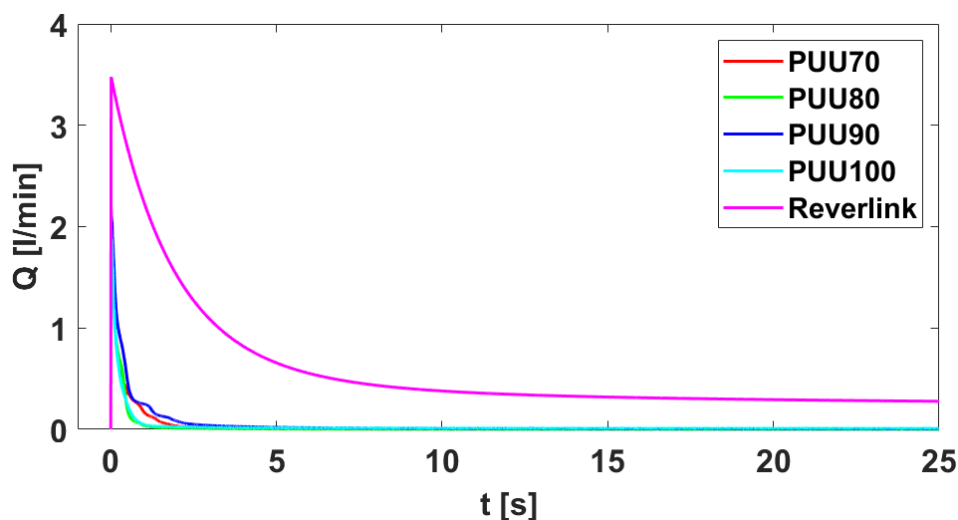


Figure 3.31: Flow rate curves comparison for 500 krad irradiation.

3.4.4 Comparison between blank and irradiated samples

Comparing the results obtained from the puncture tests performed on blanks immediately after the manufacturing and on blanks aged (1 year after the manufacturing), it can be seen a worsening of the self-healing performance for all PUUs. Looking at Table 3.27, an increase of the maximum flow rate is shown, together with a bigger air volume lost and Δt (except for PUU 80). The greatest deterioration is exhibited by PUU 90, with an increase of the Q_{max} by almost 40% and a much bigger volume lost. It should also be noted that the thickness of the blank aged samples is about twice the thickness of the blanks after manufacturing (2 mm for blanks aged, 1 mm for blanks), but despite this the results are worse. Therefore, from test results, it appears that ageing leads to a worsening of self-healing performance for poly(urea)urethane polymers.

The opposite behaviour is shown by Reverlink®, which greatly improves repair efficiency after one year. There is, indeed, a much lower Q_{max} , Δt and V_{leak} , as well as

an almost complete repair, compared to the results exhibited immediately after manufacturing.

Table 3.27: Comparison of the blanks' mean results for each polymer.

Conditioning	Q_{max} [l/min]	Q_{min} [l/min]	Δt [s]	V_{leak} [l]
PUU 70				
Blank	1.8274	0	11.29	0.0128
Blank aged	2.0571	0	104.33	0.0522
PUU 80				
Blank	2.0379	0	14.80	0.0141
Blank aged	2.2541	0	10.95	0.0143
PUU 90				
Blank	1.5885	0	16.79	0.0047
Blank aged	2.2153	0.003	162.48	0.0542
PUU 100				
Blank	1.5960	0	7.51	0.0030
Blank aged	2.0026	0	59.35	0.0196
Reverlink®				
Blank	10.1105	0.1539	488.79	5.6910
Blank aged	3.4610	0.0014	234.96	0.3214

The samples were irradiated shortly after manufacture, but tested only one year later. It is therefore decided to compare the results of the tests performed on the irradiated samples with those performed on the aged blanks. In this way, we assume to evaluate the effects of only the exposure to γ -radiation, neglecting a possible different effect of ageing on the already irradiated samples with respect to blanks.

Table 3.28: Comparison of the mean results in the different configurations for each polymer.

Conditioning	Q_{max} [l/min]	Q_{min} [l/min]	Δt [s]	V_{leak} [l]
PUU 70				
Blank aged	2.0571	0	104.33	0.0522
100 krad	1.9865	0	6.14	0.0053
500 krad	2.1881	0	34.63	0.0136
PUU 80				
Blank aged	2.2541	0	10.95	0.0143
100 krad	1.8762	0	5.34	0.0056
500 krad	1.9441	0	9.76	0.0093
PUU 90				
Blank aged	2.2153	0.003	162.48	0.0542
100 krad	2.2094	0	4.81	0.0119
500 krad	2.1378	0	48.37	0.0212

PUU 100				
Blank aged	2.0026	0	59.35	0.0196
100 krad	1.8961	0	7.07	0.0060
500 krad	1.9720	0.0058	28.87	0.0347
Reverlink®				
Blank aged	3.4610	0.0014	234.96	0.3214
100 krad	5.9902	0	101.88	0.3461
500 krad	3.4774	0.0748	452.38	0.7480

From the results illustrated in Table 3.28, there seems to be that irradiation has a positive effect on the self-healing performance of PUUs with the respect to blank aged. Generally, there is a slight decrease in Q_{max} and a large reduction in volume lost during the test, as well as a faster recovery.

A comparison between the flow rate curves of the PUUs aged blanks and irradiated is illustrated graphically in figures from Figure 3.32 to Figure 3.35.

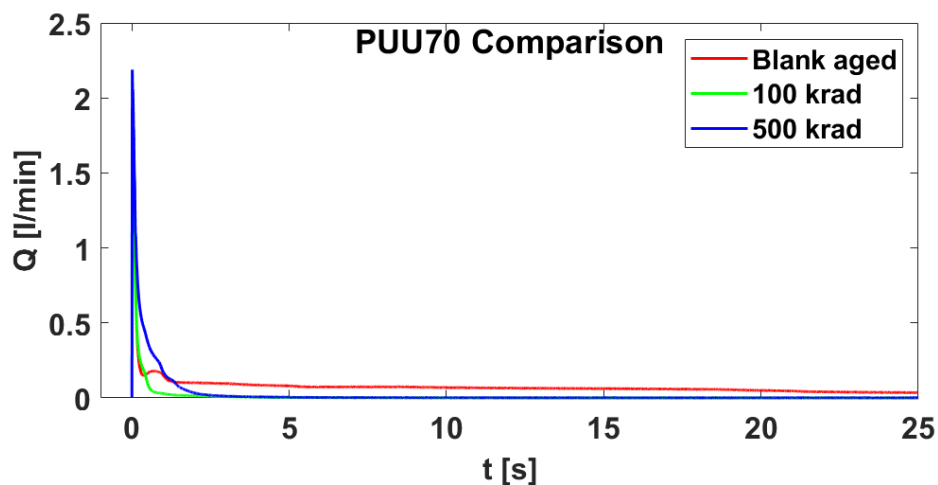


Figure 3.32: PUU 70 flow rate comparison between blank aged and irradiated.

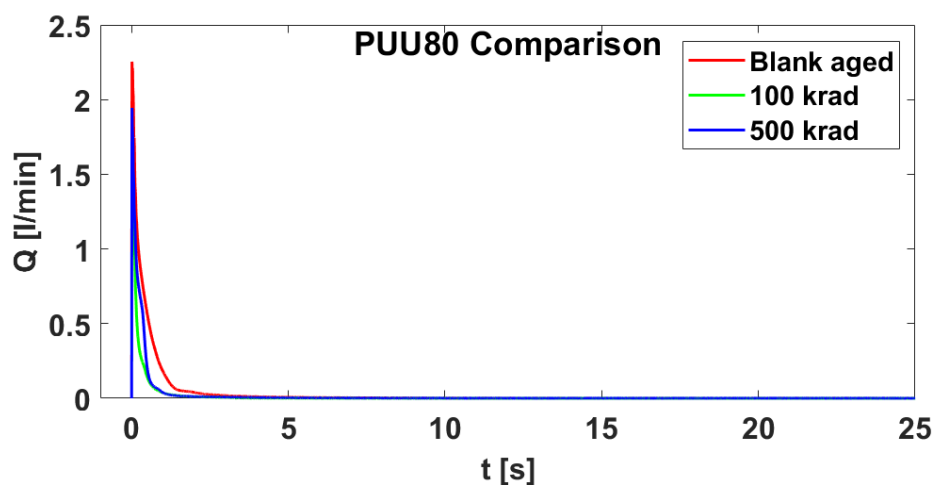


Figure 3.33: PUU 80 flow rate comparison between blank aged and irradiated.

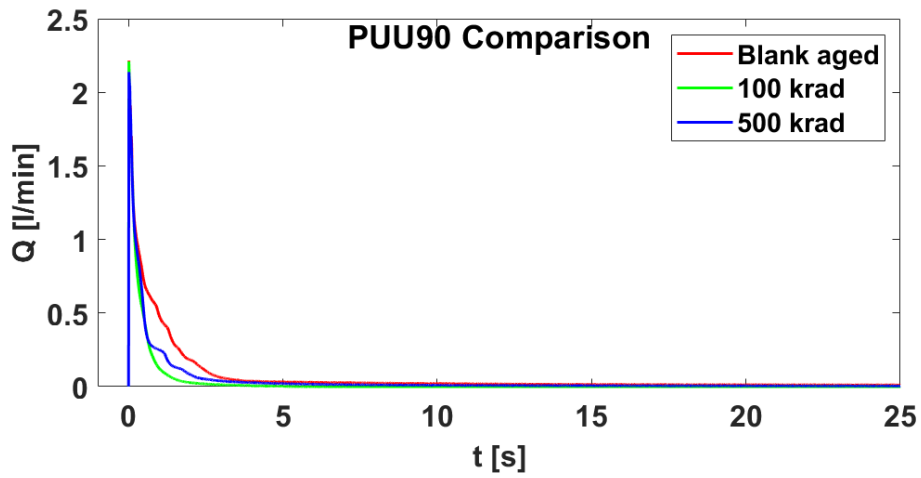


Figure 3.34: PUU 90 flow rate comparison between blank aged and irradiated.

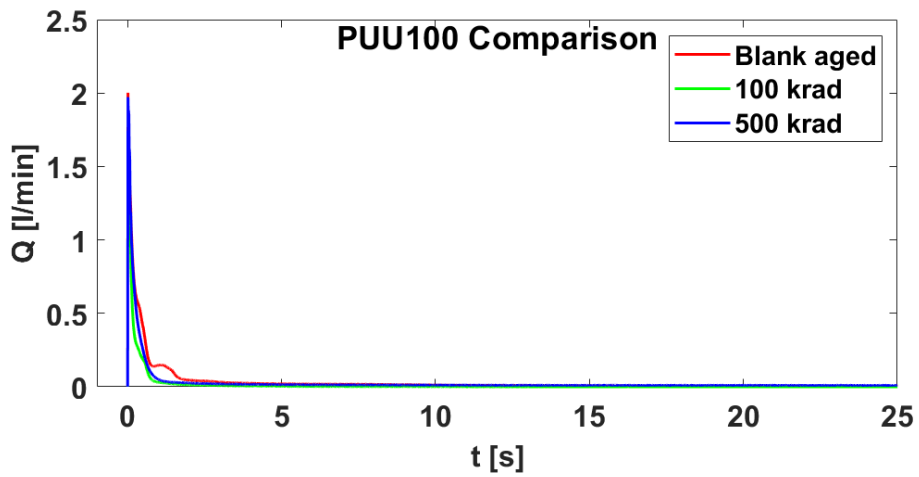


Figure 3.35: PUU 100 flow rate comparison between blank aged and irradiated.

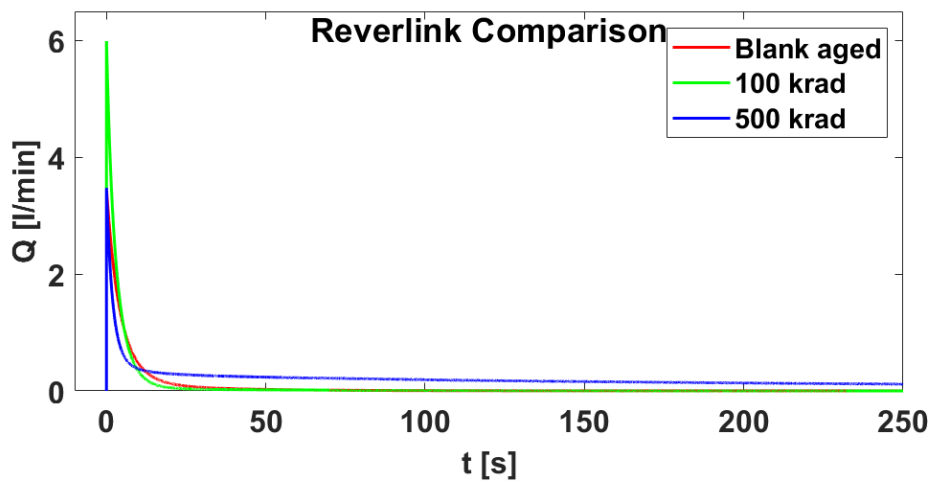


Figure 3.36: Reverlink® flow rate comparison between blank aged and irradiated.

Regarding Reverlink®, there is an opposite behavior with the respect to PUUs. Indeed, comparing the results for blank aged and irradiated samples, on average there is an overall deterioration, with the worst self-healing behavior belonged to the 500 krad samples.

4. Modeling

In this chapter, a viscoelastic model for the tested polymers is presented, starting with a schematization of the puncture test phases. The model is useful for the analysis of the polymers' viscoelastic properties and the assessment of the changes due to ageing and irradiation, relating them to the main characteristic parameters of self-healing performance (Figure 4.1). The assessment is based on the results of the puncture test.

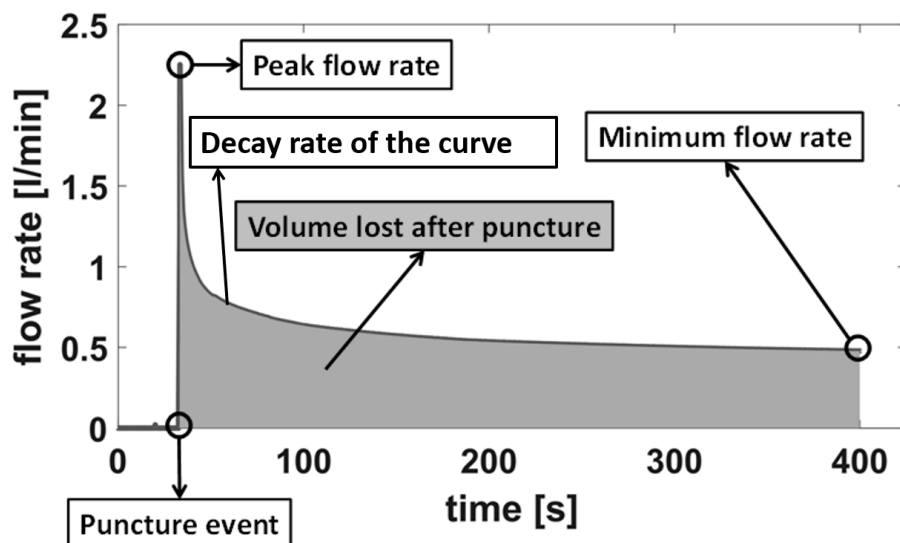


Figure 4.1: Characteristic parameters of the self-healing performance.

4.1 Puncture test model

The flow rate curve over time, obtained from puncture test data, can be associated with the strain decay curve over time due to the release of a stress applied to the polymer, known as strain recovery behavior (Figure 4.2).

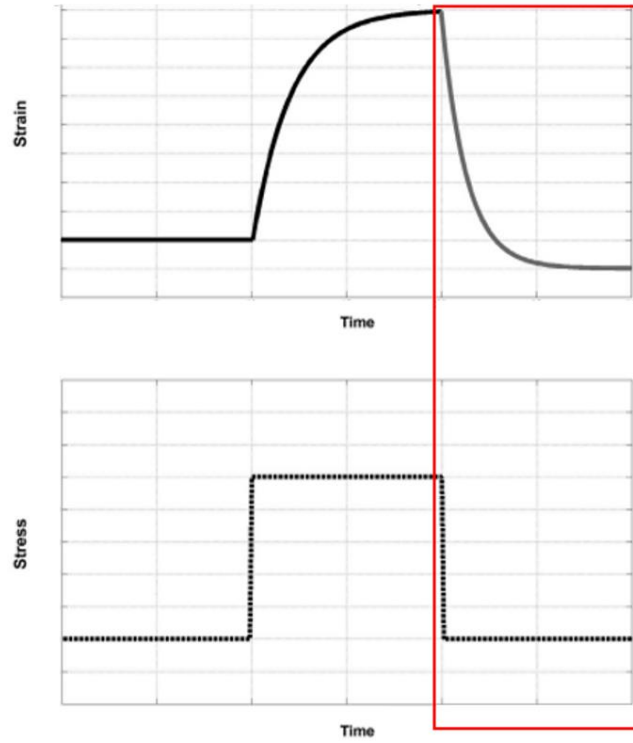


Figure 4.2: Strain recovery for viscoelastic materials example [78].

There is therefore the necessity to correlate the flow rate to the deformation experienced by the sample during the puncture test. To do this, we start by considering the test as divided into four different steps and how the radius of the hole created changes.

In the first step the puncture probe is not in contact with the sample, the radius is null. This step ends at the puncture event. In the second step the puncturing needle penetrates the sample, the perforation of the sample takes place, and a linear increase of the radius is assumed from $r(0) = 0 \text{ mm}$ to the value of the puncture probe radius $r_{probe} = 1 \text{ mm}$. The hole reaches this maximum size as soon as the needle's sharp end has completely penetrated the material. For this reason, the lifetime t_1 of the second step is equivalent to the time required for the puncheon to travel a distance equal to the sharp edge's height $h_p = 3.53 \text{ mm}$, considering that the vertical velocity imposed on the puncheon comes from the indications given by the ASTM F1342/F1342M-05 standard [76]:

$$v_p = 50.8 \frac{\text{cm}}{\text{min}} \approx 8.46 \frac{\text{mm}}{\text{s}} \quad (4.1)$$

$$t_1 = \frac{h_p}{v_p} \approx 0.42 \text{ s} \quad (4.2)$$

so, the radius increase velocity is:

$$v_r = \frac{r_{probe}}{t_1} \approx 2.38 \frac{mm}{s} \quad (4.3)$$

The third step represents the phase in which the needle has completely penetrated the sample, the radius of the hole is forced to remain at a value equal to r_{probe} . In this step a partial stress relaxation occurs. An acceptable estimate of the lifetime of this step is:

$$t_2 = 0.5 \text{ s}$$

The fourth and final step starts when removing the puncture probe from the sample, in correspondence to the top of the sharp end. During this step the hole's radius decreases, reaching 0 mm in case of total repair and thus sealing the hole created.

To correlate the flow rate with the radius of the hole Eq. 4.4 is used [79]:

$$Q(t) = \frac{\dot{m}(t)}{\rho_a} \quad (4.4)$$

$\rho_a = 1.225 \frac{kg}{m^3}$ is the air density e $\dot{m}(t)$ represents the mass flow rate through the hole:

$$\dot{m}(t) = C_d \cdot A_h(t) \cdot \psi \cdot p_0 \cdot \sqrt{\frac{2}{R_a \cdot T_0}} \quad (4.5)$$

C_d is the discharge coefficient, equal to 0.6 (typical value for small orifices), p_0 is the absolute pressure inside the cylindrical vessel, obtained as the sum between the atmospheric pressure and the applied pressure during the test, $p_0 = 0.131325 \text{ MPa}$, $T_0 = 298.15 \text{ K}$ is the absolute temperature and $R_a = 287 \frac{J}{kg \cdot K}$ is the gas constant of air. $A_h(t)$ is the area of the hole through which the air flows, in mm^2 , assumed to be always circular during time:

$$A_h(t) = \pi \cdot r^2(t) \quad (4.6)$$

It varies in time since it depends on the hole radius $r(t)$. ψ is the pressure dependent outflow function, defined as:

$$\psi = \sqrt{\frac{\gamma}{\gamma - 1} \cdot \left[\left(\frac{p_a}{p_0} \right)^{\frac{2}{\gamma}} - \left(\frac{p_a}{p_0} \right)^{\frac{\gamma+1}{\gamma}} \right]} \quad (4.7)$$

$\gamma = 1.4$ is the specific heat ratio of air, $p_a = 0.101325$ is the atmospheric pressure.

All the parameters of the equation are constant apart from the area of the hole, that changes according to the changing in time of the radius during the puncture test steps. Considering the case in which the radius is maximum and equal to $r_{probe} = 1 \text{ mm}$, the computed $Q_{r_{probe}} = 40 \frac{l}{min}$.

We can notice that this value is far greater than the maximum flow rate value shown by the self-healing polymers during the tests, which varies between 1.5 and $10 \frac{l}{min}$. This difference is related to the fact that the radius of the hole related to the maximum flow rate value is not equivalent to r_{probe} , but to a lower r_0 value. The reason for this is that as soon as the puncture probe exits the sample, an instantaneous elastic recovery of the strain occurs, and so the radius instantaneously decreases from r_{probe} to r_0 . Consequently, the maximum flow rate corresponds to a hole of radius r_0 , which then decreases according to the viscoelastic recovery in time. Figure 4.3 shows a scheme of the radius trend during the four steps of the puncture test.

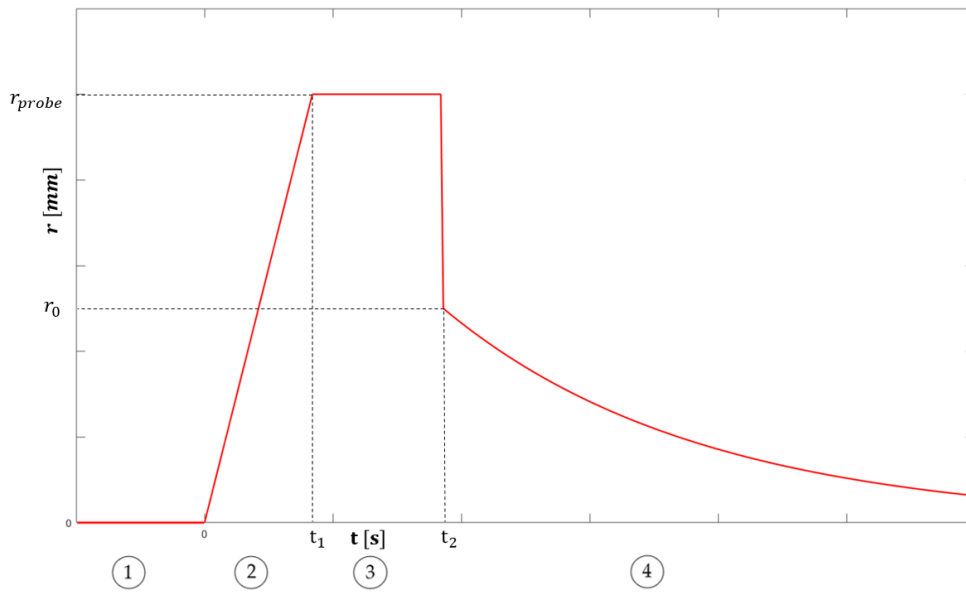


Figure 4.3: Scheme of the radius trend during the puncture test.

The numbers in circles at the bottom represent the four steps into which the puncture test was schematized.

To obtain the strain $\varepsilon(t)$, we approximate our sample as a two-dimensional disk, thus neglecting the influence of thickness, of radius $r_{sample} = 10 \text{ mm}$. We assume for simplicity that the puncture takes place perfectly at the center of the sample (Figure 4.4).

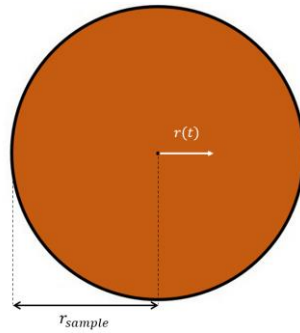


Figure 4.4: Approximation of the polymer sample as a 2D disk.

The strain is, for the sake of simplicity, considered positive:

$$\varepsilon(t) = \frac{r(t)}{r_{sample}} \quad (4.8)$$

the maximum strain value is that corresponding to the radius of the puncture probe, ε_{probe} . Following elastic recovery, the strain equals ε_0 .

$$\varepsilon_{probe} = \frac{r_{probe}}{r_{sample}} \quad (4.9)$$

$$\varepsilon_0 = \frac{r_0}{r_{sample}} \quad (4.10)$$

Consequently, the maximum flow rate value shown by polymers in puncture tests will correspond to a strain value of ε_0 .

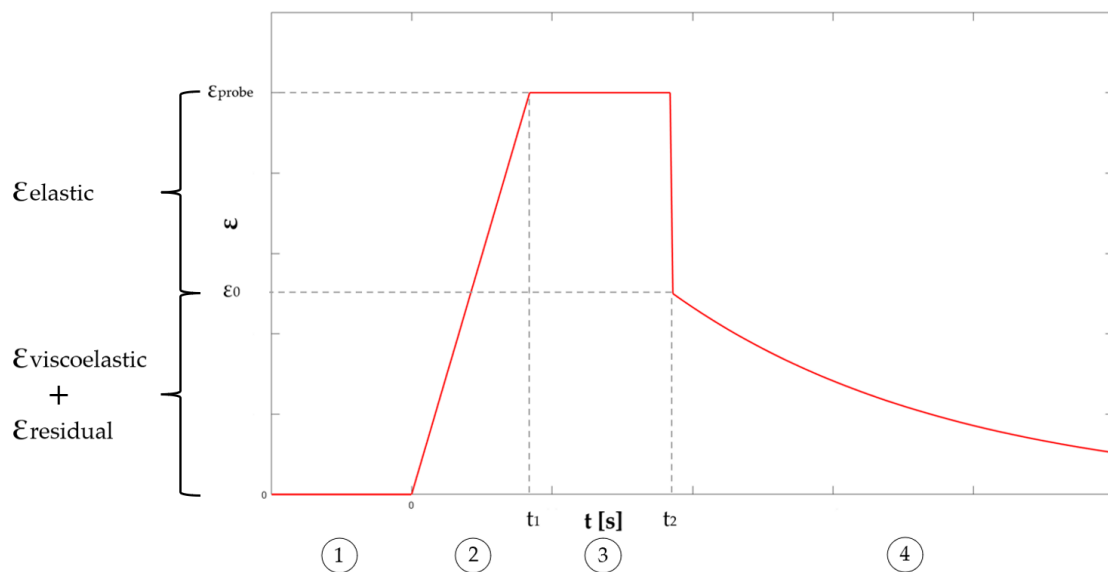


Figure 4.5: Scheme of the strain trend during the puncture test.

As can be schematically seen in Figure 4.5, the elastic deformation $\varepsilon_{elastic}$ is equal to the difference between ε_{probe} and ε_0 , while the viscoelastic deformation $\varepsilon_{viscoelastic}$ is equal to ε_0 if the polymer is completely repaired, otherwise it is less than ε_0 by an amount equivalent to the residual deformation $\varepsilon_{residual}$.

For our purposes, we are only interested in the fourth step.

4.2 Viscoelastic model

A three-element model was chosen as viscoelastic model to represent the polymers tested, namely the Zener model in the Kelvin-Voigt representation (Figure 4.6).

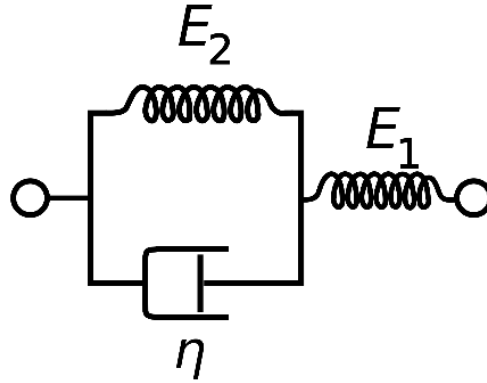


Figure 4.6: Zener model in Kelvin-Voigt representation [80].

The spring with elastic modulus E_1 will model the instantaneous elastic deformation $\varepsilon_{elastic}$, while the spring with elastic modulus E_2 in parallel with the dashpot of viscosity η , (also called Kelvin arm, since it is equivalent to the Kelvin-Voigt model), the viscoelastic deformation $\varepsilon_{viscoelastic}$. The constitutive equation of the model is:

$$\sigma + \frac{\eta}{E_1 + E_2} \cdot \dot{\sigma} = \frac{E_1 \cdot E_2}{E_1 + E_2} \cdot \varepsilon + \frac{E_1 \cdot \eta}{E_1 + E_2} \cdot \dot{\varepsilon} \quad (4.11)$$

To find the strain deformation trend over time, the constitutive equation must be coupled with the boundary conditions of puncture test:

$$\left\{ \begin{array}{l} t > 0 \quad \sigma(t) = 0 \end{array} \right. \quad (4.12)$$

$$\left\{ \begin{array}{l} t = 0 \quad \varepsilon(0) = \varepsilon_0 \end{array} \right. \quad (4.13)$$

Where, for the sake of simplicity, the initial instant of the fourth step coincides with $t = 0$. Considering the first condition (4.12), Eq 4.11 becomes:

$$0 = \frac{E_1 \cdot E_2}{E_1 + E_2} \cdot \varepsilon + \frac{E_1 \cdot \eta}{E_1 + E_2} \cdot \dot{\varepsilon} \quad (4.14)$$

Simplifying:

$$0 = E_2 \cdot \varepsilon + \eta \cdot \dot{\varepsilon} \quad (4.14)$$

This equation is equivalent to the one we would have obtained by considering a zero stress in the Kelvin-Voigt model. For this reason, we start with an initial deformation $\varepsilon(0) = \varepsilon_0$ (4.13), thus obtaining, through the result of the differential equation, the trend of the viscoelastic deformation over time. In a second moment we will add the elastic deformation, represented by the spring with modulus E_1 .

The result of the differential equation (Eq. 4.11), given the two boundary conditions (4.12, 4.13), is:

$$\varepsilon(t) = \varepsilon_0 \cdot \exp\left(-\frac{E_2 \cdot t}{\eta}\right) = \varepsilon_0 \cdot \exp\left(-\frac{t}{\tau}\right) \quad (4.15)$$

Where τ is the relaxation time:

$$\tau = \frac{\eta}{E_2} \quad (4.16)$$

4.3 Fitting

Through the Matlab software and by means of Eq. 4.4 and Eq. 4.8, the hole's strain trend during time was computed for the tested polymers from the flow rate data. For each polymer, irradiated and non-irradiated, the averaged strain values from the tests performed on each sample were computed. Those values were fitted with Eq. 4.15 through the Matlab Fitting Tool, having τ as the only variable parameter. The constraints set for the τ value are:

$$10^5 < \tau < 10 \quad s$$

derived from the constraints considered for E_2 and η [81,82]:

$$10^5 < E_2 < 10^9 \quad MPa$$

$$10^4 < \eta < 10^8 \quad MPa \cdot s$$

Given these conditions, the software returns the value of τ related to the best fitting. Figure 4.7 to Figure 4.11 show some fittings for the tested polymers.

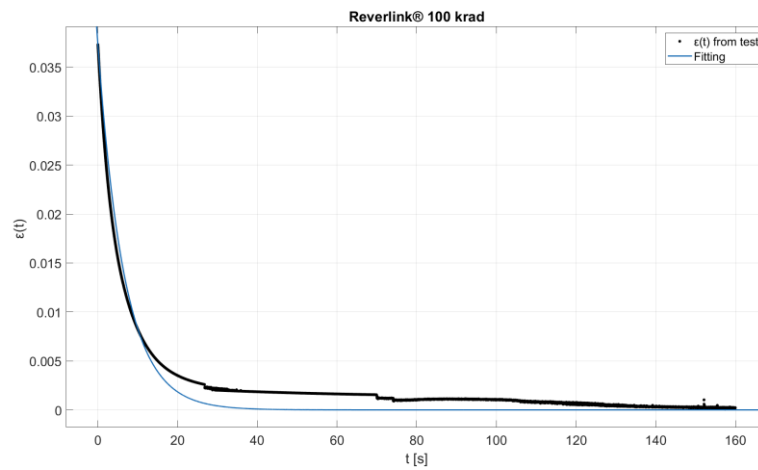


Figure 4.7: Fitting for Reverlink® irradiated by 100 krad.

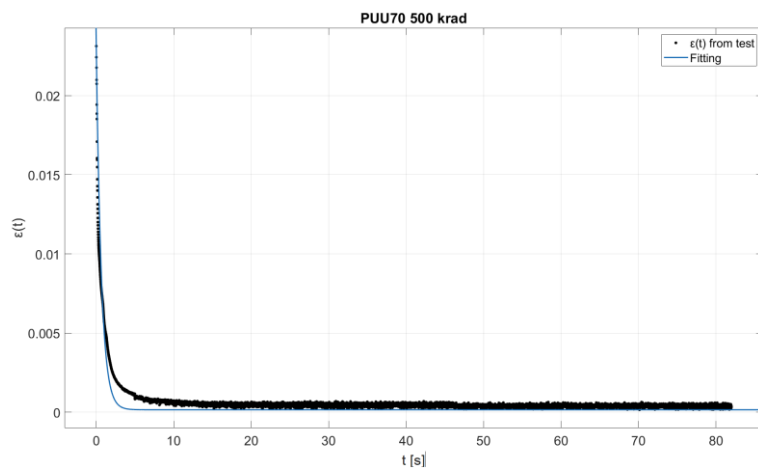


Figure 4.8: Fitting for PUU 70 irradiated by 500 krad.

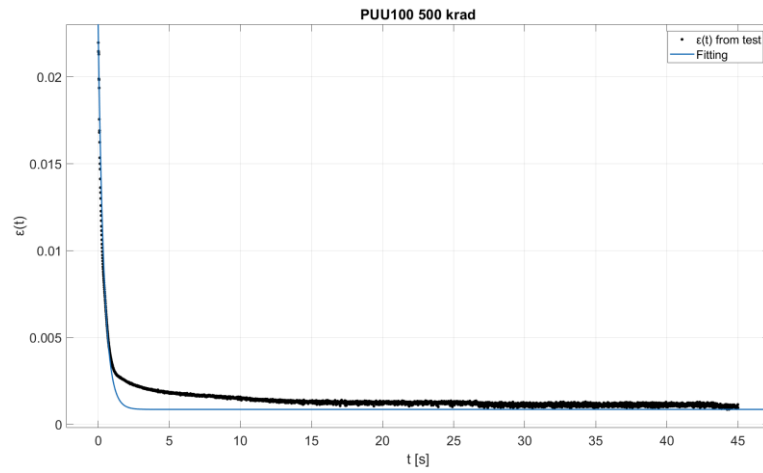


Figure 4.9: Fitting for PUU 100 irradiated by 500 krad.

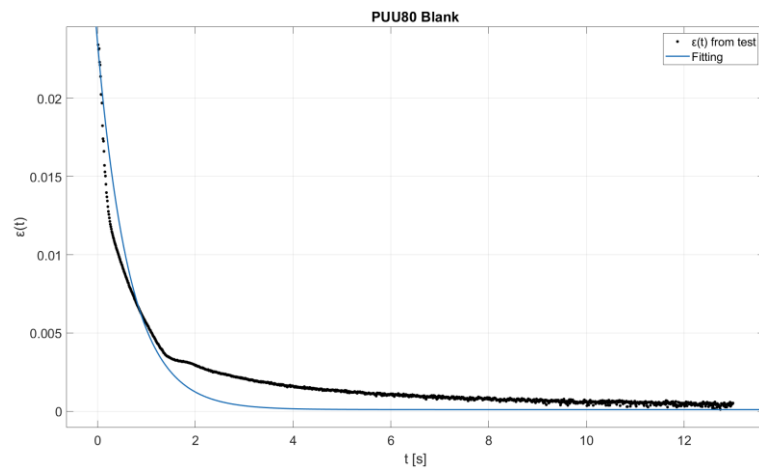


Figure 4.10: Fitting for PUU 80 Blank (aged).

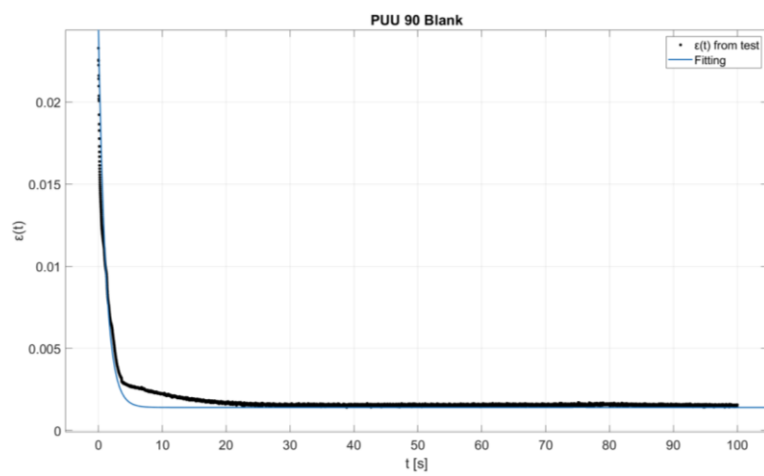


Figure 4.11: Fitting for PUU 90 Blank (aged).

For polymers that did not repair, the $\varepsilon_{residual}$ was added to the fitting expression.

$$\varepsilon(t) = \varepsilon_0 \cdot \exp\left(-\frac{t}{\tau}\right) + \varepsilon_{residual} \quad (4.17)$$

Let us initially assume a value of η equal to $10^7 MPa \cdot s$ for all polymers. The value of E_2 is obtained as:

$$E_2 = \tau \cdot \eta \quad (4.18)$$

To determine E_1 instead, we know that for the Zener model in Kelvin-Voigt representation the stress on the single spring σ_s and on the Kelvin arm σ_k are equivalent to the total stress acting on the system.

$$\sigma_{tot} = \sigma_k = \sigma_s \quad (4.19)$$

Which, the instant before the fourth step (when the stress is still different from 0):

$$\sigma_s = E_1 \cdot \varepsilon_{elastic} \quad (4.20)$$

$$\sigma_k = E_2 \cdot \varepsilon_{viscoelastic} \quad (4.21)$$

For the evaluation of σ_k we neglected the stress value in the dashpot, assuming stress relaxation during the third phase of the test where the strain is constant. E_1 :

$$E_1 = E_2 \cdot \frac{\varepsilon_{viscoelastic}}{\varepsilon_{elastic}} \quad (4.22)$$

The provisional values at this early stage of E_1 , E_2 and η , together with the τ value of the best fit, are presented in Table 4.1.

Table 4.1: Provisional parameters of the viscoelastic model.

Conditioning	E_2 [MPa]	E_1 [MPa]	η [MPa · s]	τ [s ⁻¹]
PUU 70				
Blank aged	12.76	3.69	10	0.783
100 krad	38.51	10.80	10	0.260
500 krad	14.65	4.40	10	0.683
PUU 80				
Blank aged	14.80	4.52	10	0.676
100 krad	29.33	7.99	10	0.341
500 krad	21.99	6.13	10	0.455
PUU 90				
Blank aged	8.07	2.45	10	1.24
100 krad	14.30	4.34	10	0.699
500 krad	9.46	2.80	10	1.057
PUU 100				
Blank aged	13.75	3.90	10	0.727
100 krad	28.11	7.70	10	0.356
500 krad	25.70	7.25	10	0.389
Reverlink®				
Blank aged	1.00	0.41	10	10
100 krad	1.50	0.89	10	6.650
500 krad	1.77	0.73	10	5.640

Another condition is needed to achieve η . To get that, let's consider the second and third steps of the puncture test. As can be seen from Figure 4.5, the second step is characterized by a linear increase in strain over time, with slope:

$$R = \frac{\varepsilon_0}{t_1} = 0.238 \text{ s}^{-1} \quad (4.23)$$

By entering the boundary conditions:

$$\begin{cases} t < 0 & \varepsilon(t) = 0 \\ t > 0 & \varepsilon(t) = R \cdot t \end{cases} \quad (4.24)$$

$$(4.25)$$

The constitutive equation of the Zener model (Eq. 4.11) is written as:

$$\dot{\sigma} = E_1 \cdot R + \frac{E_1 \cdot R}{\tau} \cdot t - \frac{E_1 + E_2}{\tau \cdot E_2} \cdot \sigma \quad (4.26)$$

The third step is characterized by a constant value of strain equal to ε_0 . To achieve this, a linear decrease in strain with a constant slope equal to $-R$ from $t = t_1$ is added (Figure 4.12).

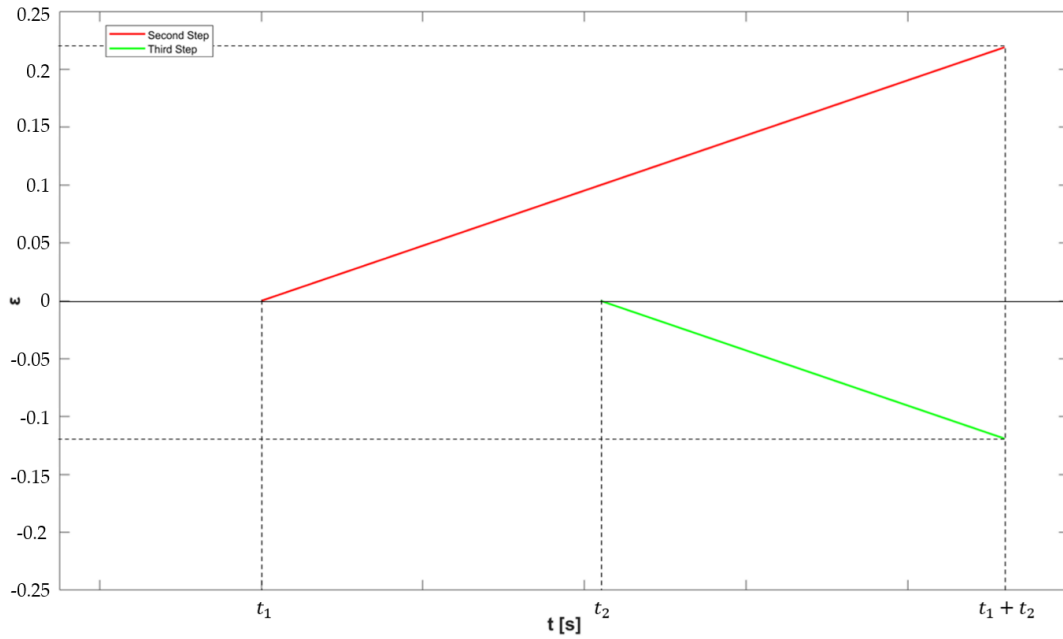


Figure 4.12: Superposition effects for second and third step of the puncture test.

The result of the differential constitutive equation of this third step is the same as the second step, Eq. 4.24, with the difference that the R value has a negative sign.

Once obtained the differential equation for the stress value of the second and third step of the puncture test, by considering the previously calculated values of E_1 and E_2 , we obtain the stress trend over time (Figure 4.13).

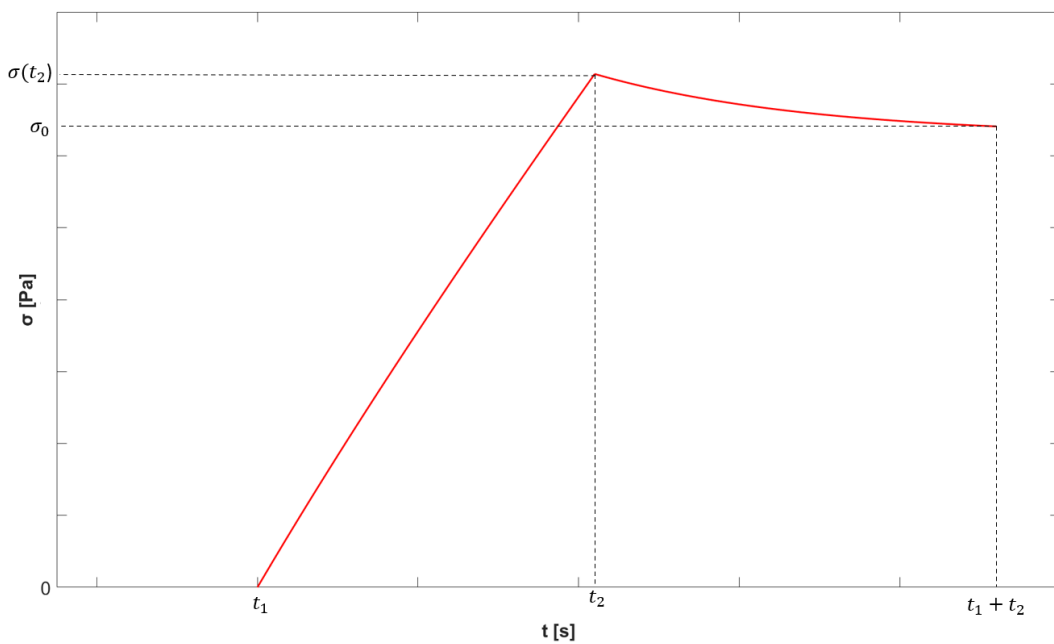


Figure 4.13: Stress curve for second and third step of puncture test.

The stress value at the end of the third step σ_0 , i.e. at time $t = t_1 + t_2$, is equivalent to the stress value on the polymer at the initial instant of the fourth step. Consequently:

$$\sigma_0 = E_1 \cdot \varepsilon_{elastic} = E_2 \cdot \varepsilon_{viscoelastic} \quad (4.27)$$

$$E_1 = \frac{\sigma_0}{\varepsilon_{elastica}} \quad (4.28)$$

$$E_2 = \frac{\sigma_0}{\varepsilon_{viscoelastic}} \quad (4.29)$$

These represent the boundary conditions useful to find a value of η different from the one initially assumed. Thus, the new values of E_1 , E_2 and η are calculated using the τ value resulting from the fitting.

$$\eta = \frac{E_2}{\tau} \quad (4.30)$$

It is important to stress that the parameters E_1 , E_2 and η thus obtained are not the actual parameters of the polymers, but simply parameters resulting from the representative model considered. They are only used to compare the viscoelastic properties of the polymers with each other and assess the changes due to ageing and irradiation.

4.4 Results

Table 4.2 shows the results in terms of elastic, viscoelastic and residual strain resulting from the viscoelastic model introduced in 4.2, together with elastic and viscoelastic deformation percentage. Based on how the viscoelastic model was set up, it is clear that the value of ε_0 is directly related to the value of Q_{max} for the polymers considered (Table 3.28), thus respecting the same changes due to irradiation. On the other hand, the value of $\varepsilon_{residual}$ is directly linked to the minimum flow rate value Q_{min} .

Since:

$$\varepsilon_{probe} = \varepsilon_0 + \varepsilon_{residual} \quad (4.31)$$

$$\varepsilon_0 = \varepsilon_{viscoelastic} + \varepsilon_{residual} \quad (4.32)$$

Consequently, an increase in elastic deformation due to irradiation will correspond to a decrease in viscoelastic deformation and vice versa.

Table 4.2: Strain parameters results from the viscoelastic model.

Conditioning	ϵ_0	$\epsilon_{elastic}$	$\epsilon_{viscoelastic}$	$\epsilon_{residual}$	Elastic deformation %	Viscoelastic deformation %
PUU 70						
Blank aged	0.0224	0.0776	0.0224	0	77.56	22.44
100 krad	0.0219	0.0781	0.0219	0	78.09	21.91
500 krad	0.0231	0.0769	0.0231	0	76.87	23.13
PUU 80						
Blank aged	0.0234	0.0766	0.0234	0	76.60	23.40
100 krad	0.0214	0.0786	0.0214	0	78.63	21.37
500 krad	0.0218	0.0782	0.0218	0	78.23	21.77
PUU 90						
Blank aged	0.0233	0.0767	0.0223	0.001	76.72	22.27
100 krad	0.0233	0.0767	0.0233	0	76.75	23.25
500 krad	0.0228	0.0772	0.0228	0	77.16	22.84
PUU 100						
Blank aged	0.0221	0.0779	0.02175	0.00035	77.88	21.77
100 krad	0.0215	0.0785	0.0215	0	78.48	21.52
500 krad	0.022	0.078	0.021	0.001	78.04	20.93
Reverlink®						
Blank aged	0.0291	0.0709	0.02869	0.00041	70.90	28.68
100 krad	0.0373	0.0627	0.0373	0	62.70	37.30
500 krad	0.0292	0.0708	0.0255	0.0037	70.85	25.45

It can be seen that the exposure to γ -rays does not cause a large percentage change in elastic deformation in PUUs, which changes by a maximum of 1 percentile point, remaining stable in a range between 76.6 and 78.6 %. The same is not true for Reverlink®, which exhibits a lower elastic deformation value (70.9 %) for blank aged with the respect to PUUs, which decreases by about 8 percentile points when irradiating with 100 krad, and then returns to around the initial value by increasing radiation to 500 krad. Indeed, a lower elastic deformation percentage of Reverlink® corresponds to higher Q_{max} values than those of PUUs.

Table 4.3 shows the values of E_1 , E_2 and η resulting from the proposed viscoelastic model, which are useful for comparing the viscoelastic behavior of polymers. The $\frac{E_2}{E_1}$ ratio, in the Zener model indicated as relaxation strength, for irradiated and non-irradiated PUUs has an almost constant value of about 3.5, whereas it is lower for Reverlink®. It is shown also the values of σ_0 computed through Eq. 4.27.

Table 4.3: Viscoelastic parameters comparison resulting from the model.

Conditioning	E_1 [MPa]	E_2 [MPa]	η [MPa · s]	σ_0 [MPa]	τ [s ⁻¹]	$\frac{E_2}{E_1}$
PUU 70						
Blank aged	4.03	13.95	10.93	0.313	0.783	3.46
100 krad	10.91	38.90	10.10	0.852	0.260	3.57
500 krad	4.75	15.83	10.81	0.366	0.683	3.33
PUU 80						
Blank aged	4.88	15.98	10.80	0.374	0.676	3.27
100 krad	8.14	29.90	10.19	0.640	0.341	3.67
500 krad	6.36	22.83	10.38	0.498	0.455	3.59
PUU 90						
Blank aged	2.80	9.65	11.96	0.215	1.24	3.44
100 krad	4.69	15.44	10.80	0.360	0.699	3.29
500 krad	3.15	10.67	11.27	0.243	1.057	3.39
PUU 100						
Blank aged	4.23	15.14	11.01	0.329	0.727	3.58
100 krad	7.88	28.78	10.24	0.619	0.356	3.65
500 krad	7.45	26.40	10.27	0.581	0.389	3.55
Reverlink®						
Blank aged	0.56	1.39	13.89	0.040	10	2.47
100 krad	1.34	2.26	15.01	0.084	6.650	1.68
500 krad	0.98	2.73	15.37	0.070	5.640	2.78

PUU 90 is the less rigid polymer of the PUU family, both blank and irradiated, having a lower E_1 and E_2 value than the others. It is also the most viscous, although viscosity has a very similar value for all PUUs. Reverlink® presents a value of E_2 and E_1 approximately one order of magnitude lower than PUUs, it is therefore the less rigid polymer, and this can be clearly seen by simply trying to deform the sample with the hands. The consequence of this is in fact a far lower stress value felt by the material (by an order of magnitude) for the same deformation. Considering the value of η resulting from the model, it is also the one with the highest viscosity, about one and a half times higher than the average PUUs.

The parameter τ is directly related to how quickly the material recovers viscoelastic deformation, so the decay rate. The higher the value, the slower the recovery. Considering the main parameters of self-healing performance, it is evident that the higher is τ , the higher is the value of Δt , and presumably the greater is the volume of air lost (which, however, also depends on the actual total repair of the material). Among the PUUs, it is still PUU 90 that has the highest value, showing in fact, as can be seen in section 3.4, the worst self-healing performance among the samples tested. Considering the aged blanks, Reverlink® presents a value approximately 10 times higher than the PUUs, and this was to be expected when looking at Figure 3.17.

Concerning the changes of viscoelastic properties due to absorbed radiation, Figure 4.14 indicates an increase in polymer stiffness due to γ -irradiation.

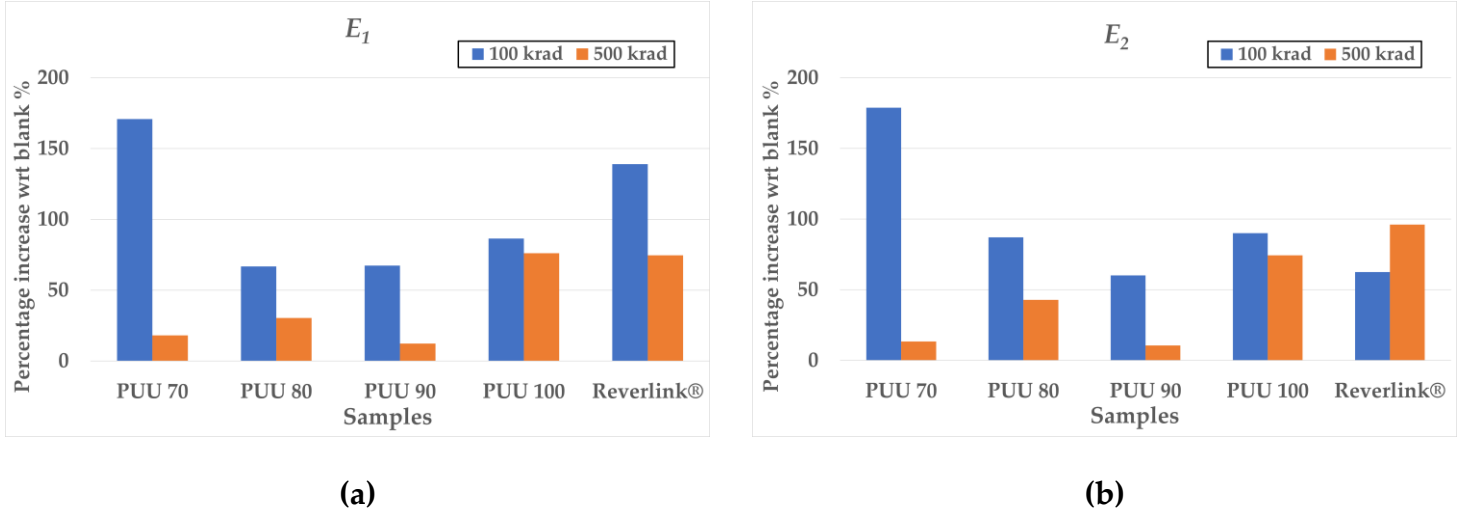


Figure 4.14: E_1 and E_2 percentage changes compared to blanks aged.

Looking at the percentage change due to 100 krad dose, PUU 70 is the polymer that stiffens the most for both springs, with an increase of 170% for E_1 and 180% for E_2 compared to blank aged, while it is the one that stiffens the least, together with PUU 90, considering irradiation at 500 krad. In general, apart from in the case of 100 krad for Reverlink®, the polymers stiffen more with 100 krad exposure than with 500 krad exposure.

This type of behavior, in which performance deteriorates with irradiation at 100 krad and then improves with increasing irradiation, can be seen when considering most of the parameters examined.

If, on the other hand, the viscosity η obtained from the model is taken into account (Figure 4.15), a slight decrease can be seen in the case of PUUs, while the opposite behavior occurs in the case of Reverlink®, with a slight increase in viscosity.

PUU 90 is the polymer that loses the most viscosity due to irradiation, reaching a loss of about 10% for 100 krad compared to the initial blank aged. Again, there is a greater decrease for irradiation at 100 krad, which is then recovered by increasing irradiation to 500 krad. PUU 100 shows no change in viscosity from 100 to 500 krad dose. From the scheme, a small, almost linear trend of decreasing viscosity can be seen from PUU 70 to PUU 100 irradiated at 500 krad. In the case of Reverlink®, on the other hand, viscosity increases by irradiating at 100 krad and increases even more by 500 krad, reaching +10% compared to blank.

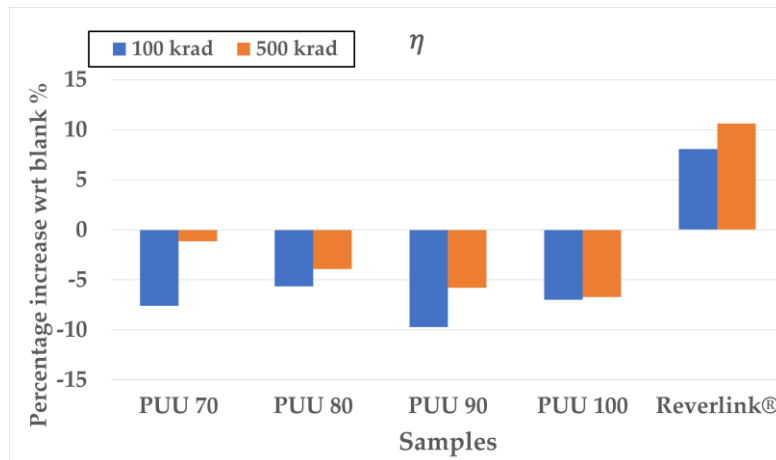


Figure 4.15: Viscosity η percentage changes compared to blanks aged.

As far as the trend in τ is concerned, Figure 4.16 shows a decrease for 100 krad, meaning a better self-healing performance, which is then recovered by increasing the radiation to 500 krad. For PUUs, there seems to be an increasing trend for the value of τ in the 100 krad case, with the exception of PUU 90, and a decreasing trend in the 500 krad case, with the exception of PUU 100.

In the case of Reverlink®, however, the τ value decreases for 100 krad and continues to decrease by increasing radiation. This behavior seems to suggest a faster strain recovery, and thus repair, by increasing the absorbed radiation dose. However, it should be noted, as can be seen in Table 3.11 and Table 3.14, that Reverlink® thickness is about 1.9 mm for blank aged and irradiated samples at 500 krad, and 2.67 mm for the sample irradiated at 100 krad. As previously mentioned, and as evidenced in literature [50], a greater thickness leads to a better self-healing performance. Consequently, a higher τ value for 100 krad than for 500 krad may be due to the large difference in thickness and would probably be lower for the same thickness, continuing the same trend as PUUs.

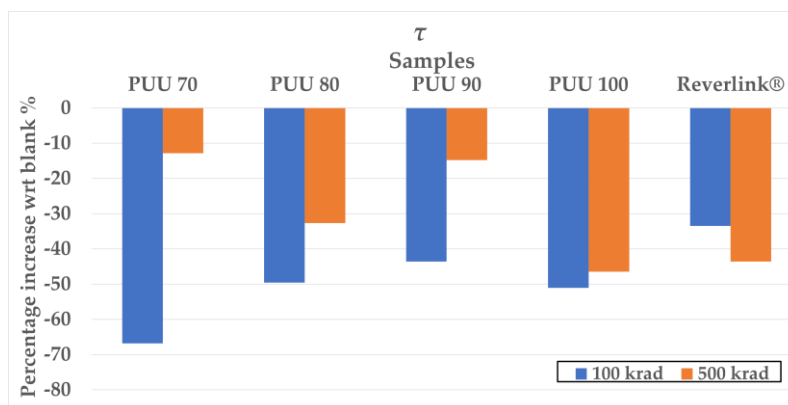


Figure 4.16: τ percentage changes compared to blanks aged.

5. Final considerations and conclusions

Ionizing radiation causes chemical degradation of polymers, which may result in the formation of highly reactive species such as free neutral radicals, cationic and anionic ions or excited molecules. Molecular modifications may consist of molecular chain branching, cross-linking and molecular degradation or scission. In presence of oxygen, degradation by oxidation of the polymer can occur. Figure 5.1 shows the two most common effects of ionization.

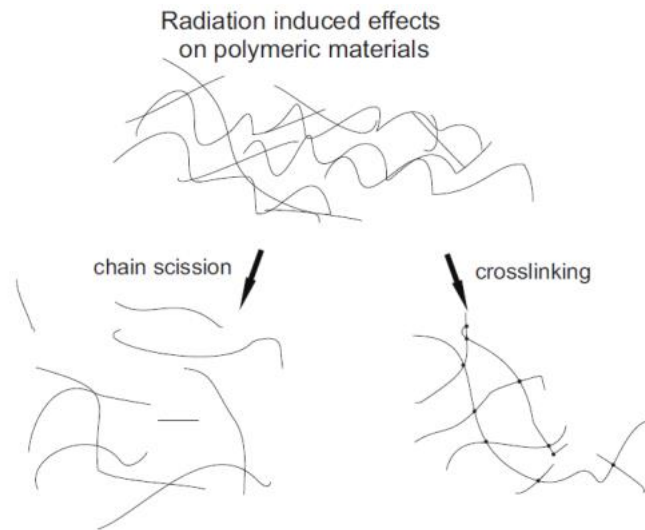


Figure 5.1: Ionizing radiation induced effects on polymeric materials [88].

Crosslinking reactions form new C-C covalent bonds between adjacent molecular chains, forming a three-dimensional network and increasing in this way the molecular weight. Chain scission results in a decrease of the molecular weight of the polymer. Those phenomena coexist during ionization, the prevalence of one over the other depends on several factors such as the morphology of the polymer, the irradiation environment and the initial molecular structure. Irradiation in air, as in our case, has different molecular modifications with the respect to irradiation in vacuum for example. During irradiation in air, the free radicals produced by interaction of ionizing radiation and polymers can react with oxygen, generating polyurethane oxidative degradation and modifying material properties [93, 88] (Figure 5.2).

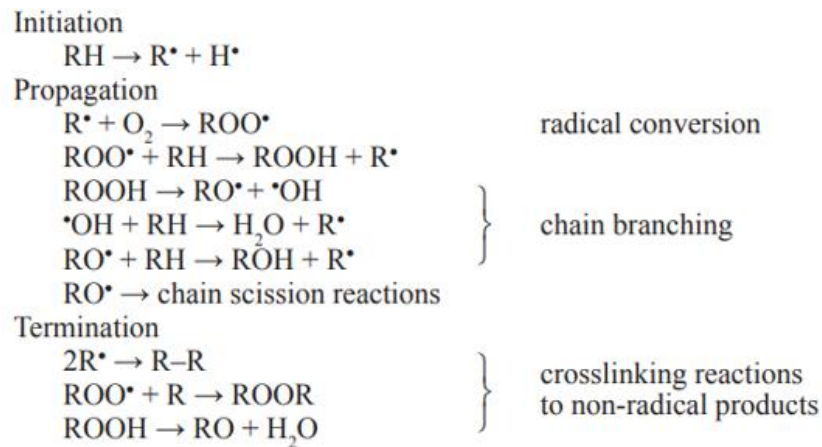


Figure 5.2: Polymer radio oxidation [88].

It must be emphasized that the effect of radiation changes from polymer to polymer, according to the different chemical reactions taking part.

5.1 Radiation effects on polymer's properties

Considering the results obtained in section 3.4.4, Figure 5.3 shows the percentage change in the Q_{max} of the irradiated samples compared to blank aged. It is possible to see more schematically the opposite behavior of PUUs compared to Reverlink®, where the former exhibit a decrease in maximum flow rate, while the latter a large increase for 100 krad and a slight increase for 500 krad.

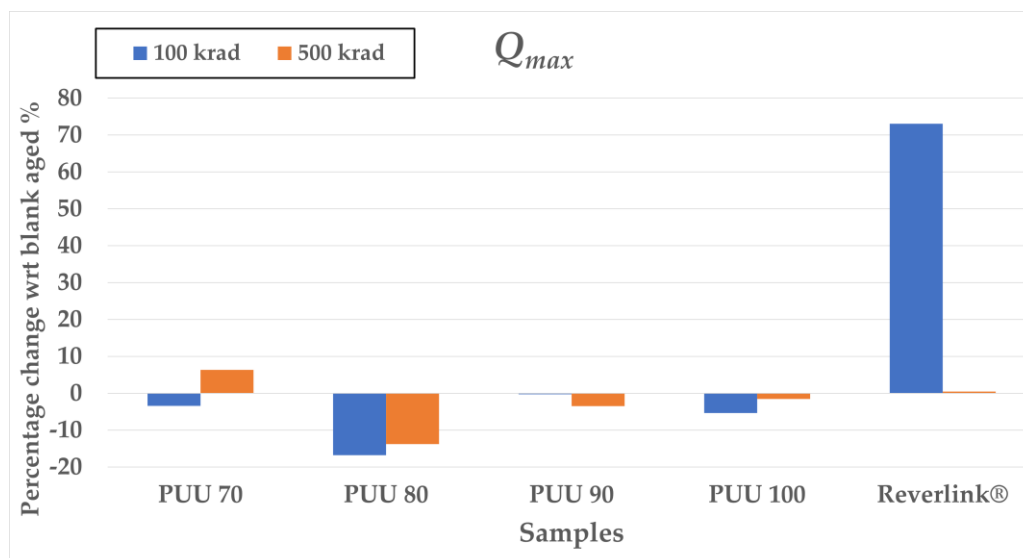


Figure 5.3: Q_{max} percentage change of irradiated samples with the respect to blanks.

Rather than the maximum flow rate, the most relevant parameter among the ones considered for the assessment of the self-healing performance is the air volume lost during the test. Figure 5.4 clearly show a high percentage decrease in volume leakage during the test with the respect to blank aged for PUUs (except for PUU 100 that doesn't repair), while an increase for Reverlink®.

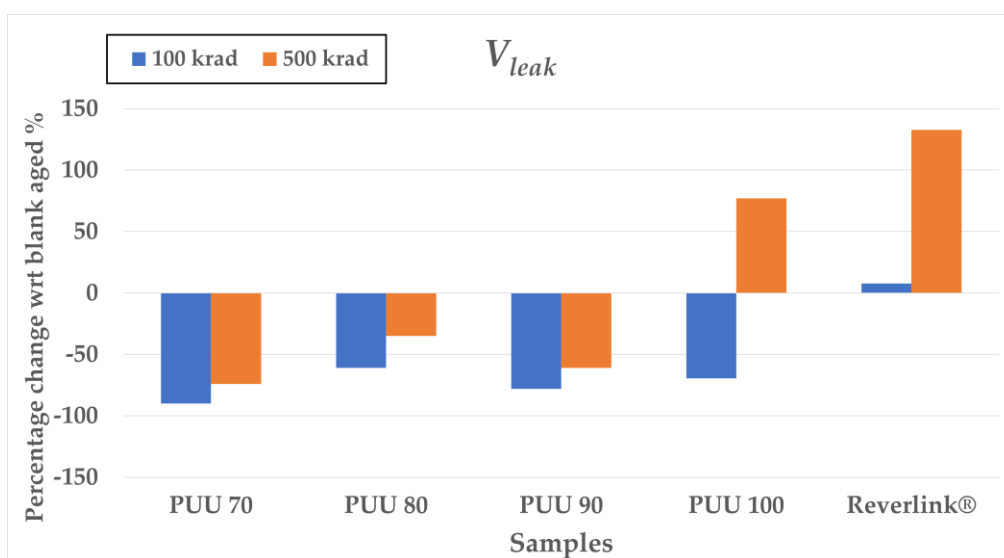


Figure 5.4: Air volume lost percentage change during the tests.

This result, which shows an improvement in performance following exposure to radiation, contrasts with the expected one. Wallin and Pernigoni have investigated the change in self-healing performance of PUUs following 10 krad dose γ -radiation, immediately after manufacturing. The test result showed a performance deterioration due to irradiation, although the amount was not so significant. In our case the radiation dose is 10 and 50 times higher (100 and 500 krad), showing however an improvement in self-healing performance.

The reason for this improvement lies in the bond nature of PUUs. Indeed, they contain a high content of reversible non-covalent hydrogen bonds and a low constant content of covalent disulphide bonds (6.2 %). Hydrogen bonds are those mainly involved in the healing process and are typically found in the four structures shown in Figure 5.5.

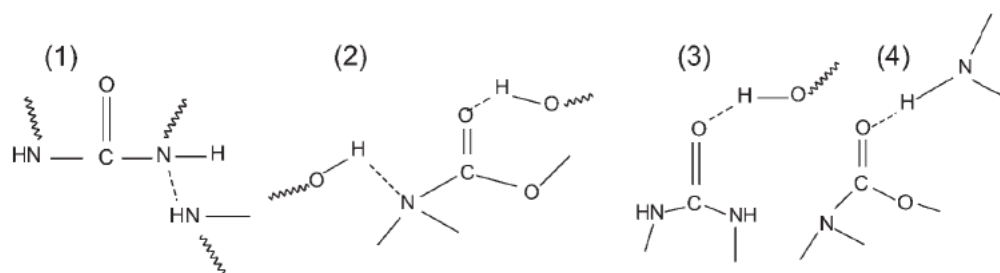


Figure 5.5: H bonds between N in urea linkage and H of an amino group (1), between O of a urethane group and H of hydroxyl group (2), between O of urea linkage and H of hydroxyl group (3), between O of a urethane group and H of an amino group (4) [92, 31].

As the radiation dose experienced increases, the most prevalent mechanism in polymers where hydrogen bonds are present is chain scissioning [89]. This mechanism reduces the molecular weight of the polymer, causing an increase in chain mobility, thus a faster strain recovery and consequently a better self-healing performance. A decrease in viscosity due to this phenomenon is indeed shown by the model considered (Figure 4.15). The scissioning mechanism is also responsible for an increase in the degree of crystallinity of the polymer, with a consequent increase in stiffness, as can be seen in Figure 4.14, and an higher elastic deformation percentage (evident from the decrease in the Q_{max} value). An improvement in the τ value, hence in the polymer's recovery rate, results from the viscoelastic model considered.

No particular trend towards increasing trifunctional:difunctional ratio for PUUs is evident from the results. PUU 90 tends to be the worst performing one for the sets considered, while PUU 80 is the best performing one. It can be said that, experimentally, for those precise compositions of PUUs there is the worst and best self-healing performance among PUUs, respectively. Finally, from Figure 5.4, it can be seen that PUU 70 is the polymer that improves self-healing performance the most due to irradiation.

In order to compare and justify the results obtained in this thesis work with those obtained by Pernigoni and Wallin, it can be hypothesized that initially, for small doses of γ -radiation, the main mechanism experienced is crosslinking. The performance degradation would then be due to an increase in the molecular weight of the polymer due to the formation of a network of chains, resulting in lower chain mobility and thus slower strain recovery. By increasing the radiation dose to 100 krad, the predominant mechanism becomes chain scissioning, which instead increases mobility and strain recovery. For a radiation dose of 500 krad, the first signs of degradation, probably of the hydrogen bonds responsible for the material's self-healing mechanism, start to

appear. This slightly worsens the material's self-healing efficiency, which nevertheless remains better than the one for blank aged. According to these assumptions, increasing the absorbed radiation dose will again tend to worsen the material's self-healing response.

Reverlink®, on the other hand, exhibits the opposite behavior, thus worsening the self-healing efficiency with increasing radiation dose. The reason for this can again be found in the nature of the polymer bonds. They consist of weak hydrogen bonds and strong irreversible covalent bonds (50:50 mol% ratio). As introduced before, polymers where hydrogen bonds are present, especially supramolecular polymers, undergo mostly chain scission due to γ -irradiation [89], while the regions of the polymer with irreversible covalent bonds undergo a crosslinking mechanism. Since in Reverlink® the latter are much stronger than the hydrogen bonds, the effects of crosslinking will prevail. For this reason, overall, the polymer undergoes an increase in molecular weight and thus a decrease in chain mobility. The viscoelastic model considered indeed shows an increase in viscosity and stiffness of the polymer [90, 91]. By increasing the radiation dose, the crosslinking mechanism becomes so important that hinders the self-healing process, which is actually attributable to hydrogen bonds. This is why the puncture test results show a missed repair of the polymer at 500 radiation dose. When the two effects are combined, however, the polymer shows an improvement in the τ value after irradiation for the model considered.

Nevertheless, for both PUUs and Reverlink®, slight changes in material behavior due to irradiation are observable from the test results. Indeed, taking into account the characterization performed on them, no significant variations are evident from a chemical and molecular point of view (Sections 3.1, 3.2, 3.3).

It has to be stressed that the derived argumentation was carried out based on the initial approximation that the ageing effect on blank and irradiated samples is similar. Thus, when comparing the results for the different sets, only the effect of radiation on polymers was evaluated. For a more extensive and complete comparison, it would be necessary to test the just-irradiated samples immediately after the manufacturing of them, as well as to test a set of irradiated samples one year after manufacturing. This, however, still would not be a perfect representation of the space environment, in which ageing and irradiation occur simultaneously over time.

5.2 Ageing effect on polymer's properties

The assessment of the effect of ageing on the self-healing performance of the polymers tested is not in the scope of this master's thesis, but a suggested explanation is nevertheless presented in this section.

As already introduced, comparing the results of puncture tests obtained for the blanks just after manufacturing [50] and for blanks tested one year after manufacturing, a slight worsening of the self-healing performance of the PUUs, and a great improvement for Reverlink® is evidenced (Table 3.27). The samples, during the year between the first tests and the later ones, were kept wrapped in special plasticized paper in laboratory. They were, as illustrated in section 2.2.5, degassed prior to the last puncture tests in order to remove the absorbed moisture.

The percentage change in maximum flow rate and the lost volume for PUUs moving from the initial test results to those after one year is shown in Figure 5.6.

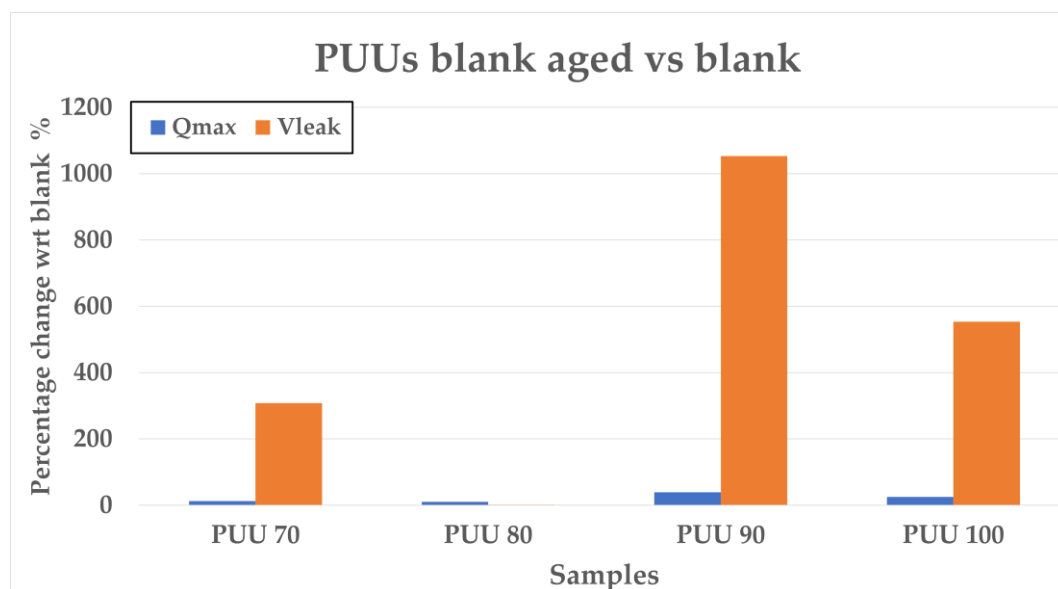


Figure 5.6: Q_{max} and V_{leak} percentage change of PUUs due to ageing.

This change, therefore, may be due to contact of the polymer with oxygen, leading to oxidation reactions, or to reactions due to the moisture absorbed during this time. Again, morphology, crystallinity and the nature of polymer bonds are key parameters that affect this process [94]. In the case of PUUs, there has probably been crosslinking due to ageing and contact with oxygen, which has led to a decrease in mobility and a worsening of self-healing efficiency. This deterioration is even greater, however, considering the fact that the thickness of aged blanks is about twice that of normal blanks. This suggests that reducing the thickness to 1 mm even for aged blanks would probably lead to much worse results. In general, furthermore, during ageing the volume of the polymer reduces, which further slows down the mobility of the polymer molecules [95]. In addition, observing the slight increase in Q_{max} , the effect of ageing for PUUs is also a slight decrease in elasticity.

For Reverlink®, however, there is a great improvement in performance after one year. In Figure 5.7 are shown, for the sake of simplicity, the maximum flow rate Q_{max} and V_{leak} values for Reverlink® blank and blank aged. Initially, the sample was unable to repair itself, even reaching a lost air volume of 5 liters. This improvement in performance may be due, for similar and opposite reasons to the irradiation case, to a prevailing mechanism of chain scission, caused by oxidation and moisture. It can be noted, from the decrease in the Q_{max} value, that there is a net increase in the elasticity of the polymer and a much greater chain mobility leading to a much faster recovery. More in-depth studies on the molecular change of the polymer one year after manufacturing could explain the reason for such a marked improvement in self-healing efficiency.

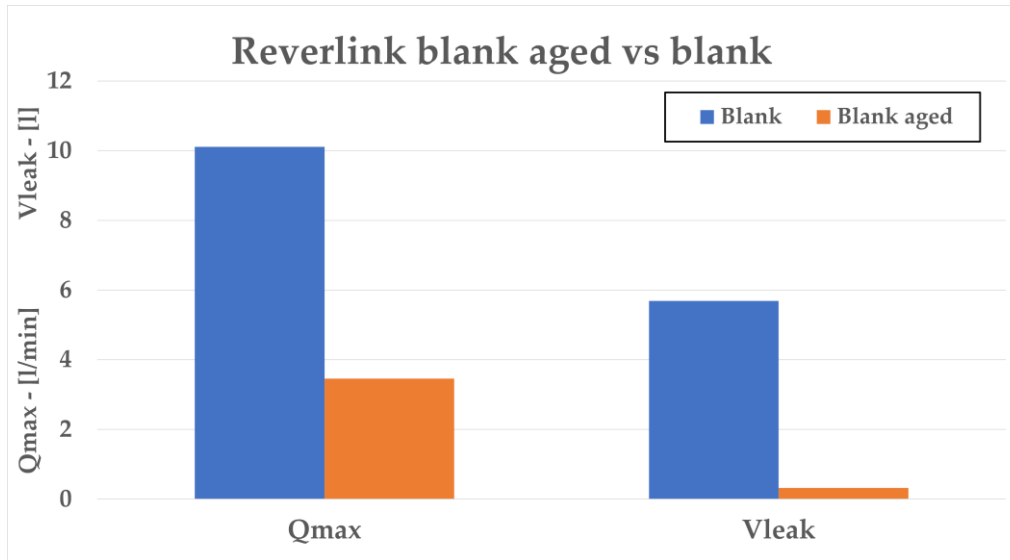


Figure 5.7: Q_{max} and V_{leak} change of Reverlink® due to ageing.

5.3 Conclusions

The purpose of this master's thesis was to assess the change in self-healing performance following γ -ray irradiation for two types of polymers: a supramolecular polymer, the Arkema Reverlink®, and four different poly(urea-urethane)s, varying their crosslinking density. The purpose of this is to evaluate the suitability of these in space applications, in particular inflatable structures (as habitats or space suits), as a result of the effects of radiation to which they are exposed in space.

Space radiation exposure was performed by simulation with the Co60 facility provided by ESA-ESTEC for two sets of samples, for radiation doses of 100 krad (1000 Gy) and 500 krad (5000 Gy) respectively.

Subsequently, the two sets of irradiated samples were characterized by ATR-FTIR spectroscopy, DSC and TGA analysis. The results of the tests were then compared with the results obtained on blank samples, to assess whether a possible chemical and molecular change had occurred. From the comparison, no significant changes emerged due to irradiation. This result indicates that the polymer does not degrade to a point where chemical or molecular changes are shown for such a dose of radiation.

The assessment of self-healing performance was carried out by means of puncture tests. From the test results, four parameters were considered as healing performance indicators: the maximum and minimum flow rate, the time between the two, and the total volume of air lost during the test. The latter parameter is considered as the most important one since the material, in order to be considered suitable for space applications, must lose as less air volume as possible. This requirement is critical for the safety of the crew, to minimize oxygen loss, and for the inflatable structure, to maintain its rigidity.

Initially, the test results for the two irradiated polymer's sets should have been compared directly with the results obtained from puncture tests performed on the blanks just after manufacturing (October 2022). For scrupulousness, tests were carried out on the same blanks approximately one year after manufacturing (September 2023), from which some differences emerged. In particular, a slight deterioration for PUUs and a marked improvement for Reverlink®, which was not able to repair itself initially.

As the samples were irradiated in October 2022 and tested in September 2023 (thus one year later) as well, it was decided to compare the test results not with those for blanks after manufacturing, but with those for blanks after one year (aged blanks). In this way, it was intended to assess only the effect of irradiation, separating it from that of ageing. A further reason for this choice was the difference in thickness with the samples tested after manufacturing.

A viscoelastic model based on the Zener model was also proposed to evaluate the change in viscoelastic properties of polymers based on the results of puncture tests.

For PUUs, the results of the comparison show an improvement in self-healing performance, an unexpected result when considering similar tests in the literature. This, also taking into account changes in the parameters of the proposed viscoelastic model, was attributed to a chain scission mechanism due to irradiation. In addition, the results did not show a clear performance trend when varying the crosslinking density. On the other hand, from the results obtained, Reverlink® showed a deterioration in self-healing efficiency due to irradiation, not repairing completely for a radiation dose of 500 krad. This effect was attributed to a crosslinking mechanism prevailing over chain scissioning.

Overall, the results of the test comparison show that among the two types of polymers tested, PUUs clearly had a better self-healing efficiency than Reverlink®. PUUs were also found to be poorly susceptible to the radiation doses considered, even showing an improvement in performance. Reverlink® exhibited however good results for low radiation doses, while a loss of self-healing capacity for higher doses.

Finally, at the end of this study, it can be concluded that PUUs may really be candidates for space applications such as inflatable habitats and spacesuits, but further tests should be carried out to assess the change in performance due to other damaging agents present in the space environment (such as UV, thermal solicitations, ATOX and higher radiation doses), ageing and humidity.

5.4 Future developments

In order to make a more accurate assessment of how self-healing efficiency changes due to irradiation, further aspects should be considered, as introduced above.

- Since the effect of ageing could be different on the already irradiated samples and blanks, puncture tests should be performed on the newly irradiated materials immediately after manufacturing, comparing them with the blanks. This would directly evaluate the effect of radiation on self-healing performance, removing the possible different effect of ageing on the samples.
- To avoid the oxidation process of the material and to analyze the evolution of radicals, the irradiation process must be performed in an inert environment, e.g. in liquid nitrogen.
- Since the effect of thickness on the self-healing performance of polymers is known, puncture test comparisons between samples irradiated with different doses of radiation and blanks, with the same thickness, would give even more precise results on the effect of irradiation.
- There is evidence in literature of the different effects on polymer properties for different irradiation dose rates [96]. Puncture tests on samples irradiated with the same radiation dose but different radiation rate doses, could be performed in order to assess whether there is a significant effect on self-healing performance for different rates. The irradiation rates to be considered for the tests should be based on the average values present in the regions where the material should be used in the space applications.
- To assess the effect of ageing on the samples, the samples could be characterized post manufacturing and years later, with the same thickness, in order to evaluate the effect only of ageing on self-healing performance.

Bibliography

- [1] Micrometeoroids and Orbital Debris (MMOD), NASA website.
- [2] https://en.wikipedia.org/wiki/Space_debris#cite_note-3
- [3] J.-C. Liou, PhD NASA Chief Scientist for Orbital Debris. *“Orbital Debris Challenges for Space Operations”*. The Second ICAO / UNOOSA Symposium Abu Dhabi, United Arab Emirates, 15-17 March 2016.
- [4] Zilong Jiao, Lixiang Jiang, Jipeng Sun, Jianguo Huang and Yunfei Zhu. *“Outgassing Environment of Spacecraft: An Overview”*. Published under licence by IOP Publishing Ltd.
- [5] R. Pastore, A. Delfini, M. Albano, A. Vricella, M. Marchetti, F. Santoni, F. Piergentili, *“Outgassing effect in polymeric composites exposed to space environment thermal-vacuum conditions”*, Acta Astronautica, 2020.
- [6] Haemmerle V R and Gerhard J H *“Cassini Camera Contamination Anomaly: Experiences and Lessons Learned (Jet Propulsion Laboratory)”*, 2006.
- [7] Zicai Shen, Yan Xia, Yuming Liu, Yigang Ding and Chunqing Zhao. *“Protection of Materials from Space Radiation Environments on Spacecraft”*, 2019.
- [8] Nuclear and Space Radiation Effects on Materials - Space Vehicle Design Criteria. NASA.
- [9] Joseph Barthel, Nesrin Sarigul-Klijn, *“A review of radiation shielding needs and concepts for space voyages beyond Earth’s magnetic influence”*, Progress in Aerospace Sciences, 2019.
- [10] Brandon E.A. Holmes, Vitor T.A. Oiko, Peter C.E. Roberts, *“A review of satellite-based atomic oxygen sensing methods”*, Progress in Aerospace Sciences, Volume 137, 2023.
- [11] Bruce A. Banks, Jane A. Backus, Michael V. Manno, Deborah L. Waters, Kevin C. Cameron, Kim K. de Groh. *“Atomic oxygen erosion yield prediction for spacecraft polymers in low earth orbit”*, NASA, 2009.
- [12] Kim K. de Groh, Bruce A. Banks and Loredana Santo. Materials International Space Station Experiment-9 (MISSE-9) Polymers and Composites Experiment. 2018.
- [13] A. Rekondo, R. Martin, A. Ruiz de Luzuriaga, G. Cabanero, H.J. Grande, I. Odriozola, *“Catalyst-free room-temperature self-healing elastomers based on aromatic disulfide metathesis”*, Mater. Horiz, 2014.

- [14] A.M. Grande, R. Martin, I. Odriozola, S. van der Zwaag, S.J. Garcia. "Effect of the polymer structure on the viscoelastic and interfacial healing behaviour of poly(urea-urethane) networks containing aromatic disulphides", *European Polymer Journal*, Volume 97, 2017.
- [15] <https://rtilab.com/techniques/ftir-analysis/>
- [16] FTIR Sample Techniques: Attenuated Total Reflection (ATR). Thermo Fisher scientific website.
- [17] Tianlong Zhang, Fengwei Xie, Julius Motuzas, Peter Bryant, Valsala Kurusingal, John M. Colwell, Bronwyn Laycock, "Early-stage photodegradation of aromatic poly(urethane-urea) elastomers", *Polymer Degradation and Stability*, Volume 157, 2018.
- [18] L. Lee. "Specialty polymers and polymer processing". *Comprehensive Polymer Science and Supplements*, 1989.
- [19] G. Sala; L. Di Landro; A. Airoidi; P. Bettini. "Tecnologie e materiali aerospaziali", 2019.
- [20] C. Vest. "The effects of space environment on spacecraft surfaces". *Johns Hopkins APL Technical Digest*, 12, 1991.
- [21] D. E. Case and J. A. Nabity. "An aerospace engineering guide to space radiation: Science and strategies". 47th International Conference on Environmental Systems, 2017.
- [22] S. Zhang et al. "First measurements of the radiation dose on the lunar surface". *Science Advances*, 6, 2020.
- [23] S. Hu. "Solar Particle Events and Radiation Exposure in Space", 2017.
- [24] J. Rask et al. "Space faring the radiation challenge, an interdisciplinary guide on radiation and human space flight".
- [25] A. Gabbana. "Characterization of the self-healing behavior of a supramolecular elastomer for space applications", 2019.
- [26] R. Vaiyapuri; B. W. Greenland; H. M. Colquhoun; J. M. Elliott; W. Hayes. "Evolution of supramolecular healable composites: A mini-review". *Polymer International*, 2014.
- [27] N. Zhong; W. Post. "Self-repair of structural and functional composites with intrinsically self-healing polymer matrices: A review". *Composites Part A: Applied Science and Manufacturing*, 69:226–239, 2015.
- [28] L. Brunsveld; B. J. B. Folmer; E. W. Meijer; R. P. Sijbesma. "Supramolecular Polymers". *Chemical Reviews*, 2001.
- [29] Reverlink introduction. Arkema.

- [30] A. Bressi. *"Self-healing supramolecular materials applied to space suits: a study of neat polymers, multi-layers and nanocomposites"*, 2021.
- [31] G. Wallin. *"Repairing ability of Dynamic Covalent Polymer Networks under simulated space radiation environment"*, 2021.
- [32] S.J. Kalista. *"Self-Healing of Thermoplastic Poly(Ethylene-co-Methacrylic Acid) Copolymers Following Projectile Puncture"*, 2003.
- [33] S. Coppi. *"Analisi sperimentale del comportamento di un polimero autoriparante e sviluppo preliminare di un modello viscoelastico"*, 2011.
- [34] Surlyn 8940, Product Data Sheet.
- [35] R. Fall. *"Puncture Reversal of Ethylene Ionomers – Mechanistic Studies"*, 2001.
- [36] Laura Pernigoni, Antonio M. Grande, *"Development of a supramolecular polymer based self-healing multilayer system for inflatable structures"*, Acta Astronautica, Volume 177, 2020.
- [37] S. K. Ghosh. *"Self-healing materials: Fundamentals, design strategies, and applications"*. Wiley, 2009.
- [38] Chemical Retrieval on the Web. Polymer properties database: Elastomers.
- [39] L. Pernigoni. *"Towards safer space suits with self-healing functionality"*, 2018.
- [40] A. Ravve. *"Principle of polymer chemistry"*. Springer Science, 1995.
- [41] W. D. Callister Jr; D. G. Rethwisch. Materials Science and Engineering: chapter 15. Wiley, 8th edition, 2009.
- [42] T. Szmechtyk; N. Sienkiewicz; J. Wozniak; K. Strzelec. *"Polyurethanes as self-healing materials"*. Current Chemistry Letters, 2015.
- [43] K. S. Toohy; N. R. Sottos; J. A. Lewis; J. S. Moore; S. R. White. *"Self-healing materials with microvascular networks"*. Nature Materials, 2007.
- [44] R. H. Aguirresarobe, S. Nevejans, B. Reck, L. Irustaa, H. Sardona, J. M. Asuaa, and N. Ballarda. *"Healable and self-healing polyurethanes using dynamic chemistry"*. Progress in Polymer Science, 2021.
- [45] B. Blaiszik, S. Kramer, S. Olugebefola, J. Moore, N. . Sottos, and S. White. *"Selfhealing polymers and composites"*. Annual Review of Materials Research, 2010.
- [46] A. Grande, S. Garcia, and S. van der Zwaag. *"On the interfacial healing of a supramolecular elastomer"*. Polymer, 2015.
- [47] M. D. Hager, P. Greil, C. Leyens, S. van der Zwaag, and U. S. Schubert. *"Self-healing materials"*. Advanced Materials, 22:5424–5430, 2007.

- [48] V. Montano, A. Smits, and S. J. Garcia. *"The bio-touch: Increasing coating functionalities via biomass-derived components"*. Surface and Coatings Technology, 2017.
- [49] S. van der Zwaag, A. Grande, W. Post, S. Garcia, and T. Bor. *"Review of current strategies to induce self-healing behaviour in fibre reinforced polymer based composites"*. Materials Science and Technology, 2014.
- [50] L. Pernigoni. *"Self-healing materials for flexible space structures"*, PhD thesis, 2023.
- [51] D. Montarnal, F. Tournilhac, M. Hidalgo, and L. Leibler, *"Epoxy-based networks combining chemical and supramolecular hydrogen-bonding crosslinks"*, Journal of Polymer Science Part A: Polymer Chemistry, 2010.
- [52] F. Sordo, S. Mougner, N. Loureiro, F. Tournilhac, and V. Michaud, *"Design of Self-Healing Supramolecular Rubbers with a Tunable Number of Chemical Cross-Links"*, Macromolecules, 2015.
- [53] Pernigoni, L., Lafont, U. & Grande, A.M. *"Self-healing materials for space applications: overview of present development and major limitations"*. CEAS Space, 2021.
- [54] K.L. Bedingfield, R.D. Leach, and M.B. Alexander. *"Spacecraft System Failures and Anomalies Attributed to the Natural Space Environment"*, NASA Reference Publication 1390, 1996.
- [55] Jun Chen, Nengwen Ding, Zhifeng Li, Wei Wang, *"Organic polymer materials in the space environment"*, Progress in Aerospace Sciences, Volume 83, 2016.
- [56] Yifan Lu, Qi Shao, Honghao Yue, and Fei Yang. *"A Review of the Space Environment Effects on Spacecraft in Different Orbits"*, 2019.
- [57] Goyal, M., Agarwal, S. N., Bhatnagar, *"A review on self-healing polymers for applications in spacecraft and construction of roads"*, J. Appl. Polym. Sci., 2022.
- [58] White, S., Sottos, N., Geubelle, P. et al. *"Autonomic healing of polymer composites"*. Nature 409, 2001.
- [59] A.R. Hamilton, N.R. Sottos, S.R. White, *"Mitigation of fatigue damage in self-healing vascular materials"*, Polymer, 2012.
- [60] S. Zainuddin, T. Arefin, A. Fahim, M.V. Hosur, J.D. Tyson, Ashok Kumar, J. Trovillion, S. Jeelani, *"Recovery and improvement in low-velocity impact properties of e-glass/epoxy composites through novel self-healing technique"*, Composite Structures, 2014.
- [61] A. Francesconi, C. Giacomuzzo, A. M. Grande, T. Mudric, M. Zaccariotto, E. Etemadi, L. Di Landro, U. Galvanetto, *"Comparison of self-healing ionomer to aluminium-alloy bumpers for protecting spacecraft equipment from space debris impacts"*, Adv. Space Res. 2013.

- [62] Wu, X. F., Rahman, A., Zhou, Z., Pelot, D. D., Sinha-Ray, S., Chen, B., Payne, S., & Yarin, A. L. “*Electrospinning core-shell nanofibers for interfacial toughening and self-healing of carbon-fiber/epoxy composites*”. *Journal of Applied Polymer Science*, 2013.
- [63] <https://www.safework.nsw.gov.au/hazards-a-z/ionising-and-non-ionising-radiation>
- [64] <https://en.wikipedia.org/wiki/Radiation>
- [65] N. H. R. P. Engagement and Communications. Space radiation, 2019.
- [66] https://en.m.wikipedia.org/wiki/File:Van_Allen_Radiation_Belt_Model_shown_with_2_VA_Probes.jpg
- [67] <https://en.wikipedia.org/wiki/Cobalt-60>
- [68] https://www.esa.int/Enabling_Support/Space_Engineering_Technology/ESA_s_cobalt-60_irradiation_facility_gains_ISO_quality_stamp
- [69] E. J. Brandon et al., “*Structural health management technologies for inflatable/deployable structures: Integrating sensing and self-healing*”, *Acta Astronautica*, 2011.
- [70] Kriss J Kennedy. “*ISS TransHab: Architecture Description*”. Tech. rep. SAE Technical Paper, 1999.
- [71] Litteken, Douglas. “*Inflatable technology: using flexible materials to make large structures*”. NASA Johnson Space Center, 2101 NASA Parkway, Houston, TX, USA, 2019.
- [72] https://en.wikipedia.org/wiki/Space_suit
- [73] https://en.wikipedia.org/wiki/Extravehicular_Mobility_Unit
- [74] Cucinotta, Shavers, Saganti, Miller. “*Radiation Protection Studies of International Space Station Extravehicular Activity Space Suits*”, 2003.
- [75] T. Fredrickson, “*NASA research announcement final report for space suit survivability enhancement*”, NASA, Tech. Rep., 1998.
- [76] Standard Test Method for Protective Clothing Material Resistance to Puncture.
- [77] J. Connolly and N. M. S. C. Team. “*Deep space transport (DST) and mars mission architecture*”, 2017.
- [78] Lombardo, Giuseppe & Serrao, Sebastiano & Rosati, Marianna & Lombardo, Marco. “*Analysis of the Viscoelastic Properties of the Human Cornea Using Scheimpflug Imaging in Inflation Experiment of Eye Globes*”, 2014.

- [79] M. Rampf, O. Speck, T. Speck, and R. H. Luchsinger, "Self-repairing membranes for inflatable structures inspired by a rapid wound sealing process of climbing plants", *Journal of Bionic Engineering*, vol. 8, 2011.
- [80] https://en.wikipedia.org/wiki/Standard_linear_solid_model.
- [81] Chabert, France & Tournilhac, Francois & Sajot, Nicolas & Tencé-Girault, Sylvie & Leibler, Ludwik. "Supramolecular polymer for enhancement of adhesion and processability of hot melt polyamides. *International Journal of Adhesion and Adhesives*", 2010.
- [82] A. R. Brás, W. Antonius, W. Pyckhout-Hintzen, J. Allgaier. "Self-Healing Elastomers Using Supramolecular Approaches", 2012.
- [83] Willis, Paul & Hsieh, Cheng-Hsien. "Space Applications of Polymeric Materials". Kobunshi, 2000.
- [84] https://it.wikipedia.org/wiki/Maximum_Absorbency_Garment.
- [85] E. Grossman, I. Gouzman, "Space environment effects on polymers in low earth orbit", *Nuclear Instruments and Methods in Physics Research Section B: Beam Interactions with Materials and Atoms*, Volume 208, 2003.
- [86] Iskanderova, Z., Kleiman, J., Mojazza, B. M. "Erosion protection and surface conductivity enhancement of TOR polymers by Implantox™ technology" *Proceedings of the 9th International Symposium on Materials in a Space Environment*, 16-20 June 2003.
- [87] Alison Shapiro. "Polymers in Space".
- [88] Sun, Y. and Chmielewski, A.G. "Applications of Ionizing Radiation in Materials Processing", 2017.
- [89] I. V. Revina, "Investigation of supramolecular structures of irradiation-modified and filled polytetrafluoroethylene," *International Siberian Conference on Control and Communications (SIBCON)*, Omsk, Russia, 2015.
- [90] Chandak A, Dhull SB, Punia Bangar S, Rusu AV. "Effects of Cross-Linking on Physicochemical and Film Properties of Lotus", (*Nelumbo nucifera G.*) Seed Starch. *Foods*. 2022.
- [91] Huang, Jinrui and Fu, Pan and Li, Wenbin and Xiao, Laihui and Chen, Jie and Nie, Xiaolan. "Influence of crosslinking density on the mechanical and thermal properties of plant oil-based epoxy resin", 2022.
- [92] M. Abd Elrehim, B. VOIT, B. Bruchmann, K. Eichhorn, K. Grundke, and C. Bellmann. "Structural and end-group effects on bulk and surface properties of hyperbranched poly(urea urethane)s", 2005.

- [93] R. Parvu, C. Podina, T. Zaharescu, and S. Jipa. *“Stability evaluation of polyurethane coatings by gamma irradiation”*. 2010.
- [94] S.G. Nunes, R. Joffe, N. Emami, P. Fernberg, S. Saseendran, A. Esposito, S.C. Amico, J. Varna, *“Physical aging effect on viscoelastic behavior of polymers”*, Composites Part C: Open Access, Volume 7, 2022.
- [95] Physical aging, viscoelasticity.info.com.
- [96] Hui Guo, Zirong Zhou, Meng Gu, Anfeng Yu, Xiaodong Ling, Weitang Yao, *“Preparation of impact-resistant functional polyurea coatings and effect of γ -ray irradiation on its microstructure and performance”*, Progress in Organic Coatings, Volume 161, 2021.

List of Figures

Figure 1.1: Electromagnetic spectrum damages [63].	10
Figure 1.2: Van Allen Belts [66].	12
Figure 1.3: Solar Particle Events [31].	13
Figure 1.4: ATOX chemical reaction [20].	14
Figure 1.5: Atomic oxygen undercutting degradation of the solar array wing blanket box cover on ISS [12].	15
Figure 1.6: NASA simulation of MMOD near the earth and in LEO over the years [3].	16
Figure 1.7: Material mass in Earth Orbit during the years [3].	16
Figure 1.8: Glow in image of planet due to contamination of spacecraft Cassini. Left: no contamination. Right: contamination [6].	18
Figure 1.9: Radiant thermal energy sources of heat of the spacecraft [56].	19
Figure 1.10: Damage management: traditional materials (grey) and self-healing materials (red and blue) [30].	20
Figure 1.11: Damages that could be repaired by Self-healing materials [30].	20
Figure 1.12: Classification of self-healing polymers [57].	21
Figure 1.13: Microcapsules (left) [43] and healing process (right) [47].	22
Figure 1.14: Microvascular network [43].	23
Figure 1.15: Intrinsic self-healing mechanism [43].	24
Figure 1.16: Cylindrical and toroidal inflatable habitats on the lunar surface [69].	30
Figure 1.17: TransHab internal view and cutaway model [70].	31
Figure 1.18: BEAM module inflation progression, from top left to bottom right [71].	31
Figure 1.19: Fabric material layup used for the arms and the legs of the EMU [74].	32
Figure 1.20: Major components of the EMU space suit assembly and support system [74].	33

Figure 2.1: Typical chemical formula of a PUU molecule.	34
Figure 2.2: (a) trifunctional PPG, (b) bifunctional PPG, (c) disulphide linker [14].	35
Figure 2.3: Curing process [14].	35
Figure 2.4: Arkema’s Reverlink® HR.	37
Figure 2.5: Preparation of the Reverlink® HR disk [50].	37
Figure 2.6: PUU80 circular sample [50].	38
Figure 2.7: DSC instruments.	39
Figure 2.8: Mettler Toledo TGA/DSC 3+ device.	40
Figure 2.9: VERTEX 70v spectrometer configuration [50].	40
Figure 2.10: Co60 irradiation facility at ESA ESTEC [68].	41
Figure 2.11: Cylindrical pressure vessel.	42
Figure 2.12: Schematic representation.	43
Figure 2.13: Test setup.	43
Figure 2.14: Example of samples between polyamide films.	45
Figure 2.15: Puncture test machine and puncture event.	45
Figure 2.16: Oven and dryer apparatus in DAER laboratory.	47
Figure 3.1: DSC results for the different PUUs [50].	48
Figure 3.2: DSC result for Reverlink® [50].	49
Figure 3.3: DSC results comparison of blank and irradiated PUUs [50].	50
Figure 3.4: DSC results comparison of blank and irradiated Reverlink®.	51
Figure 3.5: DSC results between blank and irradiated aged Reverlink®.	52
Figure 3.6: TGA curves results for PUUs [50].	53
Figure 3.7: TGA curves results for Reverlink® [50].	54
Figure 3.8: ATR-FTIR spectra comparison for PUUs [50].	55
Figure 3.9: ATR-FTIR spectrum for Reverlink® [50].	56
Figure 3.10: ATR-FTIR spectra comparison of blank and irradiated PUU 70.	56
Figure 3.11: ATR-FTIR spectra comparison of blank and irradiated PUU 80.	57
Figure 3.12: ATR-FTIR spectra comparison of blank and irradiated PUU 90.	57
Figure 3.13: ATR-FTIR spectra comparison of blank and irradiated PUU 100.	57

Figure 3.14: ATR-FTIR spectra comparison of blank and irradiated Reverlink®.....	58
Figure 3.15: Flow rate curves for blank aged PUUs.	62
Figure 3.16: Flow rate curve for Reverlink® blank aged.	63
Figure 3.17: Flow rate curves for blank aged comparison.....	63
Figure 3.18: Flow rate curves for PUU 70 irradiated by 100 krad dose.....	64
Figure 3.19: Flow rate curves for PUU 80 irradiated by 100 krad dose.....	65
Figure 3.20: Flow rate curves for PUU 90 irradiated by 100 krad dose.....	66
Figure 3.21: Flow rate curves for PUU 100 irradiated by 100 krad dose.....	66
Figure 3.22: Flow rate curves for Reverlink® irradiated by 100 krad dose.	67
Figure 3.23: Reverlink® irradiated by 100 krad dose leakage test.	67
Figure 3.24: PUU 80 and PUU 100 samples immediately after puncture test.	68
Figure 3.25: Flow rate curves comparison for 100 krad irradiation.	69
Figure 3.26: Flow rate curves for PUU 70 irradiated by 500 krad dose.....	70
Figure 3.27: Flow rate curves for PUU 80 irradiated by 500 krad dose.....	70
Figure 3.28: Flow rate curves for PUU 90 irradiated by 500 krad dose.....	71
Figure 3.29: Flow rate curves for PUU 100 irradiated by 500 krad dose.....	71
Figure 3.30: Flow rate curves for Reverlink® irradiated by 500 krad dose.	72
Figure 3.31: Flow rate curves comparison for 500 krad irradiation.	73
Figure 3.32: PUU 70 flow rate comparison between blank aged and irradiated.	75
Figure 3.33: PUU 80 flow rate comparison between blank aged and irradiated.	75
Figure 3.34: PUU 90 flow rate comparison between blank aged and irradiated.	76
Figure 3.35: PUU 100 flow rate comparison between blank aged and irradiated.	76
Figure 3.36: Reverlink® flow rate comparison between blank aged and irradiated...	76
Figure 4.1: Characteristic parameters of the self-healing performance.....	77
Figure 4.2: Strain recovery for viscoelastic materials example [78].	78
Figure 4.3: Scheme of the radius trend during the puncture test.....	80
Figure 4.4: Approximation of the polymer sample as a 2D disk.....	81
Figure 4.5: Scheme of the strain trend during the puncture test.....	81
Figure 4.6: Zener model in Kelvin-Voigt representation [80].	82

Figure 4.7: Fitting for Reverlink® irradiated by 100 krad.	84
Figure 4.8: Fitting for PUU 70 irradiated by 500 krad.....	84
Figure 4.9: Fitting for PUU 100 irradiated by 500 krad.....	85
Figure 4.10: Fitting for PUU 80 Blank (aged).....	85
Figure 4.11:Fitting for PUU 90 Blank (aged).....	85
Figure 4.12: Superposition effects for second and third step of the puncture test.	88
Figure 4.13: Stress curve for second and third step of puncture test.	88
Figure 4.14: $E1$ and $E2$ percentage changes compared to blanks aged.	92
Figure 4.15: Viscosity η percentage changes compared to blanks aged.....	93
Figure 4.16: τ percentage changes compared to blanks aged.	93
Figure 5.1: Ionizing radiation induced effects on polymeric materials [88].	94
Figure 5.2: Polymer radio oxidation [88].	95
Figure 5.3: Q_{max} percentage change of irradiated samples with the respect to blanks.	95
Figure 5.4: Air volume lost percentage change during the tests.	96
Figure 5.5: H bonds between N in urea linkage and H of an amino group (1), between O of a urethane group and H of hydroxyl group (2), between O of urea linkage and H of hydroxyl group (3), between O of a urethane group and H of an amino group (4) [92, 31].	97
Figure 5.6: Q_{max} and V_{leak} percentage change of PUUs due to ageing.....	99
Figure 5.7: Q_{max} and V_{leak} change of Reverlink® due to ageing.	100

List of Tables

Table 1.1: Residence time on the Moon during Apollo Missions [65].	11
Table 2.1: Chemical compounds involved in PUUs synthesis.	36
Table 2.2: Formulation and basic properties of the PUUs considered [14].	36
Table 2.3: Reverlink® HR components' mass [51].	37
Table 2.4: Environmental conditions during the test [50].	41
Table 2.5: Instruments main properties.	44
Table 2.6: Masses pre and post outgassing and humidity concentration in samples.	47
Table 3.1: Glass transition temperatures T_g from DSC tests [50].	49
Table 3.2: T_g comparison between blank and irradiated samples.	51
Table 3.3: Aged and non-aged Reverlink® T_g comparison.	52
Table 3.4: Thermal degradation temperatures from TGA analysis [50].	53
Table 3.5: Blank and irradiated samples thermal degradation temperature [50].	54
Table 3.6: Puncture test results for PUU 70 blank [50].	59
Table 3.7: Puncture test results for PUU 80 blank [50].	59
Table 3.8: Puncture test results for PUU 90 blank [50].	60
Table 3.9: Puncture test results for PUU 100 blank [50].	60
Table 3.10: Puncture test results for Reverlink® [50].	60
Table 3.11: Thicknesses of blank aged samples.	61
Table 3.12: PUUs blank aged puncture test results.	61
Table 3.13: Reverlink® blank aged test results.	62
Table 3.14: Thicknesses of tested irradiated samples.	64
Table 3.15: PUU 70 irradiated by 100 krad dose puncture test results.	64
Table 3.16: PUU 80 irradiated by 100 krad dose puncture test results.	65
Table 3.17: PUU 90 irradiated by 100 krad dose puncture test results.	65

Table 3.18: PUU 100 irradiated by 100 krad dose puncture test results.....	66
Table 3.19: Reverlink® irradiated by 100 krad dose puncture test results.	67
Table 3.20: Comparison of the mean results obtained for 100 krad irradiation.....	68
Table 3.21: PUU 70 irradiated by 500 krad dose puncture test results.....	69
Table 3.22: PUU 80 irradiated by 500 krad dose puncture test results.....	70
Table 3.23: PUU 90 irradiated by 500 krad dose puncture test results.....	71
Table 3.24: PUU 100 irradiated by 500 krad dose puncture test results.....	71
Table 3.25: Reverlink® irradiated by 500 krad dose puncture test results.	72
Table 3.26: Comparison of the mean results obtained for 500 krad irradiation.....	72
Table 3.27: Comparison of the blanks' mean results for each polymer.....	74
Table 3.28: Comparison of the mean results in the different configurations for each polymer.....	74
Table 4.1: Provisional parameters of the viscoelastic model.....	87
Table 4.2: Strain parameters results from the viscoelastic model.	90
Table 4.3: Viscoelastic parameters comparison resulting from the model.	91

List of Symbols

Variable	Description	SI unit
E	young modulus	<i>MPa</i>
h_p	sharp edge height	<i>mm</i>
Q	flow rate	<i>l/min</i>
Q_{max}	maximum flow rate	<i>l/min</i>
Q_{min}	minimum flow rate	<i>l/min</i>
r	hole radius	<i>mm</i>
R_a	gas constant	<i>cal/mol/K</i>
t	time	<i>s</i>
th_p	thickness of the punctured region	<i>mm</i>
T	temperature	$^{\circ}\text{C}$
$T_{5\%}$	TGA onset temperature	$^{\circ}\text{C}$
$T_{95\%}$	TGA endset temperature	$^{\circ}\text{C}$
T_{max}	maximum degradation temperature	$^{\circ}\text{C}$
T_g	glass transition temperature	$^{\circ}\text{C}$
v_p	puncheon probe velocity	<i>mm/s</i>
v_r	radius increase velocity	<i>mm/s</i>
V_{leak}	volume leaked	<i>l</i>
Δt	healing time	<i>s</i>
ε	strain	/
η	viscosity	<i>MPa · s</i>
σ	stress	<i>MPa</i>
τ	relaxation time	<i>s</i>

